GROWTH AND CHARACTERIZATION OF NOVEL GATE DIELECTRICS FOR GALLIUM NITRIDE

By

ANDREA H. ONSTINE

A DISSERTATION PRESENTED TO THE GRADUATE SCHOOL
OF THE UNIVERSITY OF FLORIDA IN PARTIAL FULFILLMENT
OF THE REQUIREMENTS FOR THE DEGREE OF
DOCTOR OF PHILOSOPHY

UNIVERSITY OF FLORIDA

2004

Copyright 2004

by

Andrea H. Onstine

“I don’t think there is any concept that you can’t make understandable to the educated lay public. I always tell my students and postdocs if you can’t explain to your grandmother what you are doing, probably you don’t understand it yourself properly.”

—Nobelist Gunter Blobel

“Between the stirrup and the ground I asked for mercy and mercy there I found.”

—English/Irish Proverb.

ACKNOWLEDGMENTS

This dissertation would not be possible without the help and support of many people in my life. I would first like to thank my advisor, Dr. Cammy Abernathy, for accepting me into the research group, for always having an encouraging word, and for being an inspiration that you can have it all— career, life, marriage, and family. Dr. Abernathy remembered that we were people, and encouraged us to have a life outside of school. I thank my committee members (Dr. Steve Pearton, Dr. David Norton, Dr. Fan Ren, Dr. Rajiv Singh) for their support and knowledge in the field of GaN device processing and semiconductor device physics. I would also like to thank Dr. Amlan Biswas for substituting for Dr. Ren on such short notice.

Many thanks go to Dr. Brent Gila for teaching me everything he knows (or at least as much as I could learn) in the past 4 years. From pumps and MBE, to characterization, to how to deal with people, Brent's help and guidance have been invaluable. People will always enjoy working for and with him.

Thanks go to my parents and family, who supported me completely in anything and everything that I wanted to try. Special thanks go to Aunt Janeen and my father, for all of their help editing and proofreading my dissertation even though they may not have understood everything. I regret that all of my grandparents, especially my paternal grandmother, did not live long enough to see me graduate with my Ph.D.

I would also like to thank my group members and co-workers (Jerry Thaler, Rachel Fraser, Jen Hite, Kimberly Allums, Danielle Stodilka, Mark Hlad, Andrew Hererro,

Jiyhun Kim, Rishab Mehandru, and Wayne Johnson) for all of their help and support. I thank Nina Burbure, Carrie Ross, and Erik Kuryliw for all the time they spent with the Focused Ion Beam system. Thanks go to Kerry Siebein for all of her time spent working in the cold with the High Resolution-Transmission Electron Microscope as well as the conversation.

I thank my long-time friends Aamir Qaiyumi, Amy Matthews, Jennifer Babin nee Adam, Bill Weisner, Bill O'Conner, Pete Meyer, Kathy Daly, Gloria Bergman, Jacques Palmer, Lori Kornberg, and everyone from the Swing Dancing Club, and from Tallwood, for all of their support. It's hard to believe that it has been so long.

TABLE OF CONTENTS

Page

ACKNOWLEDGMENTS iv

LIST OF TABLES ix

LIST OF FIGURES x

ABSTRACT xiv

CHAPTER

1 INTRODUCTION 1

1.1 Motivation 1
1.2 Dissertation Outline 3

2 BACKGROUND AND LITERATURE REVIEW 5

2.1 Introduction to Dielectric Films, Capacitors, and MOS(MIS)FETs 5
2.1.1 Dielectric Films 5
2.1.2 Metal/Oxide/Semiconductor (MOS) Capacitor 7
2.1.3 Metal/Insulator/Semiconductor (MIS) Capacitor 8
2.2 GaN Based Electronic Devices 9
2.2.1 Silicon Oxide on GaN 10
2.2.2 Silicon Nitride on GaN 10
2.2.3 Aluminum Nitride on GaN 11
2.2.4 Gallium Oxide on GaN 12
2.2.5 Silicon Dioxide on Gallium Oxide on Gallium Nitride 13
2.2.6 Gallium Gadolinium Oxide on GaN 13
2.2.7 Gadolinium Oxide on GaN 14
2.2.8 Scandium Oxide on GaN 14

3 EXPERIMENTAL APPROACH 19

3.1 Molecular Beam Epitaxy 19
3.1.1 Substrate Preparation 21
3.1.1.1 Silicon 22
3.1.1.2 Gallium Nitride 22
3.1.2 Magnesium Oxide Growth 23
3.1.3 Magnesium Calcium Oxide Growth 24

3.1.4 Magnesium Scandium Oxide Growth 24
3.2 Materials Characterization 25
3.2.1 Reflection High Energy Electron Diffraction: RHEED 25
3.2.2 Transmission Electron Microscopy: TEM 26
3.2.3 X-Ray Diffraction: XRD 27
3.2.4 Atomic Force Microscopy: AFM 28
3.2.5 Scanning Electron Microscopy: SEM 28
3.2.6 Auger Electron Spectroscopy: AES 29
3.2.7 Ellipsometry 30
3.2.8 Current-Voltage (I-V) measurements 31
3.2.9 Capacitance-Voltage (C-V) measurements 31

4 MAGNESIUM OXIDE: RESULTS AND DISCUSSION 48

4.1 Effect of Oxygen Plasma Source 48
4.2 Effects of Oxygen Pressure 50
4.3 Effect of Substrate Temperature 52
4.4 Scandium Oxide Capping Layer 53

5 MAGNESIUM CALCIUM OXIDE: RESULTS AND DISCUSSION 72

5.1 Growth of CaO 72
5.2 Growth of Ternary MgCaO 73

6 SCANDIUM MAGNESIUM OXIDE AND MAGNESIUM SCANDIUM OXIDE: RESULTS AND DISCUSSION 101

6.1 Scandium Magnesium Oxide 102
6.2 Magnesium Scandium Oxide 103

7 ENVIRONMENTAL AND THERMAL STABILIY 116

7.1 Environmental Stability 116
7.1.1 Magnesium Oxide 116
7.1.2 Magnesium Calcium Oxide 117
7.1.3 Magnesium Scandium Oxide and Scandium Magnesium Oxide 117
7.2 Thermal Stability 117
7.2.1 Magnesium Oxide 118
7.2.2 Magnesium Calcium Oxide 118
7.2.3 Magnesium Scandium Oxide and Scandium Magnesium Oxide 119

8 SUMMARY AND FUTURE WORK 132

8.1 Magnesium Oxide 132
8.2 Magnesium Calcium Oxide 133
8.3 Scandium Magnesium Oxide and Magnesium Scandium Oxide 134
8.4 Environmental and Thermal Stability 134

APPENDIX

A ELLIPSOMETRY 136

A.1 Maxwell's Equations and the EM Plan Wave 138
A.2 Jones Vectors and Matrices 140
A.3 Light Polarization States 141
A.4 Single Films on Thick Substrates 142

B TEM SAMPLE PREPARATION 150

B.1 Old-fashioned Hand Grinding- 150
B.2 Focused Ion Beam Milling 151

LIST OF REFERENCES 159

BIOGRAPHICAL SKETCH 165

LIST OF TABLES

Table		Page
2.1	Properties of dielectric materials that have been used on GaN	16
4-1	Electrical characterization of MgO/GaN diodes.	54
5-1	Growth rate and AES data for MgCaO samples.	78
5-2	Growth rate, AFM and AES data for MgCaO grown at 300˚C.	79
5-3	Composition and mismatch from XRD	80
6-1	Dependence of growth rate, RMS roughness, and AES ratio.	105
7-1	Ellipsometry data. Change in index of refraction	120
7-2	XRR data of as-grown and annealed samples.	121

LIST OF FIGURES

Figure Page

2-1 Capacitor diagrams.....17

2-2 Cross-section illustration of a depletion mode n-MOSFET.....18

3-1 Typical Knudsen effusion oven (After B.P. Gila 2000).....33

3-2 Riber MBE used for oxide growth. 34

3-3 WaveMat 610 ECR plasma head. 35

3.4 Schematic of the Oxford RF plasma source.....36

3-5 AFM images of as received MOCVD GaN and MBE GaN.. 37

3-6 RHEED images showing treated surface of MOCVD grown GaN. 38

3-7 RHEED photos indicating a (1x3) pattern.. 39

3-8 RHEED photos showing different types of diffraction patterns. 40

3-9 TEM column. 41

3-10 The relation between the lattice parameter and Bragg angle.. 42

3-11 Atomic force microscope (after K.K. Harris 2000). 43

3-12 Schematic of SEM column.....44

3-13 SEM operation. 45

3-14 The penetration depth and interaction of an electron beam.. 46

3-15 Ellipsometer schematic (After D.K Schroder[74]) 47

4-1 The MgO structure (from Cullity 1978[75]).....55

4-2 Illustration showing the symmetry between (111) NaCl and (0002) wurtzite plane.56

4-3 RHEED images indicating clean GaN surface and MgO growth. 57

4-4 SEM image of the MgO surface grown at 350°C with ECR plasma source.....58

4-5 AFM images of MgO grown at 350°C and MgO grown at 100°C. 59

4-6 RHEED images of MgO after 1 minute and after 90 minutes of growth at 100°C. 60

4-7 SEM and AFM of MgO grown at 100˚C with RF plasma source.....61

4-8 Mg/O ratio as determined by AES as a function of oxygen pressure. 62

4-9 Dependance of growth rate on oxygen pressure 63

4-10 AFM of MgO grown at 100˚C with oxygen pressure of $1x10^{-5}$ or $1x10^{-4}$ Torr.....64

4-11 SEM and TEM of MgO.....65

4-12 XRD shows that the MgO film grown at 300˚C vs 100˚C.....66

4-13 AFM of MgO grown at 100°C and grown at 300°C. 67

4-14 HRTEM of MgO grown at 300˚C.....68

4-15 SEM of degraded MgO film.....69

4-16 I-V and C-V of MgO/n-GaN diodes, aged15 weeks. 70

4-17 AFM of MgO with and without a capping layer. 71

5-1 Illustration of the CaO structure (from Cullity 1978) 81

5-2 AES shows only Ca and O after growth of CaO at 300˚C 82

5-3 MgO-CaO phase diagram.....83

5-4 HR TEM of CaO. 84

5-5 AFM of CaO grown at 100˚C. 85

5-6 AFM of CaO grown at 300˚C. 86

5-7 AES depth profiling of MgCaO. 87

5-8 XRD of MgCaO shows no signs of phase separation or secondary phases. 88

5-9 Powder XRD showing increase in lattice constant with the addition of Ca.....89

5-10 HR-XRD of the relative positions of MgO (222) and MgCaO (222) peaks. 90

5-11 AFM of MgCaO grown at 100ºC. 91

5-12 AES shows that no Mg or Ca is present after growth time. 92
5-13 AES of MgCaO film grown at substrate temperature of 300˚C. 93
5-14 XRD shows the peak from the MgCaO film grow at 300˚C vs 100˚C. 94
5-15 AFM of MgCaO grown at 100˚C and 300˚C. 95
5-16 AES scans of continuously grown and digitally grown samples. 96
5-17 HR-XRD showing MgCaO and MgO texturing in the (111) direction. 97
5-18 High resolution XTEM of MgO. 98
5-19 HR XRD showing change in peak position with change in shutter timing. 99
5-20 AFM of capped MgCaO at different shutter sequences. 100
6-1 The Bixbyite crystal structure of scandium oxide. (B.P Gila 2000) 106
6-2 AES depth profiles taken from layers grown under different growth conditions. ..107
6-3 AFM surface scans for films grown at different gorwth conditions. 108
6-4 XRD of ScMgO grown at T_{Mg} =350°C and T_{sub} = 300°C.. 109
6-5 Powder XRD showing the peak position of MgScO peak. 110
6-6 AES of MgScO with Sc_2O_3 capping layer. 111
6-7 AFM of MgScO grown at 100˚C, uncapped and with a Sc_2O_3 cap. 112
6-8 AFM of MgScO grown at 300˚C without capping layer. 113
6-9 TEM of MgScO shows epitaxial growth of MgScO on GaN. 114
6-10 EDS of ScMgO. 115
7-1 Accelerated aging experimental set up. 122
7-2 Ellipsometry of the degradation of MgO with and without a capping layer. 123
7-3 Ellipsometry of the degradation of MgCaO with and without capping layer. 124
7-4 Ellipsometry of the degradation of MgScO with and without capping layer. 125
7-5 XRR of MgO uncapped, before and after annealing at 1000˚C for 2 minutes. 126
7-6 XRR of capped MgO before and after annealing at 1000˚C for 2 minutes. 127

7-7 XRR of MgCaO uncapped before and after annealing at 1000˚C at 2 minutes.....128

7-8 XRR of MgCaO capped before and after annealing at 1000˚C for 2 minutes. 129

7-9 XRR of MgScO uncapped, before and after annealing at 1000˚C for 2 minutes...130

7-10 XRR of MgScO capped, before and after annealing at 1000˚C for 2 minutes. 131

A-1 An electromagnetic plane wave. 147

A-2 Geometry of an ellipsometric experiment, showing p- and s-directions.....148

A-3 Multiple reflected and transmitted beams for a single film.. 149

B-1 Strips of sample and support sapphire glued together into a sample stack. 153

B-2 TEM sample polished to 25 μm thick. 154

B-3 The sample glued to a 3mm Cu support ring and orientation of ion milling. 155

B-4 Top view of FIB thinned sample. 156

B-5 Tilted picture of undercut step of FIB sample preparation. 157

B-6 Sample is now cut free and ready for lift-out. 158

Abstract of Dissertation Presented to the Graduate School
of the University of Florida in Partial Fulfillment of the
Requirements for the Degree of Doctor of Philosophy

GROWTH AND CHARACTERIZATION OF NOVEL GATE DIELECTRICS FOR GALLIUM NITRIDE

By

Andrea H. Onstine

December 2004

Chair: Cammy R. Abernathy
Major Department: Material Science and Engineering

Novel crystalline dielectric materials for gate application on gallium nitride were studied. These dielectric materials must operate at high temperatures and under high power loads. To meet these needs, the selected dielectric materials must be thermally stable to temperatures above 1000˚C for device fabrication, must be chemically stable to prevent diffusion into the semiconductor, and must have a low defect density to reduce the charged trap sites in the dielectric and the dielectric/semiconductor interface. The dielectric materials studied were magnesium oxide (MgO), magnesium calcium oxide (MgCaO), and magnesium scandium oxide (MgScO).

These materials were deposited using molecular beam epitaxy (MBE) where the individual elements are supplied independent of each other. This technique allows for the use of a wide range of growth conditions in order to obtain the highest quality material and precise control of the film composition. The dielectrics were deposited on gallium nitride for characterization and device fabrication. The samples were characterized using

a variety of techniques to determine surface roughness, crystal structure, chemical composition, and electrical properties.

MgO deposited using the MBE approach grew epitaxially on GaN for the first 40 monolayers, after which it became polycrystalline. MgO grown at 300˚C using a radio frequency (RF) oxygen plasma source showed the best properties. Optimization of the MgO did not eliminate the problems with MgO as a gate dielectric, namely poor environmental and thermal stability. On annealing, the interface becomes rougher as evidenced by x-ray reflectometry.

Crystalline, single-phase MgCaO was grown by the continuous and digital MBE methods. The digital approach showed better uniformity and morphology. From XRD it was found that the addition of Ca could be used to vary the bond mismatch over a range of -6.5% to +0.96%. As with MgO, environmental stability was still problematic because of reactivity with moisture.

Bixbyite ScMgO exhibited a solid solubility limit of about 9% Mg, after which a magnesium-rich second phase was observed by XRD. This severely limits the usefulness of ScMgO. Rock salt MgScO was grown below this solubility limit and grew epitaxially on GaN. The environmental and thermal stability are not significantly affected by the addition of Sc.

The environmental and thermal stability of the oxides were also investigated. A Sc_2O_3 capping layer was shown to improve both thermal and environmental stability of the oxides. The most stable dielectric was found to be MgCaO with a Sc_2O_3 cap.

CHAPTER 1
INTRODUCTION

1.1 Motivation

The modern microelectronics industry is largely based on solid-state silicon technology. Compound semiconductors are becoming an increasingly important area of research and technology because of the limitations of silicon-based technology. The bandgap of silicon limits the temperature and power operation range of the devices. Also, since silicon is an indirect bandgap material, it will never be an efficient light emitter. Compound semiconductors are based on elements from Groups III and Groups V of the periodic table, such as gallium arsenide (GaAs) and indium phosphide (InP). These compound semiconductor devices have higher carrier mobilities, resulting in faster devices and lower-saturation electric fields than silicon semiconductor devices. Also, some compounds have direct band gaps that lead to efficient light emission and light detection.

Transistor research based on compound semiconductors has led to several breakthroughs in device performance. Recently, research in this field has produced a GaAs metal/oxide/semiconductor (MOS) capacitor that demonstrated properties useful for transistors.[1] This discovery led to an operational GaAs-based MOS transistor incorporating gallium gadolinium oxide as a gate dielectric.[2] Further research has shown that the gadolinium content of the oxide was responsible for surface passivation, and improved the electrical properties of the device.[3-7] There are still limits to these exciting compound materials, such as the thermal operating limit and power-handling capabilities.

These obstacles can be overcome by using a semiconductor material with a wider bandgap. The term "wide bandgap" refers to the forbidden energy gap of a material, a region in the energy diagram that is not occupied by electrons, that is typically greater than 2 eV, (Figure 1.1). Wide bandgap semiconductors have been researched for decades, beginning with silicon carbide (SiC) in the middle of the 20th century. In more recent years, research has turned to Group III-nitrides (such as gallium nitride), and Group II-VI materials. Because of the ease of defect propagation through the II-VI device structure during operation at room temperature, these materials have been set aside for materials that show more potential. The III-V nitride and SiC semiconductors are more thermally stable at device operating temperatures, and therefore do not have the defect-propagation problems associated with II-VI semiconductors. Table 1.1 lists some wide bandgap semiconductors and their properties, as well as those of silicon and gallium arsenide.

Nitride-based semiconductors have become a focus for research into optoelectronic devices. By creating ternary alloys, the III-nitride light emitting devices (LEDs) have covered the entire visible spectrum. Other photonic devices include UV detectors and laser diodes. Many of the lessons learned (and processes developed) by photonics research have led to the growth of high-quality material, improved electrical contacts, and controllable materials processing. From this base, research has been initiated to create microwave, ultrahigh-power switches and devices that operate at high temperatures.[8] Advances in SiC and GaN have led to power switches based on different configurations like metal-semiconductor field effect transistors (MESFETs), heterojunctions field effect transistors (HJFETs), and heterojunction bipolar transistors (HBTs). While these devices

have shown promise for a number of applications, the metal oxide (or insulator) semiconductor field effect transistor (MOSFET or MISFET) is also a desirable structure. Complementary devices are required for logic circuits. The MOSFET or MISFET structure can be made into complementary metal oxide semiconductor, CMOS, logic. The MESFET, HJFET, and HBT structures cannot be made into complementary devices. A complementary circuit based on wide bandgap semiconductors will allow for an entire monolithic control circuit to be constructed for high-temperature/high-power use.

For a MOS(MIS)FET to be realized, a high-quality dielectric material must be created for the gate insulator. This material must have a bandgap wider than the semiconductor, a dielectric constant larger than the semiconductor, and high temperature stability similar to the semiconductor. The materials that have been previously researched for this roll are discussed in Section 2.2. Because of deficiencies in various areas, each of these materials is not optimum for devices on GaN. Finding new materials to satisfy these requirements is the goal of our study. Materials selected for this study were MgO, MgCaO, ScMgO, and MgScO.

1.2 Dissertation Outline

The objective of our study was to explore the feasibility of growing lattice-matched oxides for GaN devices by molecular beam epitaxy and characterization of these materials. The background and literature review is given in Chapter 2. In the background, definitions of dielectric materials, capacitance, and MOSFET are given. The literature review contains descriptions and results of dielectric materials used on GaN. In Chapter 3, the growth methods of the oxides are explained along with the characterization methods. Chapters 4, 5 and 6 describe the results of the dielectric materials grown and discuss how the different dielectric materials compare to each other.

Chapter 7 covers the environmental and thermal stability of the dielectrics. Finally, conclusions and future experiments are given in Chapter 8.

CHAPTER 2
BACKGROUND AND LITERATURE REVIEW

2.1 Introduction to Dielectric Films, Capacitors, and MOS(MIS)FETs

The following sections discuss the basics of dielectric films, their properties, and applications. The capacitor is an important tool for testing these dielectric materials. The metal/insulator/semiconductor transistor is a solid-state switch that is controlled by the capacitor structure in the gate region.

2.1.1 Dielectric Films

Insulators are characterized by the absence of charge transport. Insulators have positive and negative charges in the form of atom nucleus and electron cloud; but these charges are bound to the atom or molecule, and are not available for conduction. When materials are placed in an electric field, there is a shift,(or polarization) in the charge distribution, and it is this polarization that leads to dielectric behavior in the material.[9] The polarization induces dipoles within the atomic or molecular structures that are aligned with the applied field. The ability of a material to resist the polarization of charge is described as the dielectric constant, K, which is the ratio of the permittivity of the material, ε_i, to the permittivity of vacuum,ε_v.

$$K = \varepsilon_i / \varepsilon_v \tag{2-1}$$

The dielectric constant can also be related to the internal field created within the material and the external applied field, through the equation 2-2.[10]

$$E_{internal} = E_{applied} / K \tag{2-2}$$

The polarization, P, of the material is related to the dielectric constant by the Equation 2-3, where ξ is the strength of the electric field (V/m). It can be assumed from this relation that the polarization increases as the electric field strength increases, until all the dipoles are aligned such that

$$P=(K-1) \varepsilon_o \xi \quad (2-3)$$

There are several applications for dielectric materials. Passivation of high-voltage junctions, isolation of devices and interconnects, and gate insulation of field-effect transistors are a few applications that are relevant to this discussion. For a material to be a successful dielectric, it must meet certain criteria. Desirable characteristics include chemical stability over the lifetime of the device, immobile charge traps (to avoid shorting and frequency limits), and a dielectric constant higher that that of the semiconductor (to avoid generating a high electric field in the dielectric). In the case of the wide-bandgap semiconductor devices, the dielectric materials must also have excellent thermal stability, since the high-power applications will result in elevated operating temperatures. Another criterion important to wide bandgap semiconductors is that the band gap of the dielectric must be greater than that of the semiconductor. The ideal dielectric would keep the electrons and holes in the semiconductor, and out of the dielectric. To achieve these properties, the bandgap of the dielectric must be larger than the semiconductor, and the electron affinity nearer to the vacuum level, according to the electron affinity rule, Equation 2-4.

$$\Delta Ec +\Delta Ev = \Delta Eg \quad (2-4)$$

The dielectric/semiconductor interface is also an important focus of research in the area of device processing. The interface state density of carrier traps must be

$<10^{11}$ $eV^{-1}cm^{-2}$ for a device to be considered successful. Another important focus is the fixed dielectric charge density, or carrier trap density within the dielectric. To date, several dielectric materials have been researched for use in wide-bandgap semiconductor switches, including AlN, Al_2O_3, Ga_2O_3, Gd_2O_3, $Ga_2O_3(Gd_2O_3)$, SiO_x and Si_3N_4, Table 2.1.

2.1.2 Metal/Oxide/Semiconductor (MOS) Capacitor

Since the gate is the actual on/off switch in the transistor structure, defining the properties of the gate and its operation are extremely important. The gate structure is identical to the metal/oxide/semiconductor capacitor, (Figure 2-1). A capacitor is a device made of two parallel, conducting plates separated by an insulating material. When a direct current (DC) voltage is applied to one side of a capacitor, an equal and opposite charge forms on the other side of the capacitor. In most cases, the DC voltage is applied to the metal side of the capacitor, and the charge is formed in the semiconductor. The amount of capacitance that the capacitor can hold is directly related to the dielectric constant of the dielectric material,[11] (Equation 2-5) where C is the capacitance, ε_0 is the permittivity of vacuum (ε_0=8.854x10^{-14} F/cm), ε_i is the permittivity of the material, A is the area of the metal contact, and d is the thickness of the dielectric material.

$$C= \varepsilon_0 \varepsilon_i A/d \tag{2.5}$$

The capacitance is independent of the applied voltage to the gate, but is completely dependant on the geometry and the dielectric constant. This gives a theoretical capacitance for a given device geometry. If the applied electric field becomes too great, the charges are ripped from the material and conducted to the charged plates. This leads to a short in the material, and is termed dielectric breakdown.

However, as usually happens in practice, the theoretical value and the measured value rarely match. The measured capacitance value is actually the sum of two capacitors in series. These are the dielectric capacitance and the semiconductor space-charge layer capacitance. The semiconductor capacitance, C_s, is responsible for deviation in the measured capacitance, and is voltage-dependant.[12] As the bias is applied to the metal, the majority carriers in the semiconductor are repelled from the oxide/semiconductor interface, resulting in a space-charge layer. This is assuming that the applied bias is the same charge as the majority carriers in the semiconductor. The space-charge layer is populated by minority carriers, and given the name majority-carrier depletion layer.[11]

The frequency of the field applied to the capacitor can also affect the trap layer in the semiconductor. Traps within the semiconductor material become filled with carriers that are attracted to the dielectric/semiconductor interface. When the bias is released, the traps are emptied. If the frequency becomes too high, the traps do not have sufficient time to empty and form a charge layer. At low frequencies, this layer is almost nonexistent. As the frequency is increased, however, this trap layer becomes thicker and adds to the total capacitance. Capacitance measurements must be made at extremely low frequencies, called quasi-static frequencies, to obtain the capacitance that is purely within the dielectric material.

2.1.3 Metal/Insulator/Semiconductor (MIS) Capacitor

Modern silicon technology is based on complementary pairs of metal oxide semiconductor (CMOS) transistors. This is one of the most common devices found in logic and memory circuits. The gate region of the transistor determines the capabilities of the device. The two types of metal oxide semiconductor field effect transistor

(MOSFET) devices are depletion mode and enhancement mode. In the depletion-mode device, the material type under the source, gate and drain regions is the same. This device is in the "on" state when no gate voltage is applied. In the enhancement-mode device, the material type under the gate is opposite that under the source and drain. This device is in the "off" state when no applied gate voltage is applied. Figure 2-2 shows a cross-section of a depletion-mode MOSFET. Because of the relatively low p-type carrier concentration available for p-GaN, only n-type depletion-mode devices were considered.

The n-type MOSFET was used to describe the operation of the gate in the transistor. For a p-type MOSFET, the gate voltage is reversed. When there is a zero gate voltage, carriers are free to flow from the source to the drain in the MOSFET structure. The switch is "on". As a negative voltage is applied to the gate contact, electrons under the gate dielectric are repelled (like charges repel) and a positive charge is induced in the semiconductor under the gate region. This positive charge hinders the ability for electrons to flow from the source region to the drain region. As the gate voltage is increased, more positive charges collect under the gate until the flow from source to drain is completely stopped. The voltage is called the pinch-off voltage, since it effectively pinches the channel shut. The transistor is now "off". As the current through the source-drain is increased, it requires more gate voltage to successfully pinch-off the carrier flow. Thus the maximum operating parameters of the device are determined by the amount of electric field that can be applied to the gate before the dielectric breakdown occurs.

2.2 GaN Based Electronic Devices

Gallium nitride research has resulted in long-lifetime, room temperature operation of photonic devices. These include LEDs that cover the visible spectrum, laser diodes in the blue and blue-green regime, and UV detectors. These devices are just recently

reaching production levels with problems still to be solved in the fields of n-Ohmic and p-Ohmic contacts, p-type doping issues, Schottky contacts, and dielectric materials. Also, with the lack of availability of high-quality GaN substrates, research of epitaxial growth and substrate selection is still ongoing. From material and processing advances learned from the photonics research, high-power and high-temperature switches have been realized. The following summarizes some of the dielectrics research to date.

2.2.1 Silicon Oxide on GaN

Silicon oxide is a very attractive choice for a dielectric material since is has been well studied and the processing is well established. Silicon oxide deposited by plasma enhanced chemical vapor deposition (PECVD)[13-16] has been reported to give interface state densities on the order of low 10^{11} $eV^{-1}cm^{-2}$. Silicon oxide deposited by electron beam (EB) evaporation has shown interface state density of $5.3x10^{11}$ $eV^{-1}cm^{-2}$.[15] After annealing the EB deposited SiO_x at 650C°, the valance band offset was measured to be 2eV and the conduction band offset was measured to be 3.6 eV.[17] The EB evaporated SiO_x shows a silicon rich stoichiometry when compared to the PECVD SiO_x.

There are several inherent problems with SiO_x as a dielectric material for wide bandgap semiconductors. The high D_{it} of SiO_x is due to uncontrolled oxidation of the surface[18]. The most significant limitation is that SiO_x has a dielectric constant (ε) of 3.9, which is significantly lower than that of GaN ($\varepsilon = 8.9$). This will create a very large electric field in the dielectric, leading to further breakdown.

2.2.2 Silicon Nitride on GaN

Silicon nitride deposition by PECVD[15,16] reported an interface state density of $6.5x10^{11}$ $eV^{-1}cm^{-2}$. This value is reasonable for a first attempt. But when compared to

GaN MESFETs, the Si_3N_4 MISFET was out performed. Electrical measurements showed the MISFET structure had a large flat band voltage shift (3.07 V) and a low breakdown voltage (1.5 MV/cm). There was no microstructural analysis performed on the deposited Si_3N_4 films. SiN deposited by ECR plasma CVD showed a D_{it} of $1x10^{11}cm^{-2}eV^{-1}$ but has excess leakage current due to small conduction band offset.[18] The ECR-CVD MIS diode showed a D_{it} of $4x10^{11}$ $cm^{-2}eV^{-1}$, fixed oxide charge of $1.1x10^{11}$ cm^{-2} and breakdown 5.7 MV/cm with a dielectric constant of 6.[19]

A unique dielectric structure of $SiO_2/Si_3N_4/SiO_2$ (ONO) was reported to have breakdown field strength of 12.5 MV/cm for temperatures as high as 300°C.[20] The ONO structure was deposited by jet vapor deposition to a thickness of 10 nm /20 nm /10 nm. The multiplayer structure does allow for unique engineering of a dielectric, but multiple interfaces can lead to an extremely large number of interface state traps and increased processing. The D_{it} for the ONO structure was shown to be less than $5x10^{10}$ $eV^{-1}cm^{-2}$ with breakdown fields greater than 12 MV/cm.[21]

2.2.3 Aluminum Nitride on GaN

Aluminum nitride deposited by MBE and MOCVD has been used to create MISFET devices and insulated gate heterostructure field effect transistors (IG-HFET) devices.[22,23] The AlN MISFET structure grown at 400°C was polycrystalline. From x-ray reflectivity measurements, the AlN/GaN interface showed a roughness of 2.0 nm. This may be due to the polycrystalline nature of the film or from intermixing of the AlN and GaN at the interface. The dielectric breakdown field was calculated to be 1.2 MV/cm. The AlN IG-HFET structure was grown at 990°C, forming a single crystal film of 4.0 nm. This device operated in enhancement mode and had a pinch-off voltage

of 0 V. Hexagonal aluminum nitride has a 2.4% lattice mismatch with hexagonal GaN on the (0001) plane. The 4.0 nm film thickness is greater than the critical thickness allowed for elastic deformation leading to threading dislocations forming from plastic deformation. Single crystal AlN and polycrystalline AlN films suffer from defects and grain boundaries that cause shorting.

2.2.4 Gallium Oxide on GaN

Gallium nitride forms a stable native oxide. This oxide has been considered as a dielectric material, like the native oxide of silicon. Thermal oxidation of the GaN surface has lead to some interesting research. Oxidation was performed in dry[24,25] and wet[26] atmospheres. Dry oxidation of GaN epilayers at temperatures below 900°C showed minimal oxidation. Dry oxidation at 880˚C for 5 hours showed 1110 nm of β-Ga_2O_3 with a D_{it} of $1x10^{10}$ $eV^{-1}cm^{-2}$ and showed inversion.[27] At temperatures above 900°C, a polycrystalline monoclinic Ga_2O_3 forms at a rate of 5.0 nm/hr. This oxidation rate is too slow to be viable as a processing step. Wet oxidation of GaN also forms polycrystalline monoclinic Ga_2O_3, but at a rate of 50.0 nm/hr at 900°C. From cross-sectional transmission electron microscopy, the interface between the oxide and the GaN is found to be non-uniform. Scanning electron microscopy shows that both films are rough and faceted. Electrical characterization of the oxide shows the dry oxide dielectric field strength of 0.2 MV/cm and the wet oxide dielectric field strength of 0.05 to 0.1 MV/cm. Some limits to the thermal oxidation of GaN are that only one microstructure has been formed from this process and GaN is consumed in the process. XRD shows this to be a high temperature hexagonal phase[28]. Ga_2O_3 passivates the surface,[28-31] and has a D_{it} of 10^{11} $eV^{-1}cm^{-2}$ for GaN MOS. A negative oxide charge as well as high capacitance and

reduced reverse leakage where shown for thicker oxides grown by PEC.[29] Using PEC and HeCd laser, a low reverse leakage current of 200 pA at 20 Vm has been achieved. For this oxide the forward breakdown, $E_{fb,}$ is 2.8 MV/cm and the reverse breakdown, E_{rb}, is 5.7 MV/cm with a D_{it} of 2.53 x 10^{11} $cm^{-2}eV^{-1}$. The dielectric constant of Ga_2O_3 grown under these conditions is estimated at 10.6.[33] With amorphous GaO deposited by PEC, low leakage currents of <10 x 10^{-8} Å/cm at –15 V have been measured. Using Ga_2O_3 as both gate dielectric and passivation layer, a breakdown field of 0.4 MV/cm was observed. The bandgap, E_g, of Ga_2O_3 was measured to be 4.4 eV.[34]

2.2.5 Silicon Dioxide on Gallium Oxide on Gallium Nitride

Depending on the growth technique, the interface between the SiO and the GaN can vary drastically. When SiO is deposited by RPECVD, a parasitic subcutaneous layer of native gallium oxide is grown on the GaN surface. This layer as been shown to have a direct effect on the device performance. When the thickness of the initial GaO layer is controlled by a pre-oxidation step the device characteristics improve markedly. Remote Plasma Assisted Oxidation first followed by RPECVD gave a lower D_{it} and a smaller flat band shift over the RPECVD of the SiO_x alone.[35] Real and ideal CV curves are nearly identical.[36] After an anneal in an RTA for 1 min at 900˚C in Ar the D_{it} is 2-3x10^{11} cm^{-2}.[37,38] Another group used a similar oxide growth technique and measured a D_{it} of 3.9x10^{10} $eV^{-1}cm^{-2}$ and a low leakage current.[39,40]

2.2.6 Gallium Gadolinium Oxide on GaN

Due to the recent success of gallium gadolinium oxide (GGG) as a dielectric in GaAs MOSFETs[41-46], attention has turned toward this as a dielectric material for GaN. The GGG dielectric was deposited on a GaN epilayer by EB evaporation of a single crystal GGG source.[22] The substrate temperature was 550°C. The interface roughness

was calculated to be 0.3 nm from x-ray reflectivity. Metal oxide semiconductor (MOS) capacitors were formed and tested. A breakdown field of greater than 12 MV/cm was estimated. More recently, the thermal stability of the film and the interface has been proven to temperatures as high as 950°C and operation of a depletion mode MOSFET has been performed at temperatures up to 400°C.[47] The EB evaporated GGG stoichiometry is heavily dependant upon the substrate temperature. Changes in temperature lead to changes in the stoichiometry.[48] This limits the available microstructure obtainable within the stoichiometric limits of GGG.

2.2.7 Gadolinium Oxide on GaN

GaN based MOSFETs have been made that used a stacked gate oxide consisting of single crystal gadolinium oxide and amorphous SiO_2.[49] The gadolinium oxide provides a good oxide /semiconductor interface and the SiO_2 reduces the gate leakage current and enhances oxide breakdown voltages. The dislocations in the Gd_2O_3 film limit the breakdown field that can be sustained in the dielectric.

2.2.8 Scandium Oxide on GaN

Scandium oxide grown by MBE has been used as a gate dielectric and passivation layer for GaN based devices. Scandium oxide has the bixbyite crystal structure, a reasonable band gap of 6.3 eV and a lattice mismatch to GaN of 9.2%. The scandium oxide was grown by MBE using an RF oxygen plasma, substrate temperature of 650°C and an effusion cell temperature of 1130°C. The surface state density is $8.2 \times 10^{12} eV^{-1} cm^{-2}$ and showed inversion for gated diodes.[50] This oxide was also grown under the same conditions except the substrate temperature was lower to 100°C, which resulted in an interface state density of 5×10^{11} $eV^{-1} cm^{-2}$.[51]

Scandium oxide has also been used as a field passivation layer for GaN devices. It has been shown to reduce the reverse leakage current an increase the f_T and f_{MAX}. The passivation films have been grown with a substrate temperature of 100°C and a cell temperature of 1130°C.[52] Scandium oxide has better long-term stability than SiN_x as a passivation film for GaN based HEMTs. It has been shown to dramatically reduce the gate lag problems due to surface states on AlGaN/GaN HEMTs.[53]

Table 2.1. Properties of dielectric materials that have been used on GaN

Material	Bandgap (eV)	Dielectric (ε)	Melting Point (K)	References
AlN	6.2	8.5	3273	54,55,56
Al_2O_3	5.75	12	2319	57,58,59
Ga_2O_3	4.4	10	2013	60,61,62
Gd_2O_3	8.5	11.4	2668	63,64,65
$Ga_2O_3(Gd_2O_3)$	4.7	14.2	2023	2,66
SiO_x	8-9	3.9	1993	12,59,67
Si_3N_4	5.0	7.5	2173	12,67,68
MgO	7.3	9.8	3073	59,69,70,71
Sc_2O_3	6.3	11.4	2678	72

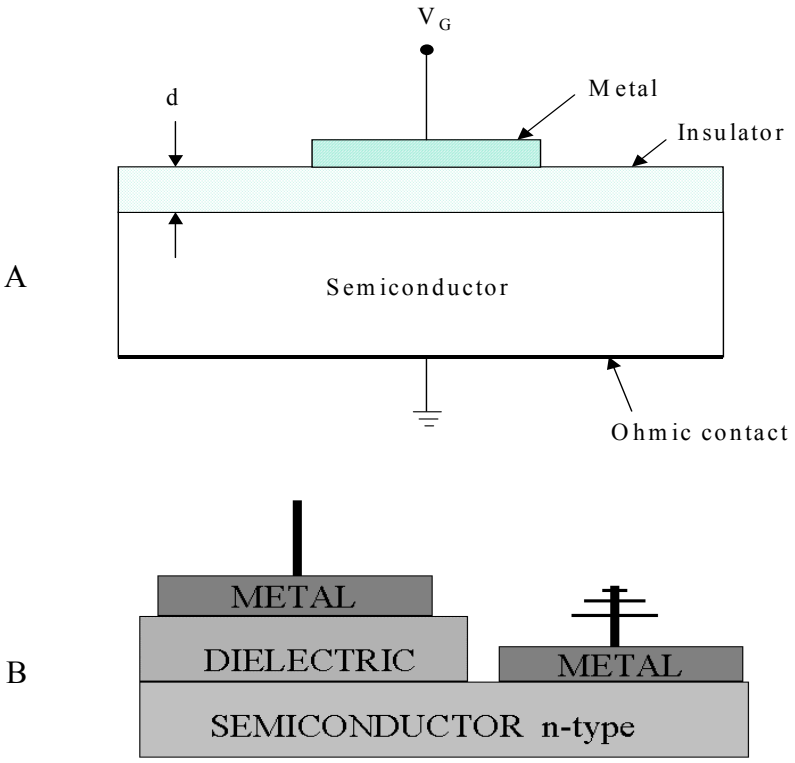

Figure 2-1. Capacitor diagrams. A) Typical metal-insulator-semiconductor capacitor with backside ohmic contact. B) Typical planar capacitor produced in our study.

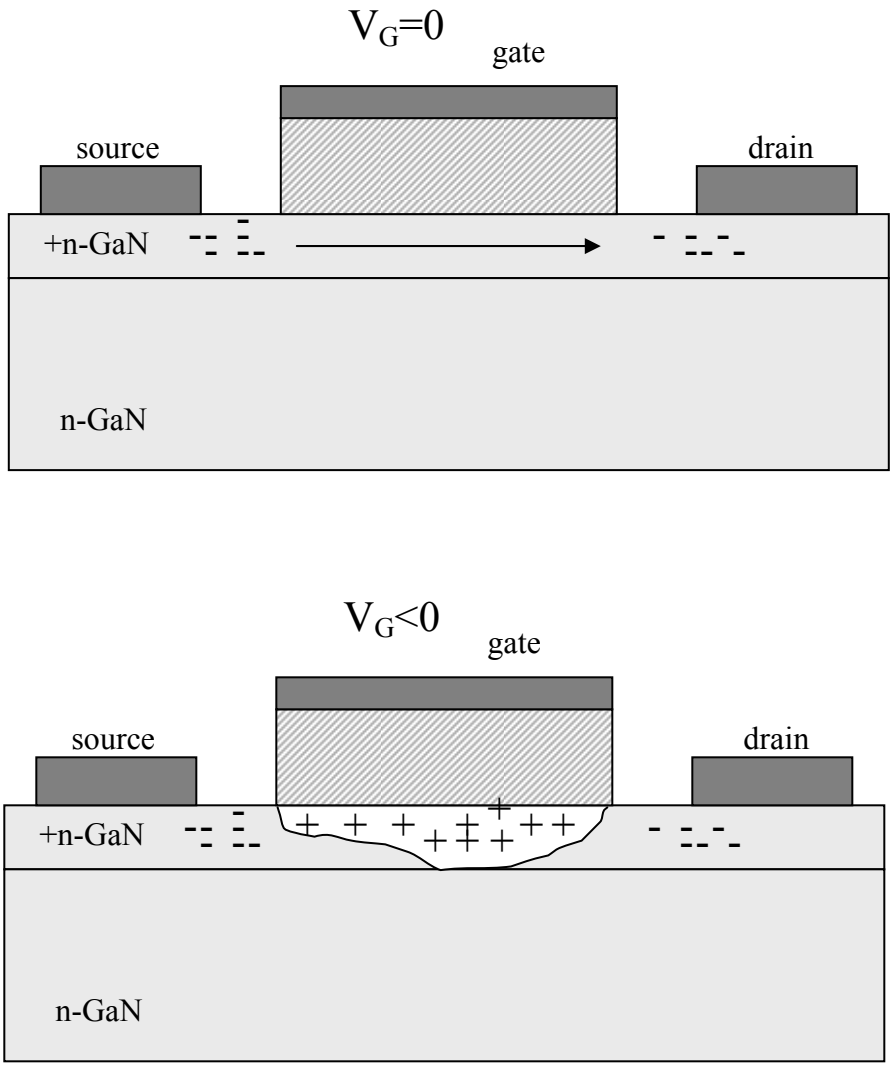

Figure 2-2. Cross-section illustration of a depletion mode n-MOSFET. In the top figure, the device is in the "ON" state with V_G=0. The bottom figure is the device in the "OFF" state with V_G<0, notice the conduction channel is pinched-off.

CHAPTER 3
EXPERIMENTAL APPROACH

3.1 Molecular Beam Epitaxy

Molecular beam epitaxy (MBE) was the growth method employed in this work to produce the dielectric films. The dielectric materials were deposited in an ultra-high vacuum environment from the purest attainable elements. In MBE, the individual elements of the compound are provided to the growth surface independent of each other, allowing for a high degree of control over the stoichiometry of the dielectric material that conventional sputtering and electron beam evaporation do not allow. Also, MBE allows for precise control of the substrate temperature, which in turn helps to control the microstructure of these materials. The growth rate is dependent upon the substrate temperature, the ratio of the elements, and also the rate at which the elements are supplied to the substrate.

In conventional MBE, beams of atomic or diatomic species are produced from ovens called Knudsen cells (Figure 3-1). The purity of the atomic beam depends upon the vacuum level in the chamber and the purity of the source material. The number of atoms emitted from the Knudsen cell is related to the temperature of the cell and the relative atomic mass of the material in the cell. This relation is modeled by the Equation 3-1 where F is the flux of the Knudsen cell in atoms/cm^2-s, p is the vapor pressure in the cell in Torr, a is the orifice area in cm^2, d is the cell to substrate distance in cm, M is the atomic mass of the element in amu, and T is the temperature of the cell in degrees Kelvin.

$$F = \frac{1.18x10^{22}(p)(a)}{d^2(MT)^{1/2}}\left(\frac{atoms}{cm^2 s}\right) \quad (3\text{-}1)$$

For these oxides, a Riber model 2300 MBE was modified to perform the growth. A sketch of this system is shown in Figure 3.2. The main growth chamber was pumped on with a cryopump allowing for a base pressure of $2x10^{-9}$ Torr. This modified system is equipped with a Reflection High-Energy Electron Diffraction (RHEED) system, described in Section 3.2.1. This allows for the arrangement of the top few monolayers of atom to be determined. This is extremely important in determining the atomic arrangement of the starting growth surface and in determining the structure of the film.

The oxygen source for the oxide growth was a WaveMat model 610 electron cyclotron resonance (ECR) plasma source, (Figure 3-3) operating at a frequency of 2.54 GHz and powers ranging from 100 to 200 watts or an Oxford Applied Research radio frequency (RF) oxygen plasma source, Figure 3-4, operating at 13.56 MHz with the RF power set at 300W. Oxygen is supplied to the plasma generator through a leak valve using a 99.995% oxygen source. The ECR plasma sources works by microwave energy that is guided into the source chamber and coupled into the oxygen molecule electron cloud. A series of permanent magnets around the source chamber create a magnetic field, which accelerates the electron motion into helical paths that collide and ionize the source gas molecules. This creates a dense plasma in the source chamber. The plasma contains the atomic species for growth, as well as ionic and molecular species. The RF plasma source operates by means of an electrical discharge created from inductively-coupled RF excitation.[73] Atoms produced by dissociation in the discharge tube can escape into the vacuum environment along with the undissociated molecules via an array of fine holes in the aperture plate. The electrical potentials are such that negligible currents of ions or

electrons escape form the discharge during normal operation of the source. Dissociated atoms undergoing wall collisions in the discharge chamber exhibit a low recombination coefficient and may also ultimately contribute to the radical beam flux. The pressure in the discharge chamber is sufficiently low that atom-gas collisions are minimal over the dimensions of the discharge chamber.[73]

The substrate temperature was determined by a backside thermocouple in close proximity with the substrate holder. The substrate thermocouple was calibrated by using the melting points of gallium antimonide (GaSb) at 707˚C and indium antimonide (InSb) at 525°C. Pieces of GaSb and InSb were heated in the growth position with a nitrogen plasma impinging on the surface. This reduces the chance for loss of the Group V, Sb, species during the heating process, which would result in an incorrect melting temperature. With out the nitrogen over pressure, the InSb and GaSb would degrade by loss of Sb, the more volatile Group V species, before melting.

3.1.1 Substrate Preparation

Prior to any epitaxial growth, the substrates receive an *ex-situ* and *in-situ* surface treatment to remove any contamination and the native oxide. The surface of the semiconductor must be as clean and planar as possible to ensure high quality dielectric film deposition. Surface contamination leads to impurities at the dielectric/semiconductor interface, which ultimately results in creating interface traps, as described in Section 2.1.2. The substrates were visually inspected as well as scanned using atomic force microscopy (AFM), described in Section 3.2.4. This gave a reference for the surface roughness to compare to the final product. The substrates used in this work are silicon (Si) and gallium nitride (GaN).

3.1.1.1 Silicon

All of the initial experiments were carried out on Si single crystal substrates oriented in the <001> direction. This was due to the wide availability of Si substrates and their low cost. The data gathered from the Si substrates is used to calibrate the growth rate and composition of the dielectric films. The microstructure of the dielectric films grown on Si will be different from that on GaN since the surface atomic spacing and the crystal structure of the substrates are different.

Silicon wafers received as *ex-situ* treatment of a 30 second wet etch in a buffered oxide solution consisting of 6 parts ammonium fluoride and 1 part hydrofluoric acid, rinsed in deionized water (DI), and dried under nitrogen gas. This treatment results in a smooth surface with a surface roughness root mean square (RMS) value of 0.08 nm, as seen in AFM. This surface is oxide free and stable for a period of up to one hour. The *in-situ* cleaning consists of heating the silicon up to 200˚C in order to drive off any moisture from exposure to the atmosphere.

3.1.1.2 Gallium Nitride

Since gallium nitride wafers substrates are not currently available, gallium nitride grown on sapphire wafers oriented <0001> were used. These will be referred to throughout this work as GaN substrates. Two different types of growth of the GaN substrates were employed in this work, MBE and metal-organic chemical vapor deposition (MOCVD). The MBE GaN substrates were provided by SVT Associates and the MOCVD substrates were provided by Epitronics, QinetiQ, and Uniroyal Optoelectronics (UOE). From AFM, there is a large difference in surface roughness between the two types of GaN. The MOCVD substrates are 1-3 nm RMS roughness and the MBE substrates are ~6 nm RMS roughness (Figure 3-5).

The GaN substrates received an *ex-situ* treatment consisting of a 3-minute etch in (1:1) hydrochloric acid: water, followed by a DI rinse and blown dry by nitrogen. This was use to remove any organic residue from the surface. Then a 25-minute exposure to ozone produced by an ultraviolet lamp in a UVOCS UVO Cleaner model number 42-220 was used to oxidize the carbon on the surface and create a thin native oxide layer. Next, the substrates received another etch in buffered oxide etch for 5 minutes, in the solution described for silicon, to remove the native oxide. This is shown by observing the reflection high-energy electron diffraction (RHEED) pattern produced from the surface, described in Section 3.2.1. The RHEED pattern produced by the native oxide is more diffuse than the pattern produced by the buffered oxide etched surface (Figure 3-6).

The GaN substrates were then mounted to molybdenum blocks using indium solder, and then loaded into the load-lock of the MBE. Room temperature RHEED measurements showed a reasonably clean (1x1) surface (Figure 3-6). Two different crystal directions are observed in RHEED to create a more complete understanding of the surface. Here, the <1-100> and the <11-20> directions are observed. An *in-situ* thermal treatment was employed to further remove any oxide or contamination left on the surface. The substrates were heated to 700˚C in vacuum and no overpressure of nitrogen was used. The RHEED patterns recorded at this temperature indicate a sharp (1x3) pattern (Figure 3-7).

3.1.2 Magnesium Oxide Growth

The magnesium oxide samples were grown from 99.99% pure magnesium and Knudsen cell temperatures ranging from 350°C to 400°C. Substrate temperatures between 100°C and 340°C were used. The oxygen was provided by an Oxford RF

plasma source at 300 W forward power or an ECR Wavemat plasma source set to 200 W forward power. There was a significant difference in the properties of the films between the 2 plasma sources. The RF plasma source produced the superior films. Oxygen pressure was varied from $8x10^{-6}$ up to $1x10^{-5}$ Torr. In all cases, the sample rotation was kept at 15 rpm.

3.1.3 Magnesium Calcium Oxide Growth

The magnesium calcium oxide samples were grown from the same Mg sources as that used for the MgO with the addition of 99.999% pure calcium, Ca, from another Knudsen cell with temperatures ranging from 450°C to 500°C. Substrate growth temperatures were between 100°C and 300°C. The two growth methods that were used are continuous where all shutters open at once and exposed to the substrate and digital alloying where alternating layers of MgO and CaO. Changing the flux of the metal sources during a continuous growth or changing the timing of the shutter sequences during digital growth varied the composition of the film. Oxygen pressure was held at $8x10^{-6}$ Torr and used only the RF plasma source. As in the MgO growth, the sample rotation was kept at 15 rpm.

3.1.4 Magnesium Scandium Oxide Growth

The magnesium scandium oxide films were grown using the same Mg source with the addition of a Sc metal Knudsen cell with temperatures ranging from 1090°C to 1190°C due to the extremely low vapor pressure of scandium. Substrate temperatures were between 100°C and 300°C. Growth methods for this ternary oxide were continuous and digital as in the MgCaO films. It was not possible to take a flux reading of the scandium due to severe fluctuations in readings, the needle bounced around, when the

cell at temperature due to out-gassing of He from the Sc source metal. The out-gassing of He was shown by the mass spectrometer. The composition of the film was varied by changing the temperature of the source metals. As a convention, films with a higher amount of scandium then magnesium are referred to as scandium magnesium oxides, ScMgO. Films with a greater amount of magnesium than scandium are referred to as magnesium scandium oxides, MgScO. Oxygen pressure was held at $8x10^{-6}$ Torr and used only the RF plasma source. As in the MgO growth, the sample rotation was kept at 15 rpm.

3.2 Materials Characterization

The films were heavily characterized after growth. Emphasis of the research was placed on, but not limited to, the microstructure and the stoichiometry of the epitaxial films and how these properties related to the electrical properties, environmental and thermal stability of the dielectric materials. The dielectric films were annealed to temperatures as high as 1000°C by a rapid thermal anneal (RTA) process to determine the thermal stability of the films.

3.2.1 Reflection High Energy Electron Diffraction: RHEED

In-situ structural characterization can be done in the growth chamber via reflection high-energy electron diffraction (RHEED). A RHEED system consists of an electron gun, typically 5 to 30 kV, and a phosphorescent screen. The electrons from a filament are collimated, accelerated, and reflected off the surface of the sample. A diffraction pattern is seen on the phosphorous screen. From this diffraction pattern, single crystal, polycrystalline and amorphous films can be differentiated. This technique was used to determine the starting substrate surface quality and the quality of the films grown while

in the ultra-high vacuum system. Also, the method of growth initiation, which has an enormous impact on the overall film quality, can be determined from RHEED.

RHEED reflections are created by diffraction from the surface of the substrate. The incoming electron beam has a grazing incident angle of 1 to 2 degrees. Diffraction occurs only along certain crystal directions in a single crystal material. From the type of pattern, intensity, and spacing between different diffraction events, a 2-dimensional map of the surface can be created. It is this map that will help determine the condition of the starting substrate as well as of the grown film. A surface growing layer-by-layer (2D) will produce a pattern with streaky lines, whereas a surface growing by islanding (3D) will produce a pattern that is spotty. Polycrystalline surfaces show a ringed pattern and amorphous surfaces show almost no pattern at all (Figure 3-8).

3.2.2 Transmission Electron Microscopy: TEM

One of the most powerful microstructural analysis techniques available is transmission electron microscopy (TEM). From TEM, not only can the microstructure of an epitaxial film be determined, but also detailed analysis of defects in the film, atomic imaging of the interface, and an accurate calculation of lattice spacing is determined. TEM uses a beam of electrons that pass through and interact with a very thin sample to form an image on the other side of the sample (Figure 3-9). The interactions between the atoms in the sample and the electrons produce the contrast seen in the image. One of the major drawbacks of TEM is sample preparation required to obtain the images. The sample must be cut, polished, and thinned to electron transparency (~100 nm) via hand polishing and ion beam milling or by using a focused ion beam (FIB) system. A complete description of the sample preparation is given in Appendix B. This is especially difficult for the nitride materials due to their hardness. The FIB used to make

these sample was a FEI Strata DB (Dual Beam) 235 FIB. A JOEL 200CX operating at 200 keV was used for film analysis and JOEL 2010FX operating at 400 keV was used for high-resolution analysis of the interface.

3.2.3 X-Ray Diffraction: XRD

Another structural analysis technique is x-ray diffraction (XRD). This technique had virtually no sample preparation when compared to TEM. X-rays are diffracted off the sample to produce characteristic peaks of the atomic planes in the sample. The full width at half maximum (FWHM) of these characteristic peaks is used to determine the crystalline quality of the films. Powder x-ray diffraction can be used if the samples are polycrystalline or polycrystalline/amorphous. This was used in preliminary sample analysis to determine if second phases were present. X-ray reflectivity (XRR) from the air/film interface and the film/substrate interface help determine the roughness of these interfaces and the thickness of the film. The powder system is a Phillips 3720. The high-resolution system is a Phillips MPD 1880/HR with a 5-crystal analyzer. The x-ray source for both systems is a copper (Cu) Kα x-ray source. Figure 3-10 shows an illustration of the sample geometry for the x-ray diffraction. Samples were scanned measuring the Ω-2Θ with the GaN peak optimized for the high-resolution system. For the powder system, peak intensity- 2Θ was measured. For the x-ray scan, the 2Θ peak positions are obtain and using Bragg's Law, Equation 3-2, the d-spacing between the corresponding planes are calculated.

$$n\lambda = 2d \sin \Theta \tag{3-2}$$

Here, λ is the wavelength of the incident x-ray, d is the spacing between the planes, and Θ is the measured peak position. The d-spacings are compared to known values of the material to determine crystal orientation.

3.2.4 Atomic Force Microscopy: AFM

The surfaces of the grown films were characterized using atomic force microscopy (AFM) to give a quantitative analysis of film morphology or surface roughness. Tapping mode AFM was used to obtain a root mean square (RMS) roughness of the surface. In tapping mode, the tip of a stylus, made from Si_3N_4, is brought into close proximity to the surface, close enough to be defected by van der Waals forces of the surface atoms. A laser is reflected off the AFM tip and collected into a photodiode (Figure 3-11). The intensity of the reflected light is read as height. The tip is rastered across the surface and each point is read as a height, creating a 3-dimensional map of the surface. From this 3-dimensional map, a surface roughness is calculated and from this a RMS roughness. This is very useful in characterizing the starting substrate, the dielectric film, and the effects of the various growth and processing steps. The sensitivity of the AFM is largely dependent on the sharpness of the tip and the sensitivity of the deflection. The tapping mode tip used here has a tip radius of 5 nm and the deflection sensitivity is about 0.01 nm. This makes tapping mode extremely sensitive to surface roughness. An alternative mode of operation is contact mode. However, the tip radius is about 20 nm, which greatly reduces the resolution. The AFM used in this study was a Digital Instruments Nanoscope III.

3.2.5 Scanning Electron Microscopy: SEM

The surface morphology of the samples is characterized on the macro level by using the secondary electron microscope (SEM). The SEM technique enables an image of the surface to be taken at very high magnifications, from between 5000X to 100,000X. In this technique, an electron beam of energy between 5 keV and 30 keV is rastered across the sample surface. A schematic of the SEM is shown in Figure 3-12. One requirement of an SEM sample is that the surface be conducting in order to prevent

surface charging due to interaction of the beam with the sample. In the case of insulating samples a thin carbon film is applied or beam conditions are used that reduce surface charging. The interaction of the beam with the sample produces several different species at differing depth within the sample including secondary electrons, Auger electrons, backscattered electrons, and characteristic x-rays. Secondary electrons have energies below 50 eV, and due to this low energy can only escape from the sample if they are produce within a few nm of the surface. As the electron beam is rastered, a detector picks up the secondary electron signal. This signal is fed into a cathode ray tube that is scanned at the same rate as the beam, producing an image (Figure 3-13).

The SEM used in this research is a JOEL 6400. The technique gives a qualitative analysis of the surface, indicating the overall surface morphology of the film. This is important for future processes in fabricating capacitors and MOS(MIS)FET's, since device processing requires annealing, etching, and metal deposition, all of which are sensitive to surface morphology. SEM can also be used to look at the surface topography, which should determine how well the surface is covered and see any obvious defects and pin holes.

3.2.6 Auger Electron Spectroscopy: AES

Auger electron spectroscopy (AES) was used to determine qualitatively the elements present in the grown dielectrics. Auger electrons are also emitted from the sample during the electron/sample interaction (Figure 3-14). An incident electron strikes an inner shell electron of an atom and ejects that electron. An upper shell electron fills the void and energy is given off in the form of an Auger electron. The Auger electron is specific in energy to the element it came from and is thus a characteristic electron to that element. The Auger electrons are collected and an elemental analysis of the surface is

obtained. The AES technique can detect elements down to the alloy level (~1%) within the top 1.0 nm of the surface. Auger electrons are produced throughout the interaction volume of the incident electrons, however, because of their low energies, only those produced near or at the surface can escape. From the ratio of the peak heights from each element and published sensitivity factors, an approximate ratio of elements can be determined. A Perkin Elmer 660 AES was used for these measurements. This system is also equipped with an ion gun for creating depth profile Auger electron spectra. From this, changes in the element ratios perpendicular to the interface and the interface itself can be studied. This will help in determining if film composition is constant throughout the film and if there is segregation in the film. Also, approximate film thickness can be determined from known standards.

3.2.7 Ellipsometry

Ellipsometry is used primarily to determine the thickness of thin dielectric films on highly absorbing substrates but can also be used to determine the optical constants of films or substrates. Ellipsometry is based on measuring the state of polarization of polarized light. When light is reflected from a single surface it will generally be reduced in amplitude and shifted in phase. For multiple reflecting surfaces, the various reflecting beams will further interact and give maxima and minima as a function of wavelength or incident angle. Since ellipsometry depends on angle measurements, optical variables can be measured with great precision, being independent of light intensity, total reflectance, and detector-amplitude sensitivity. A general schematic of the machine is in Figure 3-15. For further explanation of ellipsometry see Appendix A. The ellipsometer used for this experiment is a JA Woollam Variable Angle Spectroscopic Ellipsometer.

3.2.8 Current-Voltage (I-V) measurements

Current-voltage measurements were made using a Hewlett Packard Model 4145. In these measurements, the current is set to an upper and lower limit, typically 5μA to10μA and the voltage is swept from negative to positive. The voltage range is increased until the forward and reverse breakdowns are reached. The current limit is then set to 1mA and the voltage is measured again. The voltage at 1 mA is divided by the dielectric thickness and the breakdown field strength is obtained. This is one parameter used in defining the quality of the dielectric film. This helps to determine the breakdown field of the dielectric at elevated temperatures. There is a heated stage with the current-voltage measurement equipment with a maximum temperature for testing of the 300ºC. This was used to study the dependence of the temperature with the breakdown of the dielectric.

Ohmic contacts were made to the silicon substrates using a Pt/Au (300 Å /1000 Å) bilayer structure using electron beam evaporation. Ohmic contacts made to the gallium nitride were made using a multiplayer structure of Ti/Al/Pt/Au with the following thicknesses- 20 nm Ti /70 nm Al/40 nm Pt /100 nm Au. The contacts on the GaN were annealed for 30 seconds at a temperature of 450ºC in a nitrogen ambient. Contacts on the dielectric were Pt/Au and were deposited through a shadow mask with varying contact sizes. The most commonly used contact sizes were 50 μm and 80 μm.

3.2.9 Capacitance-Voltage (C-V) measurements

Capacitance-voltage measurements were made using a Hewlett Packard Model 4284. Here a bias of 2 to 20 volts is applied across the capacitor and cycled at a selected frequency, typically 100 Hz to 1 MHz, and the resulting capacitance is recorded. From capacitance-voltage plots, the flat band voltage shift, dielectric constant, and interface

state density can be calculated. Calculating the carrier concentration of the substrate from the data obtained can test the accuracy of these measurements. This carrier concentration should match the quoted value from the manufacturer.

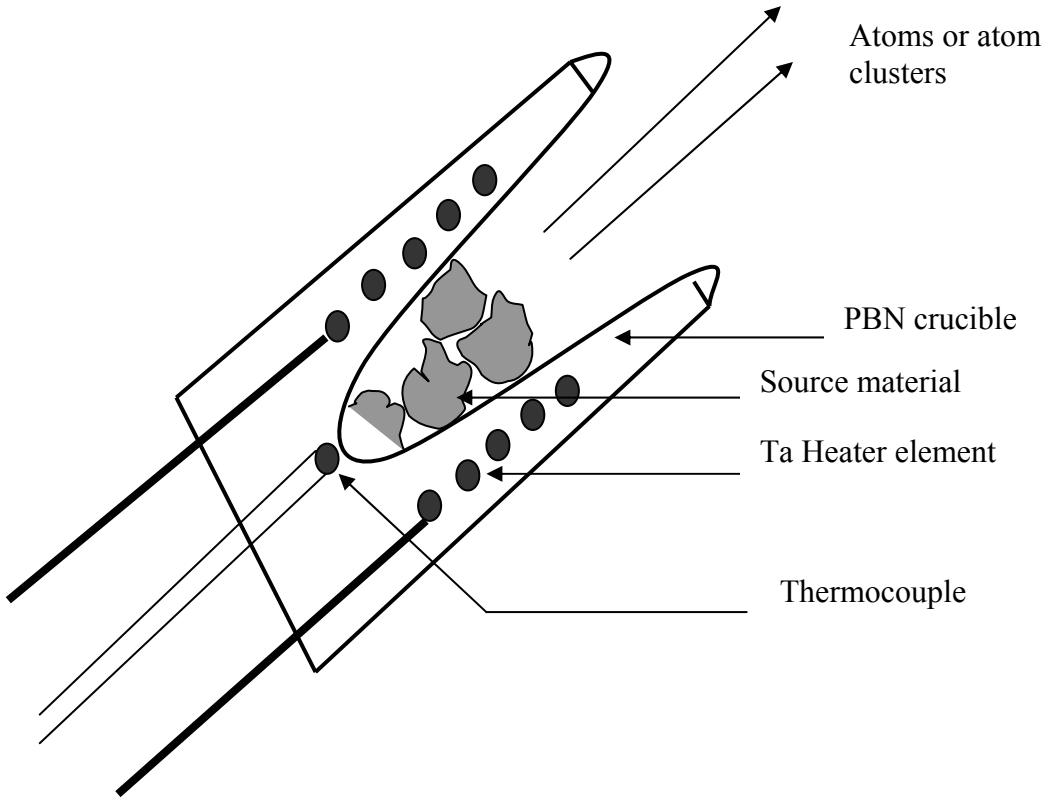

Figure 3-1. Typical Knudsen effusion oven (After B.P. Gila 2000).

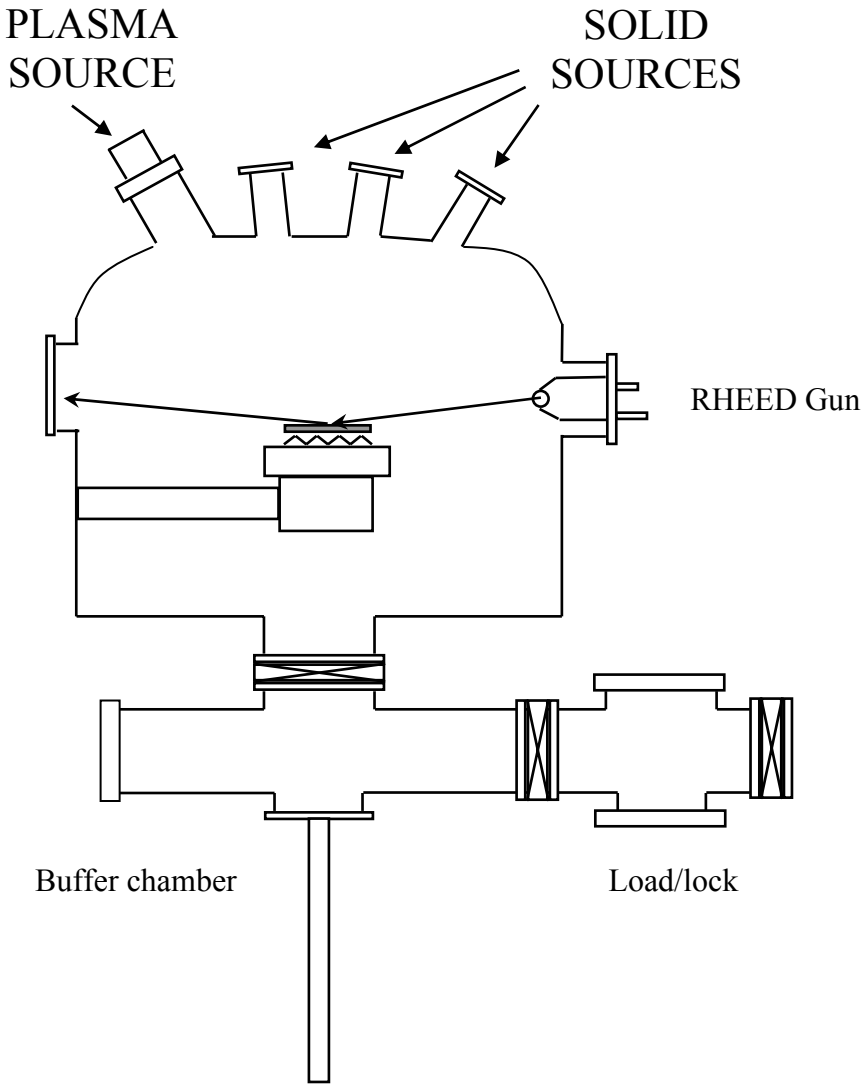

Figure 3-2. Riber MBE used for oxide growth.

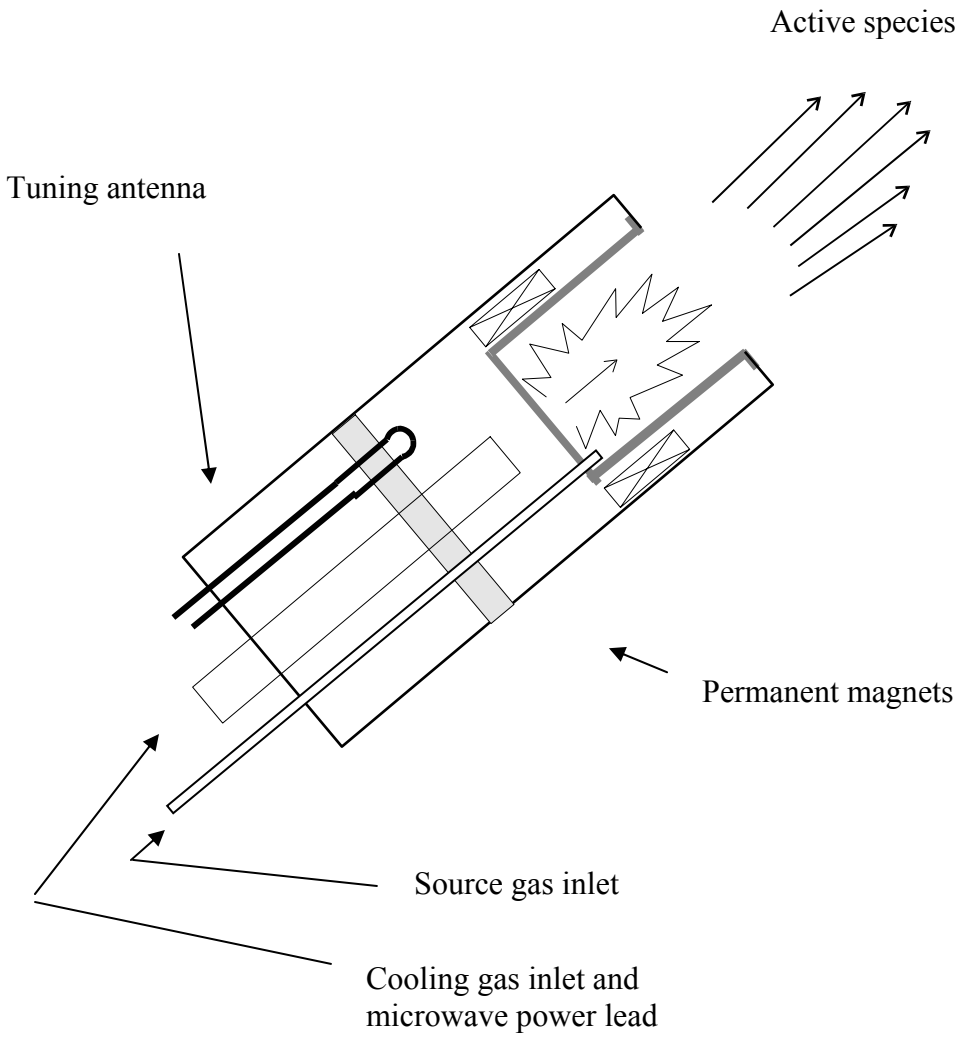

Figure 3-3. WaveMat 610 ECR plasma head.

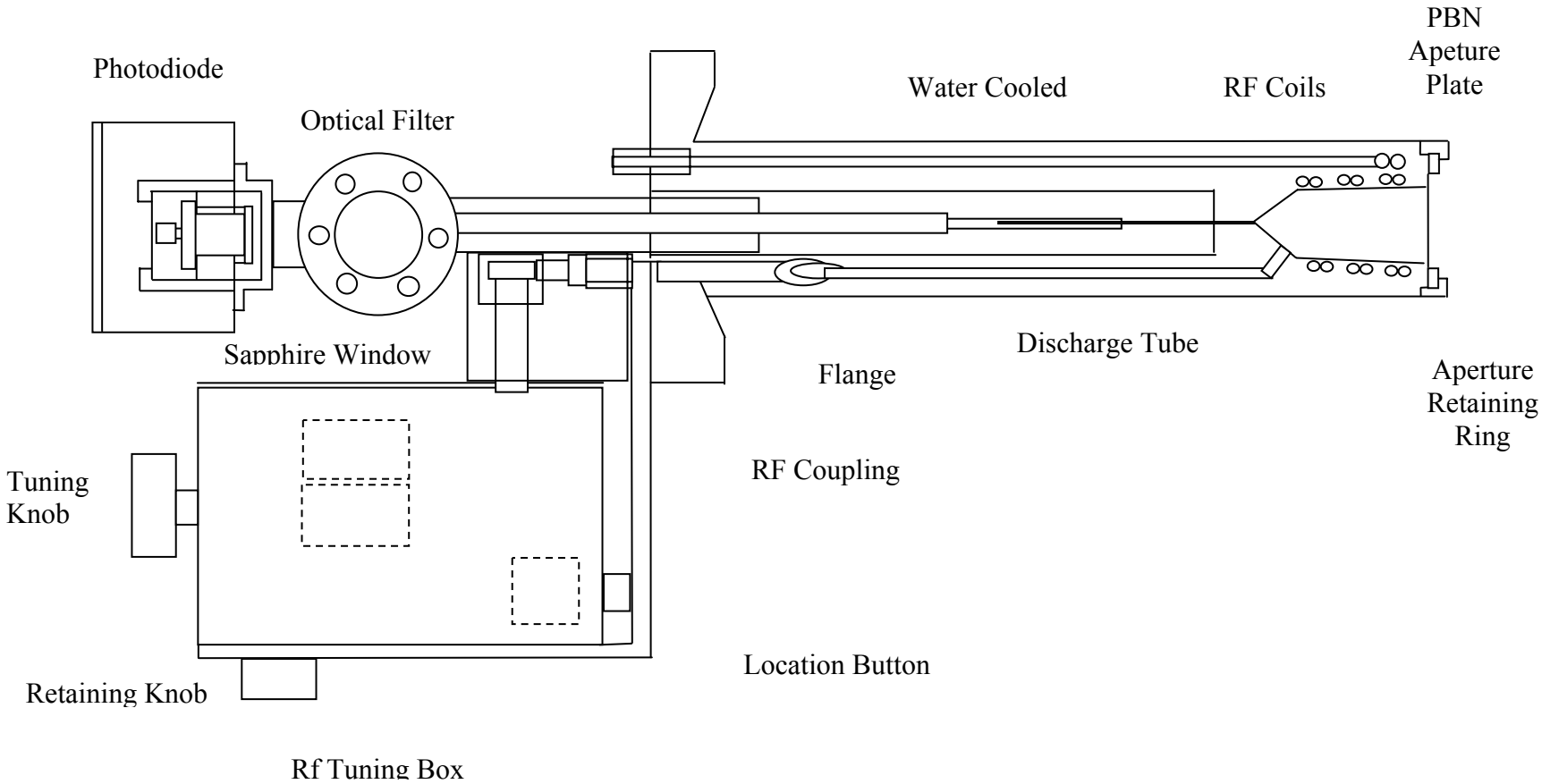

Figure 3.4. Schematic of the Oxford RF plasma source (After MDP21S Operating and Service Manual 1989[73]).

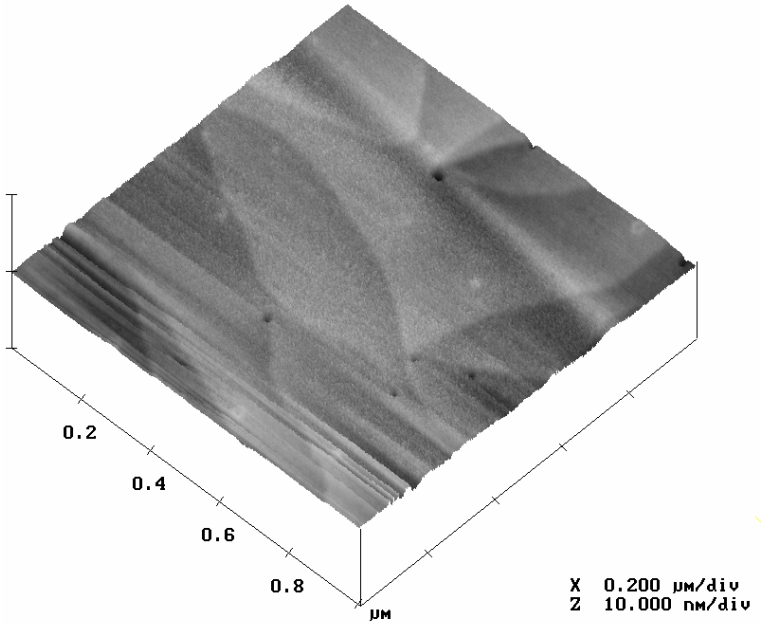

A

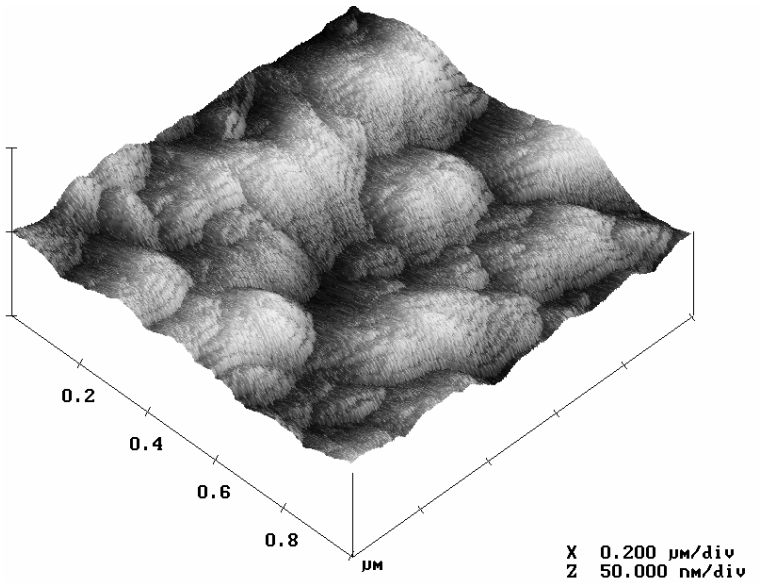

B

Figure 3-5. AFM images of as received A) MOCVD GaN from Epitronics, and B) as received MBE GaN from SVT.

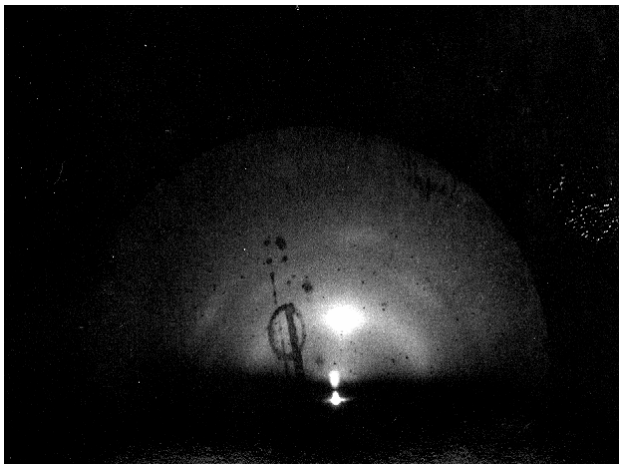

A

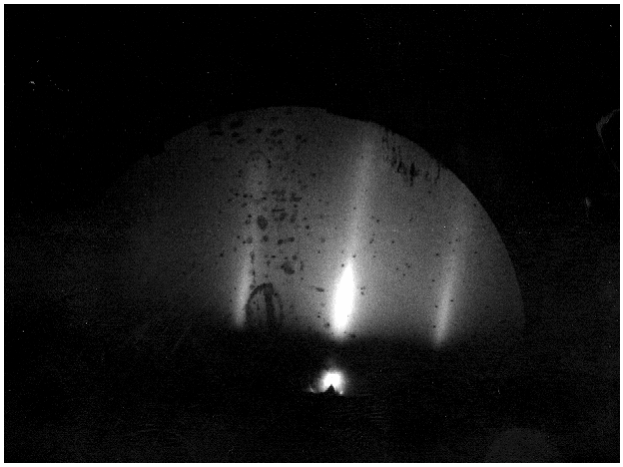

B

Figure 3-6. RHEED images showing A) the UV-ozone treated surface of MOCVD grown GaN and B) the buffered oxide etched UV-ozone surface of GaN.

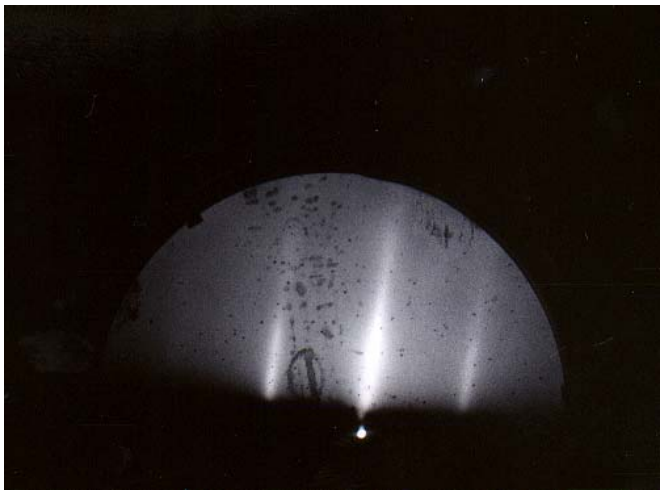

A

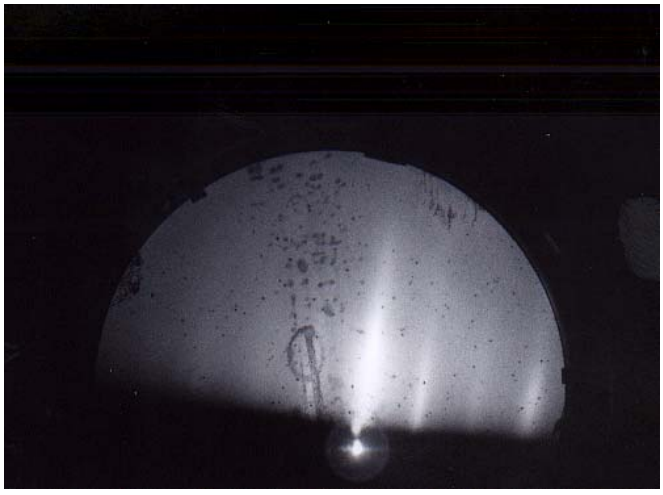

B

Figure 3-7. RHEED photos indicating a (1x3) pattern. The top photo is along the <11-20> crystal direction and the bottom photo is along the <1-100> crystal direction.

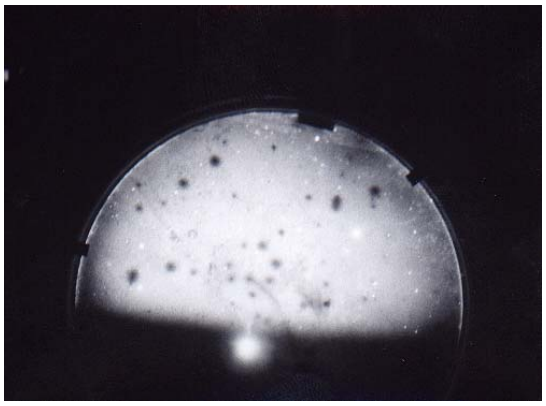

A

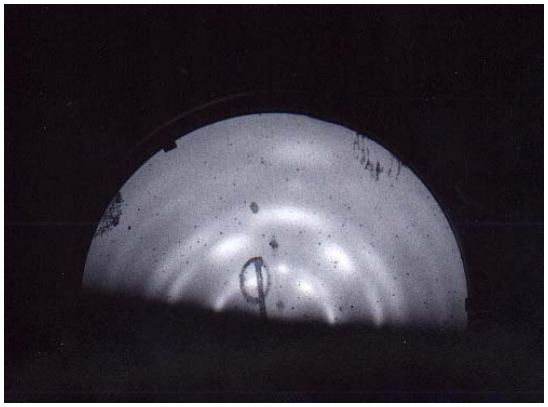

B

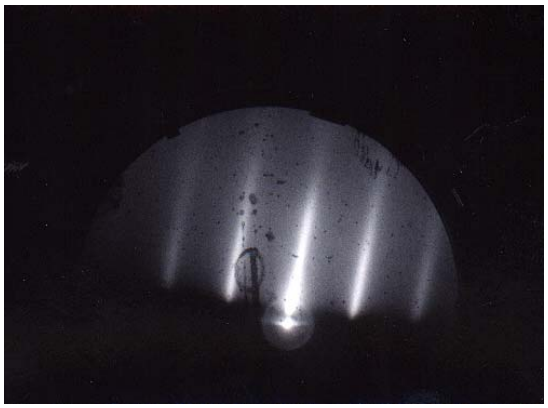

C

Figure 3-8. RHEED photos showing A) an amorphous diffraction pattern, B) a polycrystalline diffraction pattern, and C) a single crystal diffraction pattern.

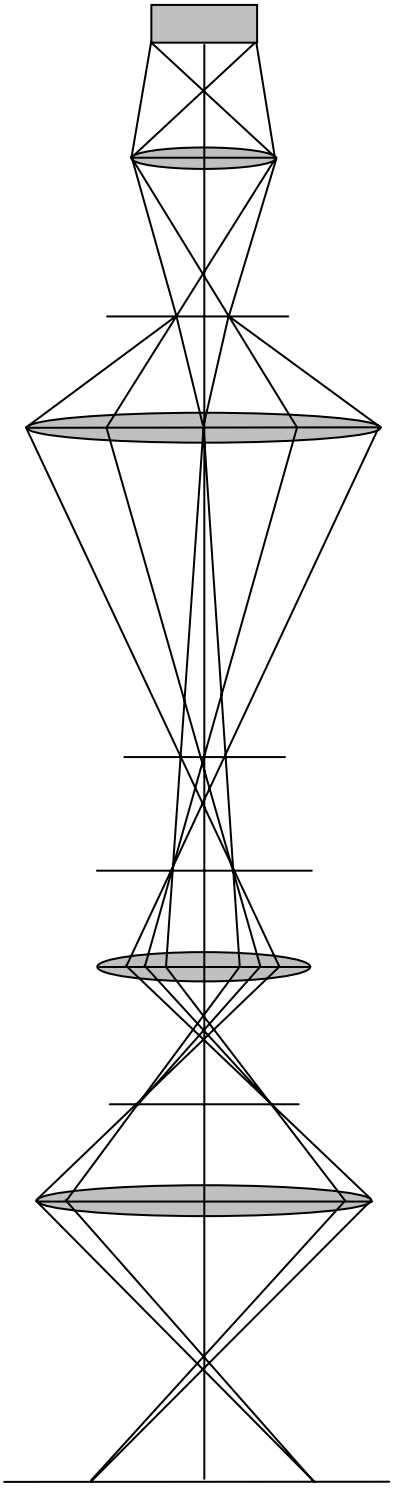

Figure 3-9. TEM column.

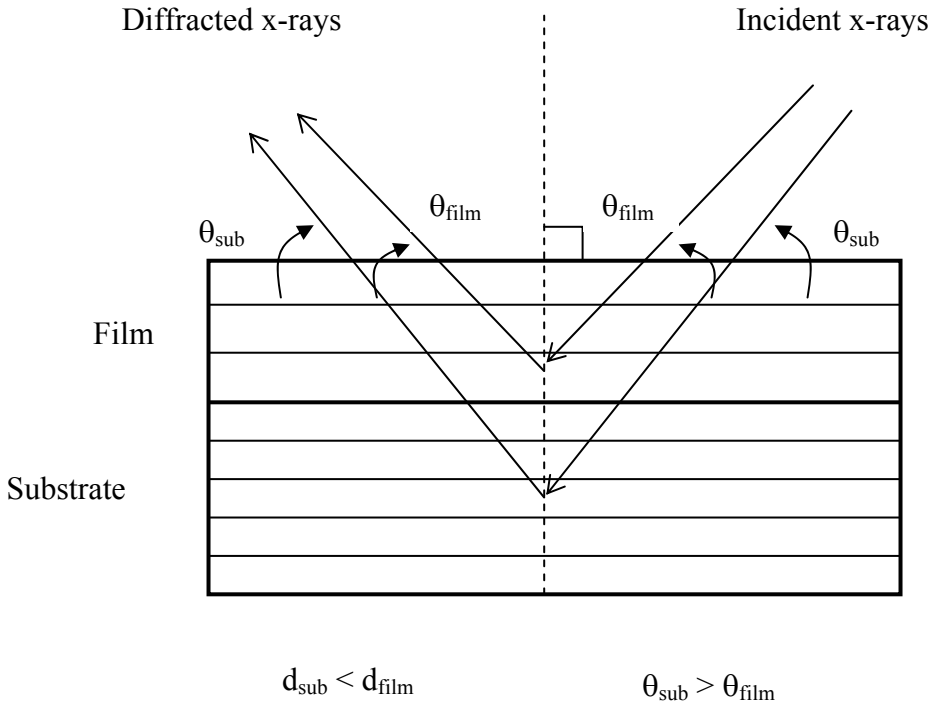

Figure 3-10. The relation between the lattice parameter and Bragg angle for film and substrate.

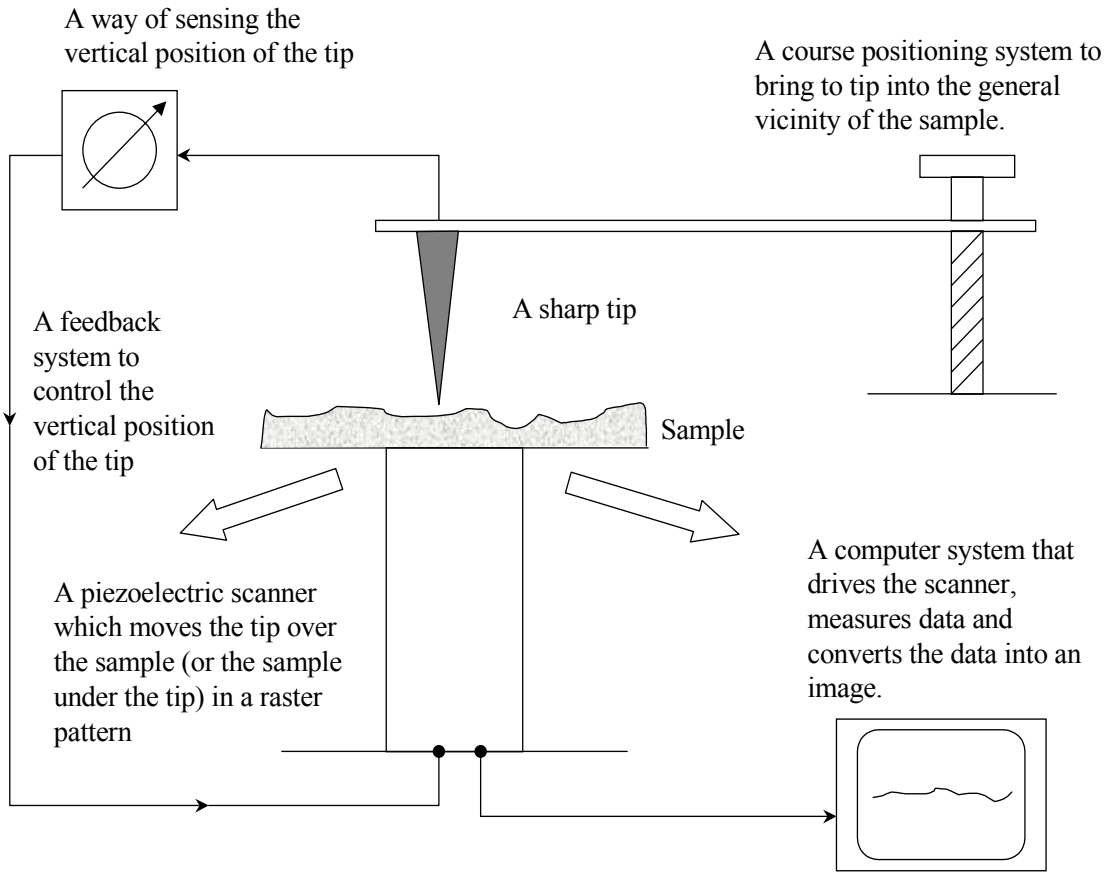

Figure 3-11. Atomic force microscope (after K.K. Harris 2000).

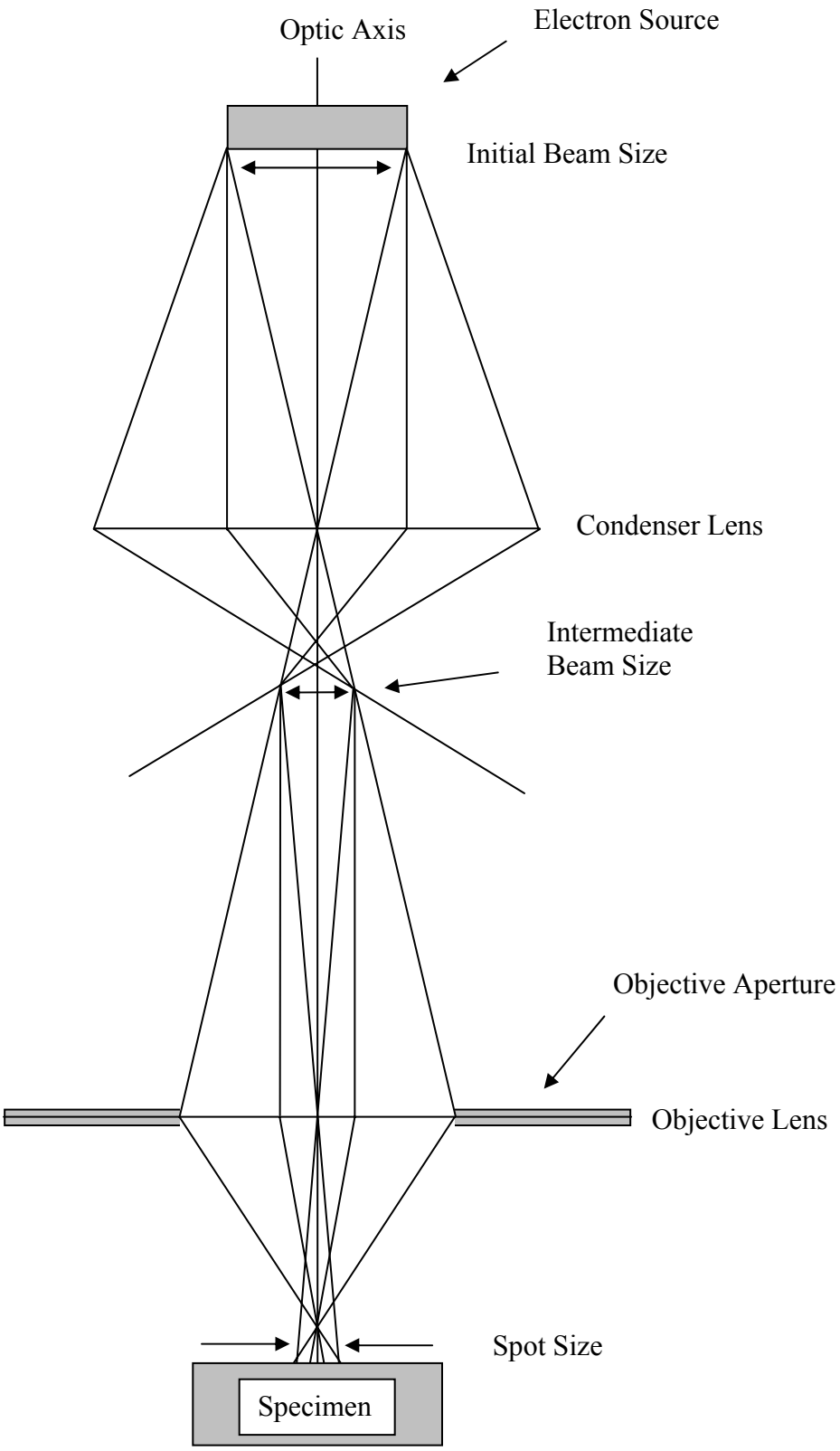

Figure 3-12. Schematic of SEM column.

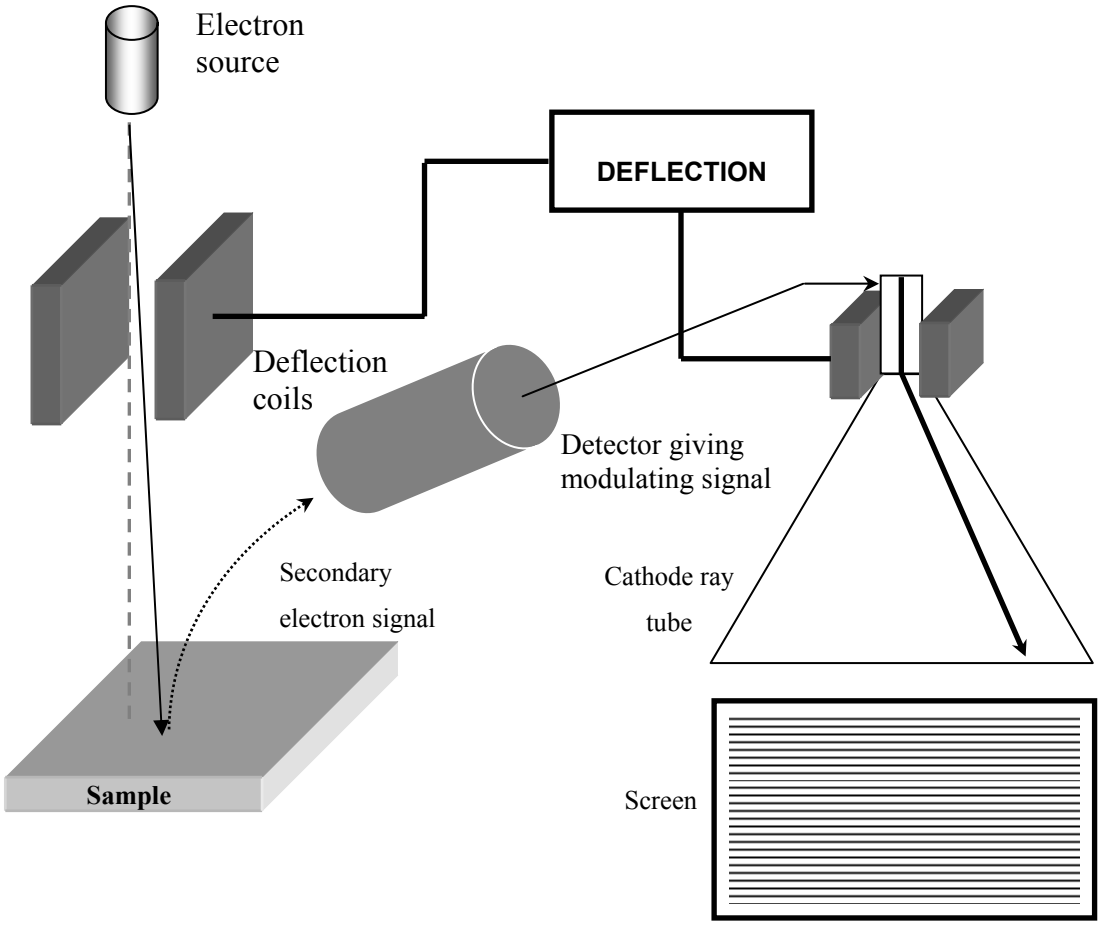

Figure 3-13. SEM operation. Electron beam is rastered over the sample producing secondary electrons (after S.M. Donovan 1999).

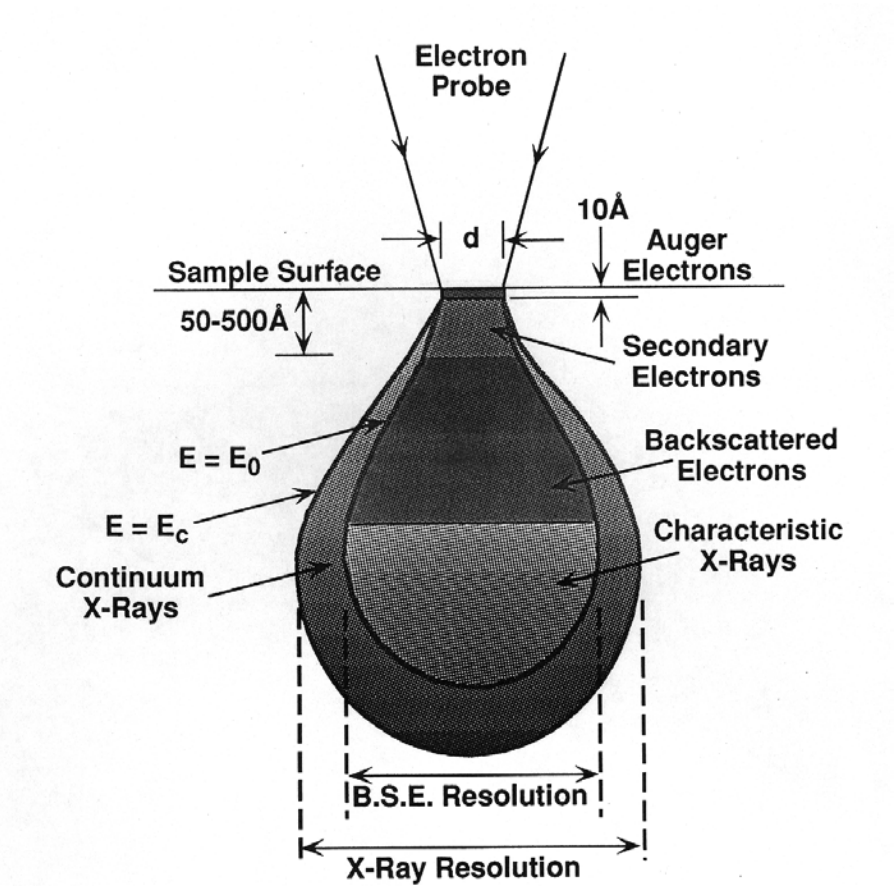

Figure 3-14. The penetration depth and interaction of an electron beam in a material. Notice that Auger only escape the top 1.0 nm (after Goldstein).

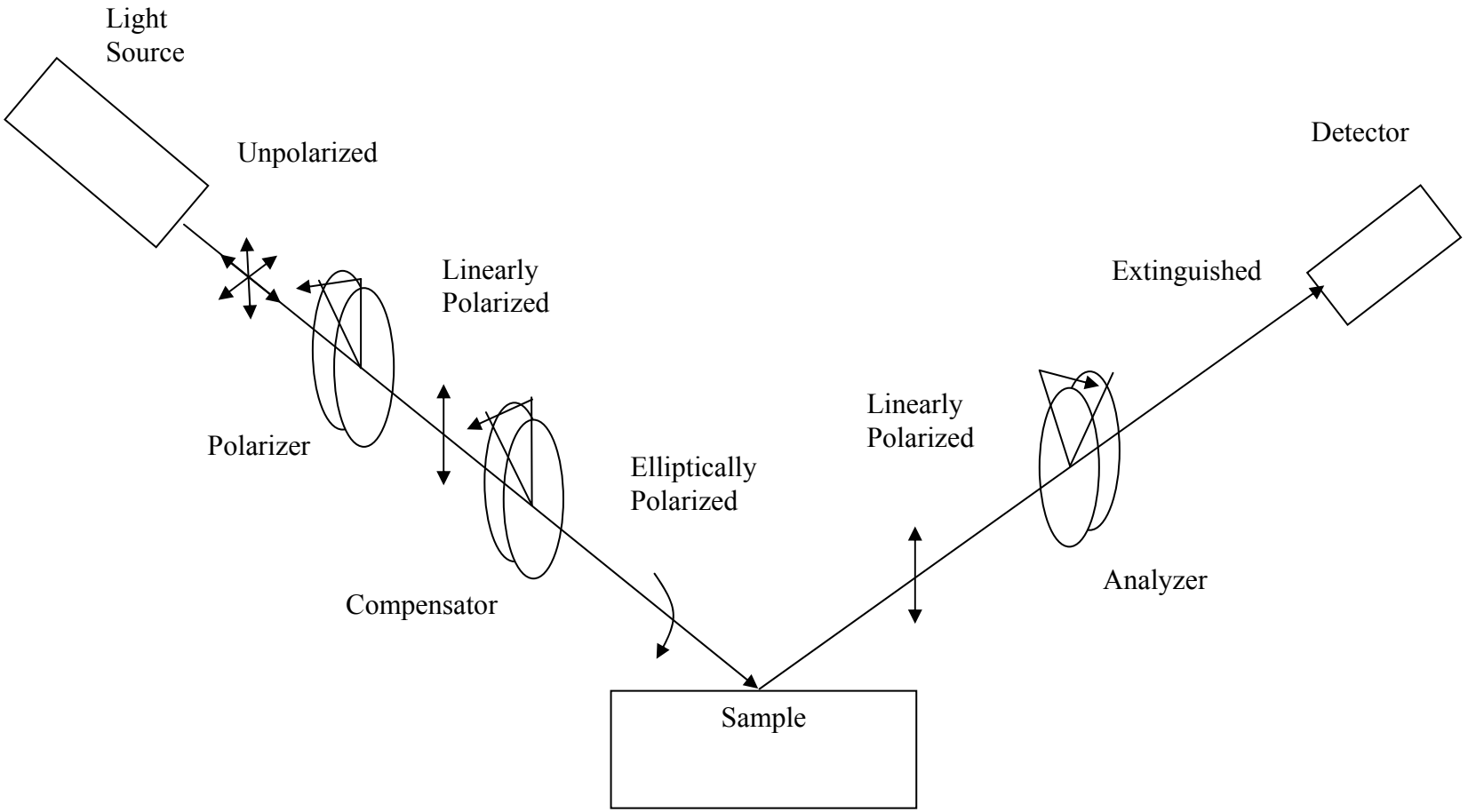

Figure 3-15. Ellipsometer schematic (After D.K Schroder[74])

CHAPTER 4
MAGNESIUM OXIDE: RESULTS AND DISCUSSION

Magnesium oxide was chosen as a possible dielectric material for GaN because of its high melting point (2850°C), large band gap (7.3 eV), large dielectric constant (9.8) and good band offsets with GaN. The structure of MgO is the NaCl crystal structure[75] (Figure 4-1). This is a cubic structure with a lattice constant of 4.20 Å. The symmetry alignment for MgO:GaN is the MgO (111) and the GaN (0001). The cation spacing for the MgO (111) plane is 2.97 Å and for the GaN (0001) plane is 3.19 Å which gives a mismatch of -6.9% (Figure 4.2).

4.1 Effect of Oxygen Plasma Source

Many factors affect the growth of MgO such as oxygen source, oxygen pressure, substrate temperature, and plasma power. Initial work was carried out using an ECR plasma head for the oxygen source. Samples grown using a substrate temperature of 350˚C and a cell temperature, $T_{Mg,}$ of 340˚C, showed spotty RHEED diffraction patterns (Figure 4-3). As seen in this series of images, the pattern changed from streaky pattern, indicative of the single crystal GaN surface, to a broken line pattern indicative of a roughened surface. The surface diffraction also showed 6-fold symmetry indicating that the MgO grew with the (111) plane parallel to the GaN (0001) basal plane. During growth the pattern changed slowly until at the end of 120 minutes of growth, the pattern was highly three-dimensional and showed arcs associated with a polycrystalline pattern. This indicates that the initial layers were single crystal and that the microstructure gradually changed to polycrystalline as more layers were deposited. Using a

profilometer, the film thickness was measured to be 150 nm, yielding a growth rate of ~1.25 nm/min. From XRD results, the MgO film was found to be cubic and oriented with the (111) direction normal to the surface. Needle-like structures were observed on the surface by SEM (Figure 4-4) and the sample surface had an AFM root-mean-square (RMS) roughness of 4.07 nm (Figure 4-5). These needle-like features were found to decrease with increasing film thickness.

Samples grown at a substrate temperature of 100˚C using the ECR plasma head were significantly different from those grown at 350˚C. Initiating growth on the same GaN surface, the films remained single crystal for 1-2 minutes (~2.5-5.0 nm), then a polycrystalline RHEED pattern began to form, Figure 4-6. This pattern remains for the duration of the growth. The polycrystalline RHEED pattern shows six-fold rotational symmetry, indicating that the film is textured towards the <111>. This polycrystalline pattern differs from the pattern obtained at 350˚C, in that the arcs are more pronounced and the spots are not visible. This suggests a less textured film with a smaller grain size. From an etch step measurement, a growth rate of 2.5 nm/min was calculated. The sample surface has an AFM RMS roughness value of 1.26 nm and a reduced number of needle-like features. These needle-like features are not visible on films with a thickness of 100 nm or more. From XRD measurements, the polycrystalline MgO films were confirmed to be highly oriented toward the (111) direction.

Diodes were fabricated from these materials to measure the electrical properties of the dielectric film and the dielectric/GaN interface. Ohmic windows were created by etching the MgO with dilute phosphoric acid. Ohmic contacts were made by e-beam evaporating Ti/Al/Pt/Au. The gate metal was Pt/Au with contact sizes ranging from 100-

50 μm. Because of the leaky nature of the single crystal MgO grown at temperatures of 350˚C, no C-V results could be measured. The leakage in these films could be due to the needle-like microstructure. For the polycrystalline MgO grown at 100˚C, a forward breakdown field of 2.3 MV/cm was measured at a current density of 5.1 mA/cm^2. From C-V measurements a corresponding interface state density of 4 x 10^{11} $cm^{-2}eV^{-1}$ was calculated for the diode using the Terman method. It is clear that the different microstructure obtained at the 100˚C is critical to improving the electrical behavior of the MgO dielectric. The combination the single crystalline interface and the polycrystalline material on top appears to produce a low interface trap density while at the same time eliminating the shorting paths obtained in the films which are mostly single crystal but highly defective.

When an RF plasma head was used as the oxygen source for MgO growth the materials properties improved further. For samples grown under the same conditions but with an RF plasma oxygen source, the needle-like microstructure was not observed. SEM and AFM also show a smoother surface, Figure 4-7. For these reasons, all further growths used the RF plasma head for the oxygen source and the ECR plasma head was removed from the system.

4.2 Effects of Oxygen Pressure

To study the effect of oxygen pressure on the properties of the growth of MgO, several different pressures were investigated- $1x10^{-5}$, $3x10^{-5}$, $7x10^{-5}$, and $1x10^{-4}$ Torr as measured by the beam flux monitor. The MgO flux was held constant. The higher oxygen pressures produced a decrease in the growth rate (Figure 4.9). From AES, the films were shown to contain only Mg and oxygen, with the Mg/O decreasing from 0.72 to 0.63 as the pressure was increased, (Figure 4.8). By comparison, the ratio of peak

heights of a standard single crystalline sample of MgO was measured and showed the ratio to be 0.60. The reduction in growth rates at higher pressures may be an indication of a reduction in the concentration of reactive oxygen species at the surface or of site blocking due to the higher concentration of oxygen incident on the surface. Both cases would result in a reduction in the Mg sticking coefficient. The lower Mg/O ratio at the higher pressures would seem to favor the site blocking explanation. AFM analysis indicated that as the pressure was increased the surface morphology became smoother, as evidenced by the decrease in RMS roughness from 0.998 nm at a pressure of $1x10^{-5}$ Torr to 0.247 nm at $1x10^{-4}$ Torr, (Figure 4-10). All of the films appeared smooth when examined by SEM. XTEM of the MgO grown at the lowest pressure showed that the initial 40 monolayers were epitaxial, with the remainder of the layer appearing to be fine-grained polycrystalline, (Figure 4-11). The precise microstructures of the films grown at higher pressure are not yet known. It is quite likely that given the superior morphology, these films retain their single crystal nature for a greater percentage of their thickness before becoming poly-crystalline.

From structural and compositional analysis it would appear that the higher pressures are beneficial to the growth of MgO layers. However, electrical characterization of the MgO/GaN diodes suggests the opposite, (Table 4-1). The breakdown field, V_{bd}, and the interface state density, D_{it}, improve with decreasing pressure. Ironically, the reduction in the dielectric strength may be due to the superior but not perfect microstructure in the films grown at higher pressures. Previous work with other dielectrics such as Gd_2O_3[49] has shown that if the layer does not contain a substantial polycrystalline region, then the breakdown field will be substantially lowered due to

leakage through the defects, which propagate through the layer. The presence of a nanocrystalline layer on top of the single crystal material at the interface appears to improve the breakdown strength of the layer in spite of the presence of numerous grain boundaries.

The effect of the pressure on the interface and the bulk charge densities suggests that the electrical behavior of the layer is enhanced by the presence of higher ion energy species at the surface. Since the total power to the plasma remains constant, increasing the oxygen flow will decrease the average energy per ion, and possibly decrease the concentration of ionized oxygen species as well. Studies with ECR plasmas suggest that the average ion energy is a critical parameter. ECR plasmas typically exhibit very low ion energies. MgO films grown using an ECR plasma with similar oxygen pressures to those in the RF grown films exhibit breakdown fields which are up to four times lower than those obtained with the RF plasmas. As the ion energy is increased, damage of the interface will eventually become a factor and begin to increase the density of interface states. Clearly, however, this does not occur at the standard pressures and powers used in this study, making the RF plasmas the optimum choice for the deposition of MgO dielectric on GaN.

4.3 Effect of Substrate Temperature

For MgO samples grown with the RF plasma at 300˚C, XRD shows a sharper peak, which indicates that the film grown at a substrate temperature of 300˚C is more crystalline than that grown at a substrate temperature of 100˚C, (Figure 4-12). AFM of films grown at 300˚C are rougher than films grown at 100˚C, (Figure 4-13). The RMS roughness of the 300˚C film is 1.998 nm while the 100˚C grown samples have RMS roughnesses of 1.334 nm. AES shows that the Mg/O ratio of the films deposited at 100˚C

is 0.75 while the 300˚C grown samples have an Mg/O ratio of 0.66. Single crystal MgO has a Mg/O ratio of 0.60 when investigated in the Auger system. This shows more incorporation of oxygen at a substrate temperature of 300˚C under the same oxygen flux and Mg flux. TEM of MgO grown at 300˚C (Figure 4-14) shows that the films is still epitaxial and is single crystalline for a greater thickness before rotation as compared to MgO grown at 100˚C, (Figure 4-11).

4.4 Scandium Oxide Capping Layer

Despite the positive aspects of MgO, it has been found to be environmentally unstable as shown by SEM, (Figure 4-15). The MgO films degrade over time in atmosphere due to the presence of water vapor.[76,77] From device processing, it does not appear that the MgO under the metal contacts degrades, only the areas exposed to atmosphere, (Figure 4-16). Capping layers of scandium oxide of various thicknesses have been tried in order to prevent this degradation. AFM shows that the capping layer smoothes the surface for both MgO grown at 100˚C and 300˚C. The RMS for MgO grown at 300˚C goes from 1.921 nm uncapped to 0.337 nm with a Sc_2O_3 cap of 20 nm, (Figure 4-17). For the MgO grown at 100˚C the RMS goes from 1.539 nm uncapped to 0.869 nm with a 20 nm Sc_2O_3 cap. The effect of the capping layer on the environmental stability of MgO is discussed further in Chapter 7.

Table 4-1. Electrical characterization of MgO/GaN diodes. V_{BD} was the applied voltage, which produced a leakage current of 1 mA/cm^2. D_{it} was the defect value at 0.4 eV below the conduction band calculated using the Terman method. The diode grown at 1x10^{-4} Torr was too leaky to be measured.

Oxygen Pressure (Torr)	V_{BD} (MV/cm)	D_{it} ($eV^{-1}cm^{-2}$)
$1x10^{-5}$	4.4	$3.4x10^{11}$
$3x10^{-5}$	4	$7.1x10^{11}$
$7x10^{-5}$	1.2	$1.8x10^{12}$

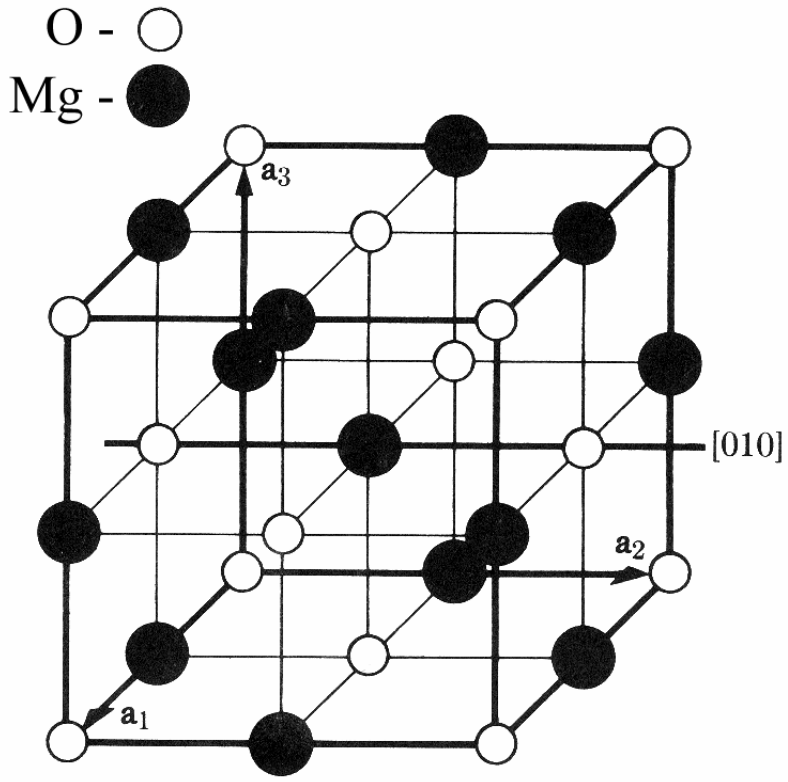

Figure 4-1. The MgO structure (from Cullity 1978[75])

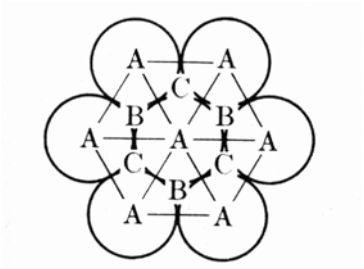

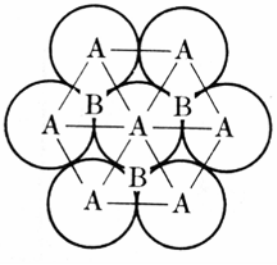

(111) (0002)

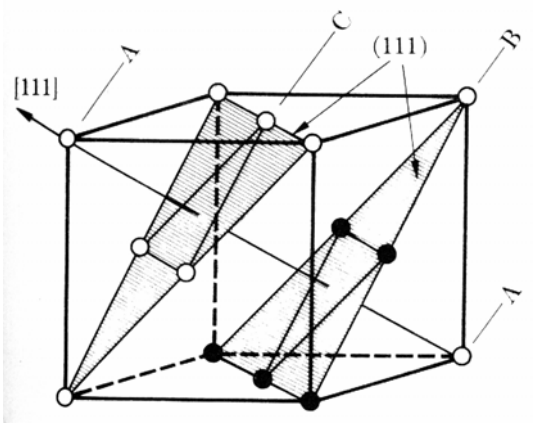

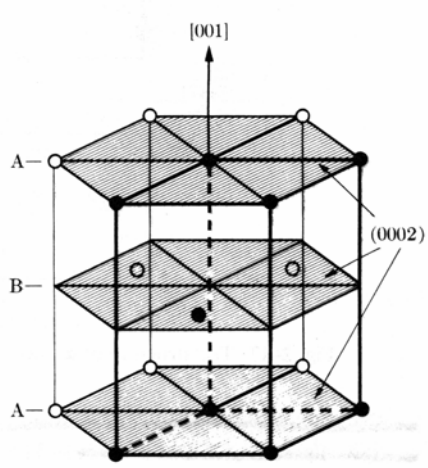

FCC **HCP**

Figure 4-2. Illustration showing the symmetry between the (111) NaCl plane and the (0002) wurtzite plane. The spacing between atoms marked A is 2.97Å for NaCl MgO and 3.19Å for wurtzite GaN. (from Cullity 1978)

A)

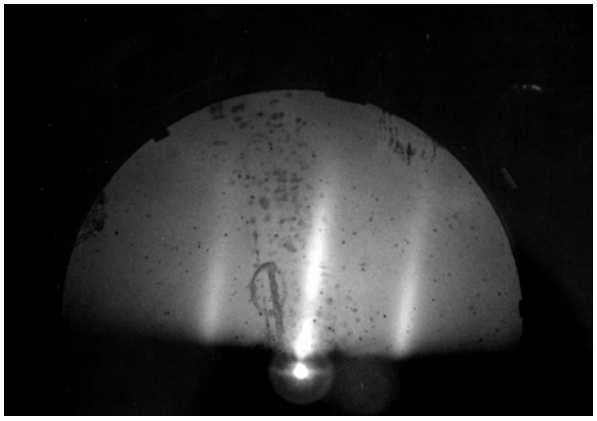

B)

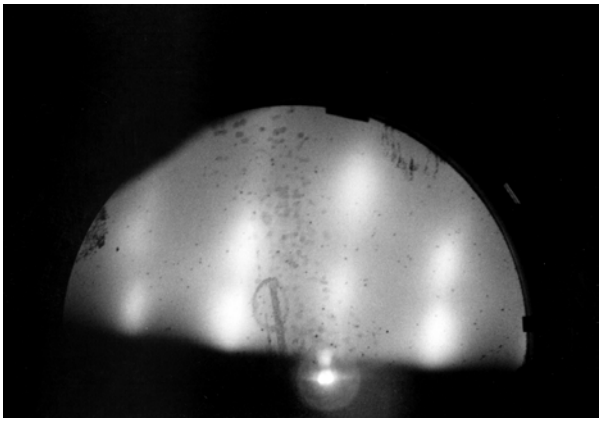

C)

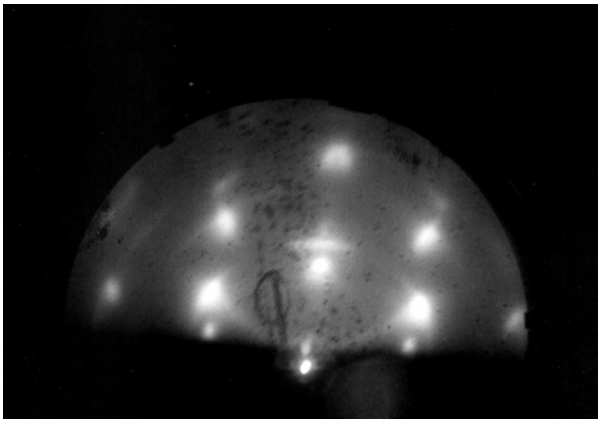

Figure 4-3. RHEED images indicating A) GaN at 350°C before growth, B) MgO after 1 minute of growth, and C) MgO after 120 minutes of growth at 350°C.

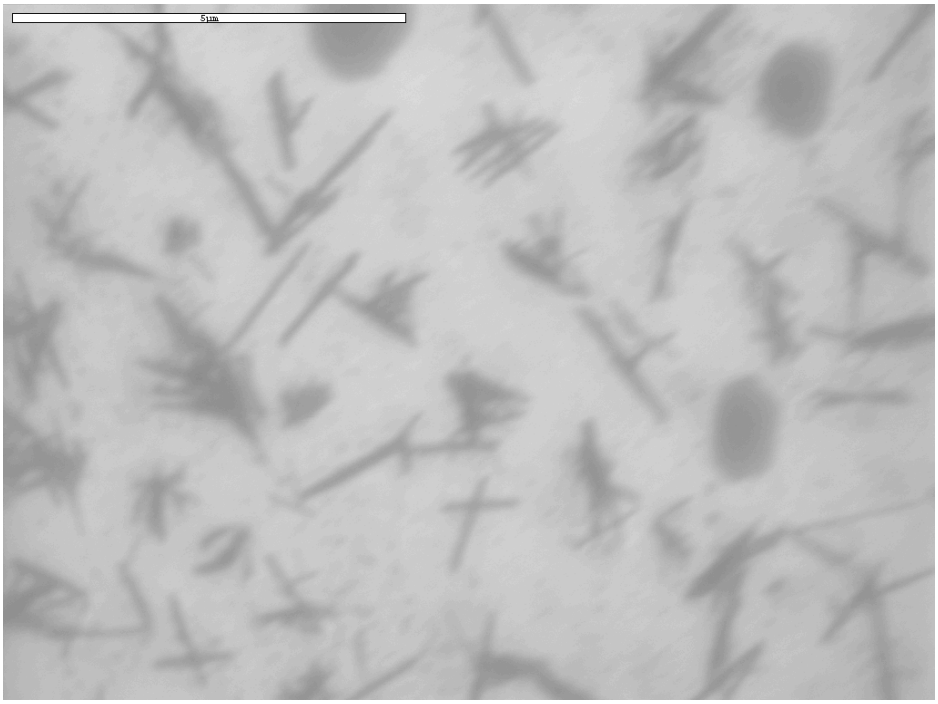

Figure 4-4. SEM image of the MgO surface grown at 350°C with ECR plasma source. Scale bar is 5µm.

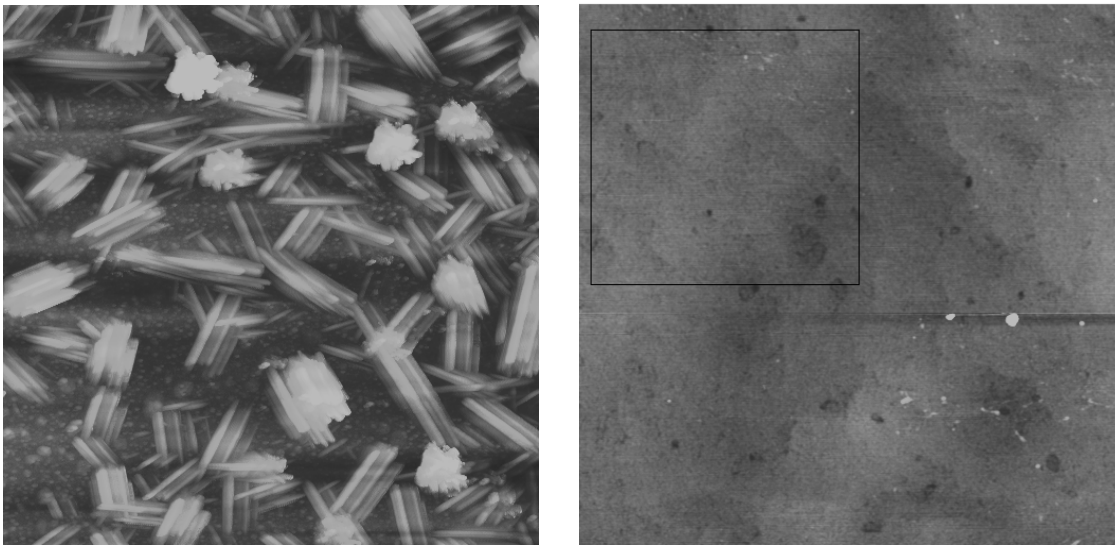

A) B)

Figure 4-5. AFM images of A) MgO grown at 350°C (4.07 nm RMS) and B) MgO grown at 100°C (1.26 nm RMS). Both films are grown with the ECR oxygen plasma source. Images are 5μm per side.

A)

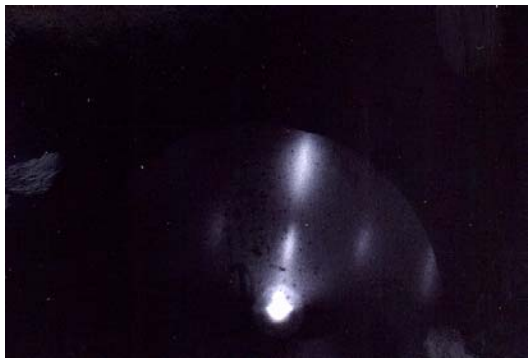

B)

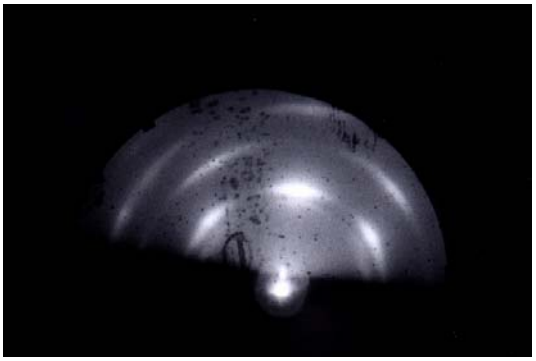

Figure 4-6. RHEED images indicating MgO after A) 1 minute of growth, and B) after 90 minutes of growth at 100°C.

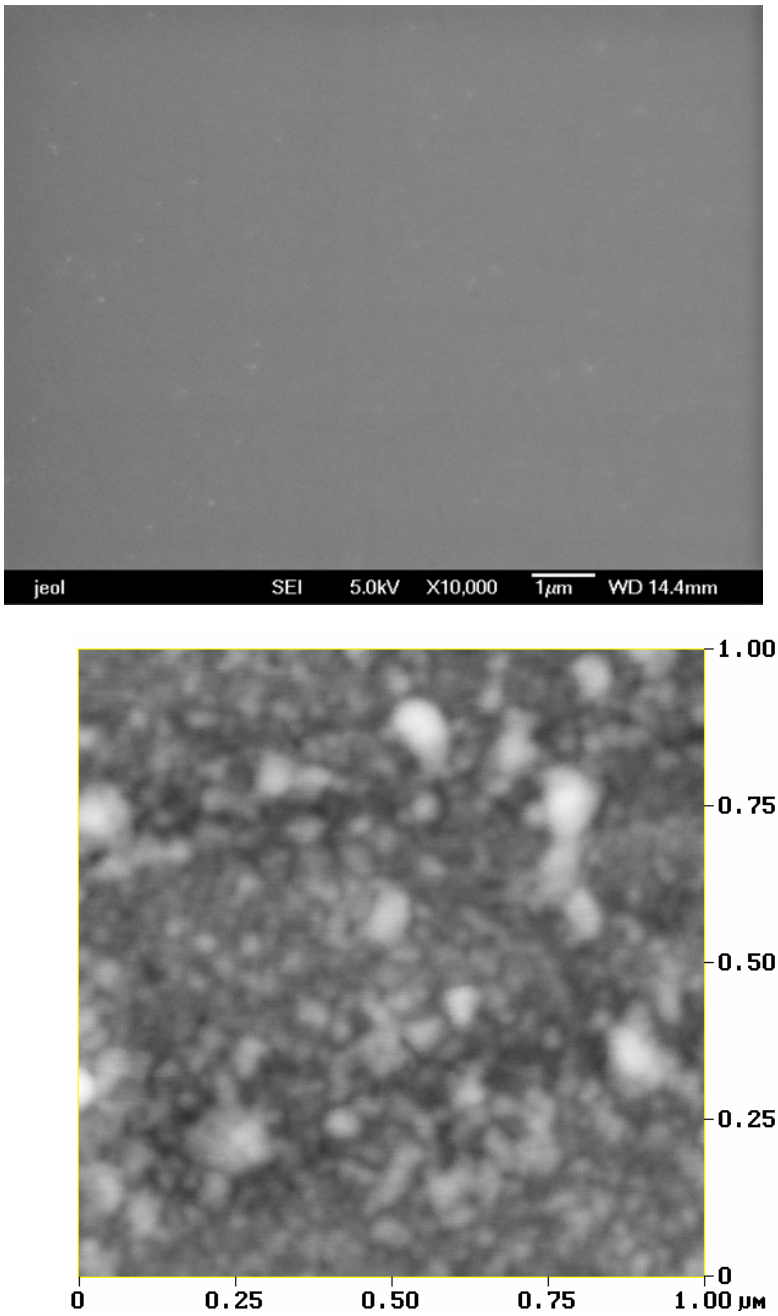

Figure 4-7. SEM, above, and AFM, below, of MgO grown at 100˚C with RF plasma source, RMS = 1.334 nm.

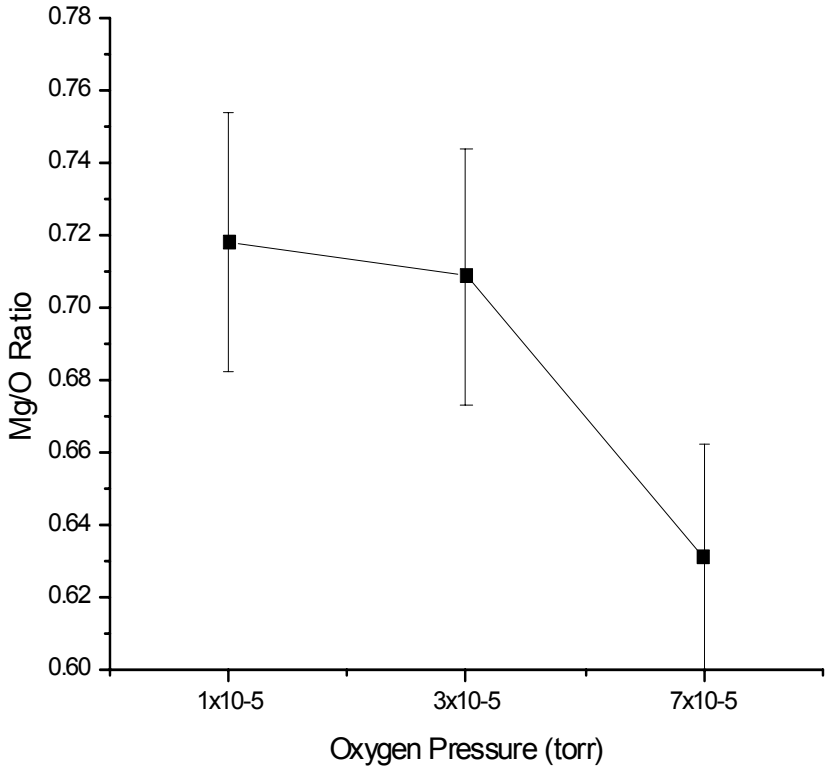

Figure 4-8. Mg/O ratio as determined by AES as a function of oxygen pressure.

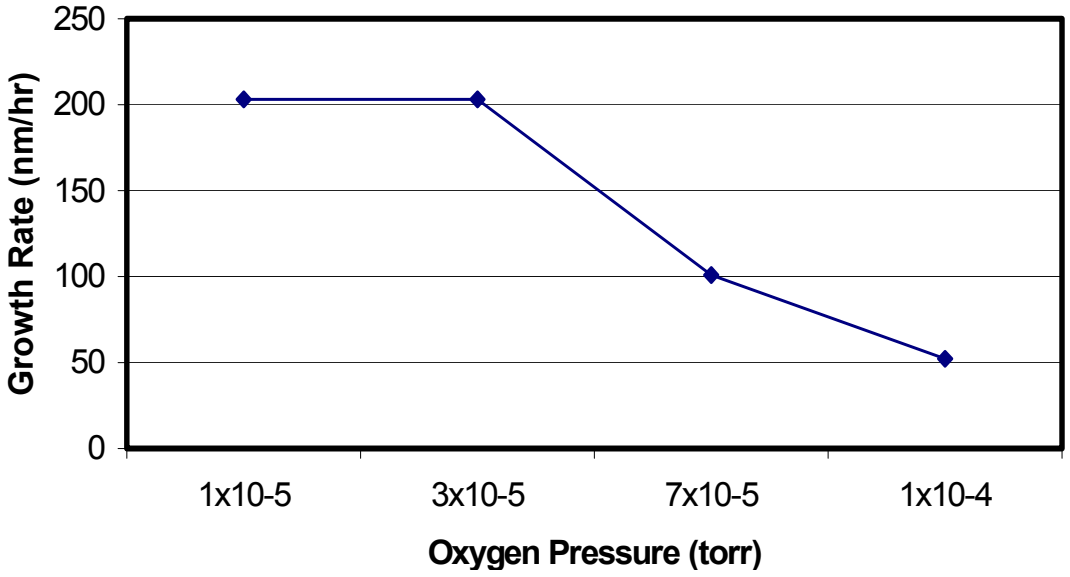

Figure 4-9. Dependance of growth rate on oxygen pressure

A)

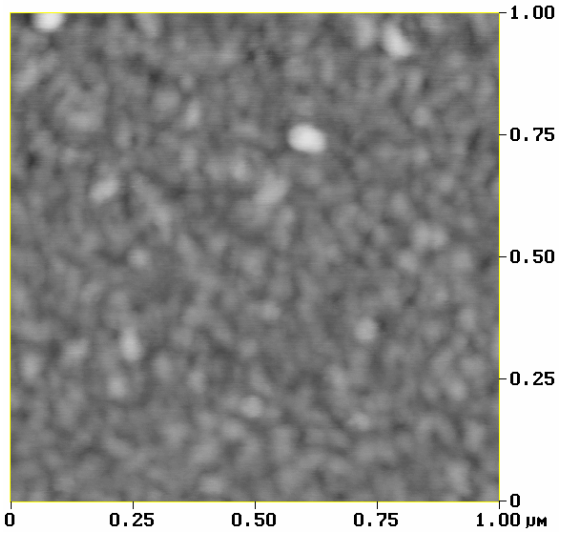

B)

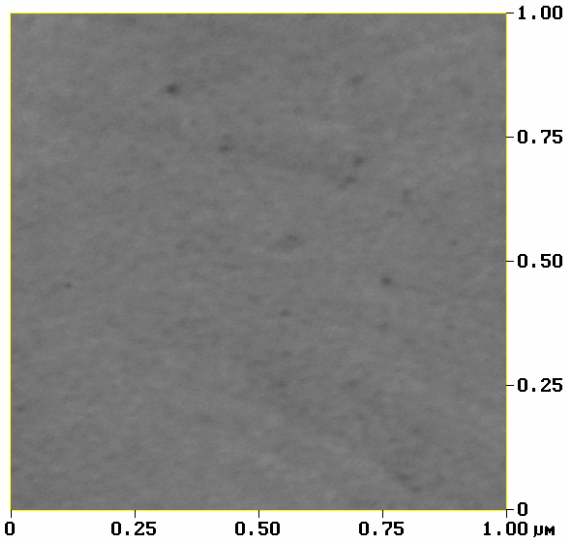

Figure 4-10. AFM scans of MgO grown at 100˚C using an oxygen pressure of A) $1x10^{-5}$ Torr, or B) $1x10^{-4}$ Torr. The RMS roughnesses were 0.998 nm and 0.247 nm respectively.

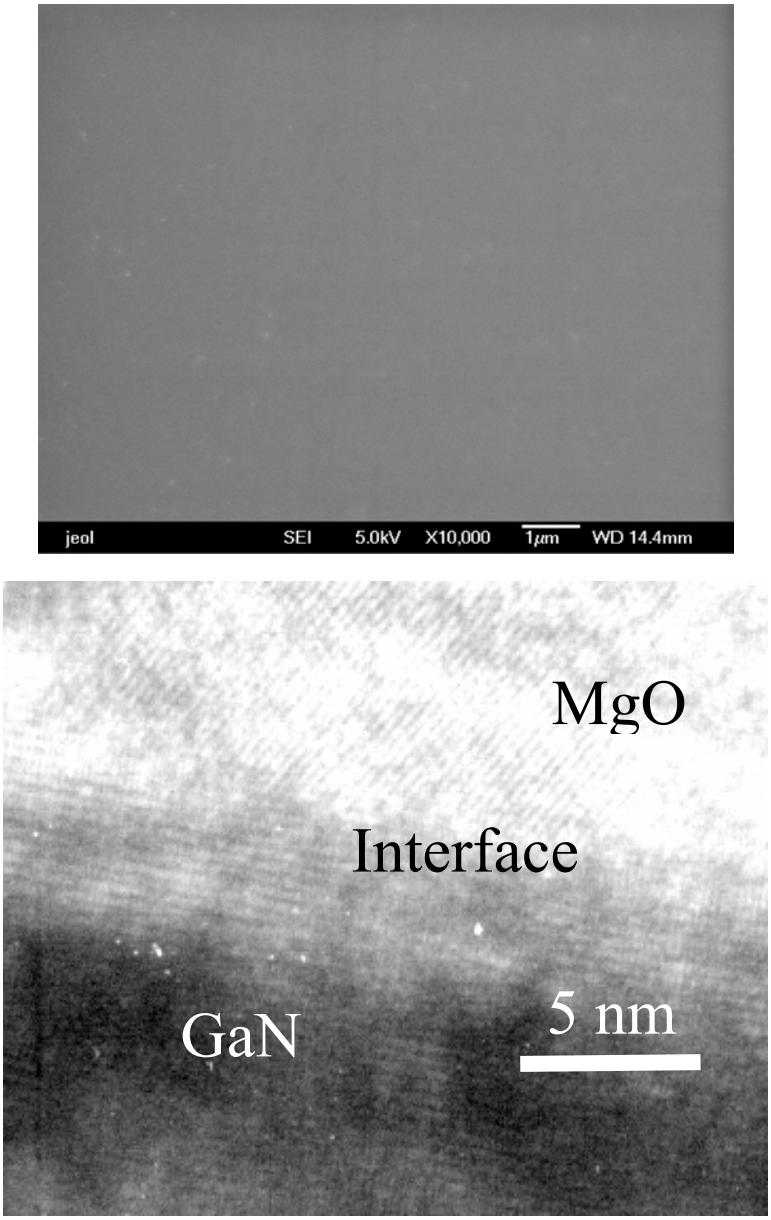

Figure 4-11. SEM and TEM of MgO. An SEM image (10,000x) of the MgO layer grown at $1x10^{-5}$ Torr is shown above and an XTEM image of the same layer is shown below.

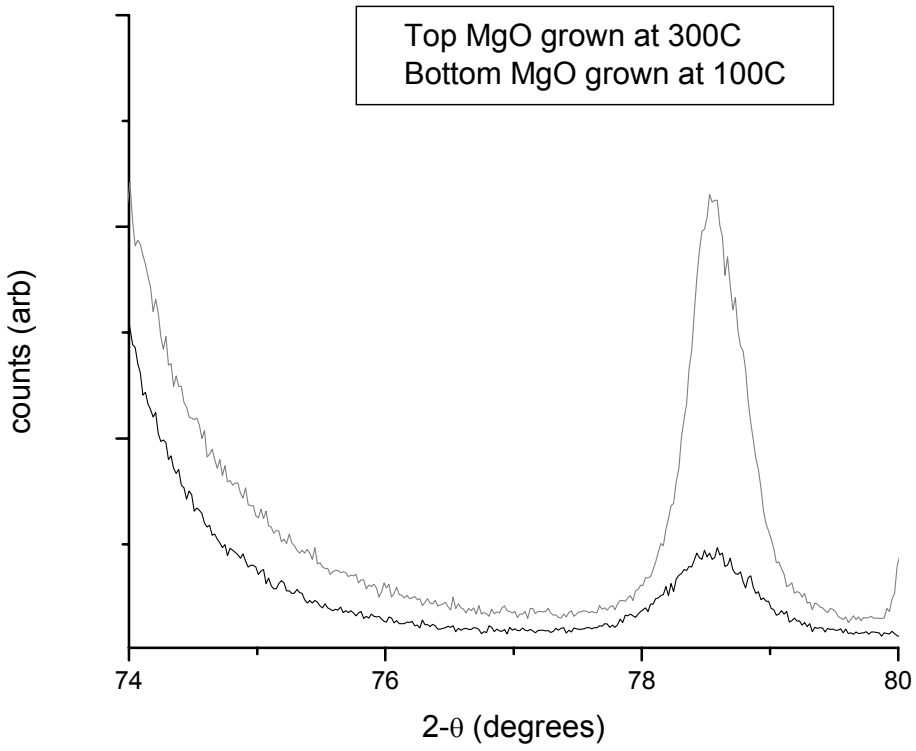

Figure 4-12. XRD shows that the MgO film grown at 300˚C has a much sharper peak than the MgO film grown at 100˚C.

A)

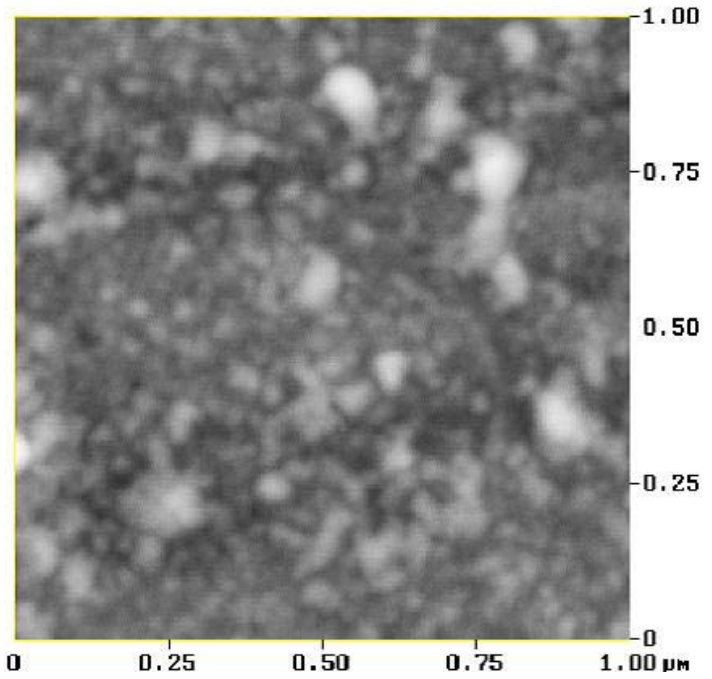

B)

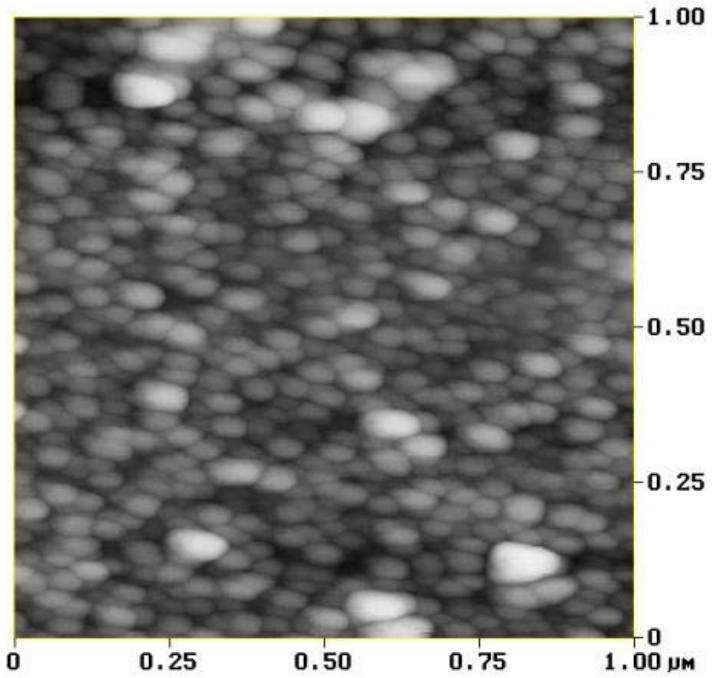

Figure 4-13. AFM of MgO A) grown at 100°C with and RMS roughness of 1.334 nm, and B) grown at 300°C with an RMS roughness of 1.998 nm.

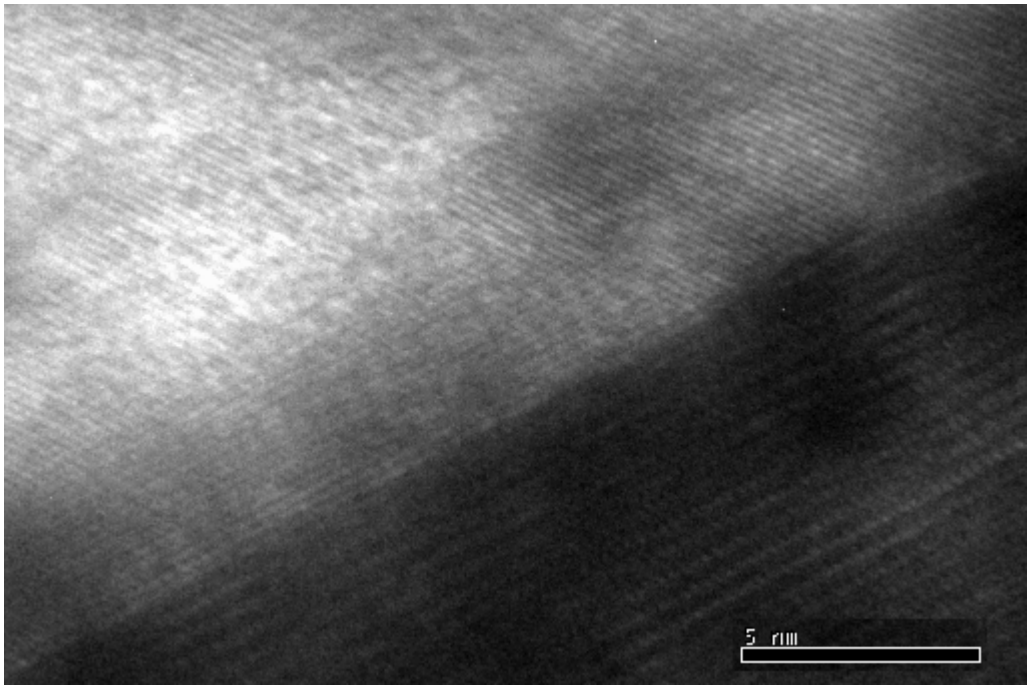

Figure 4-14. HRTEM of MgO grown at 300˚C.

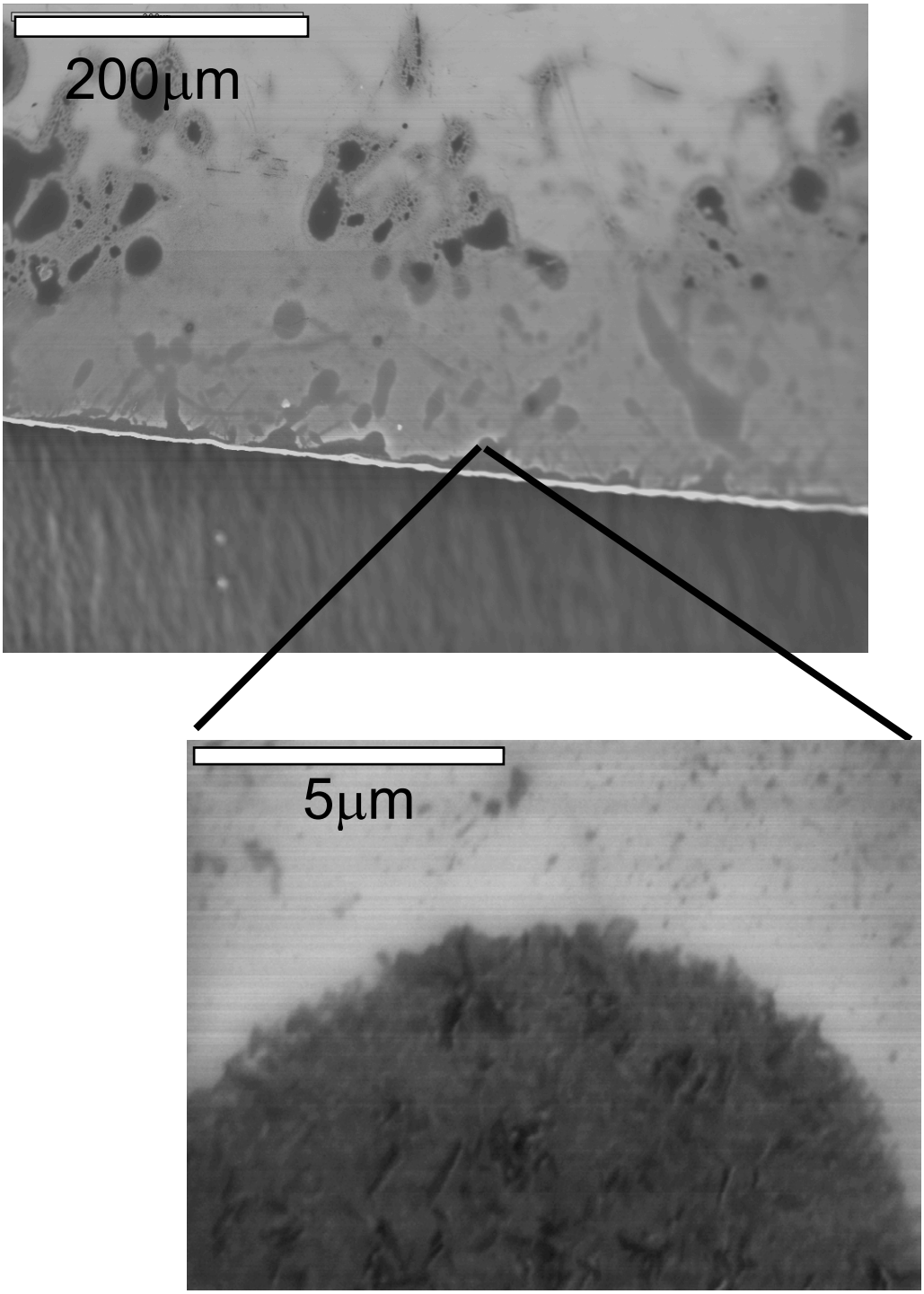

Figure 4-15. SEM of degraded MgO film.

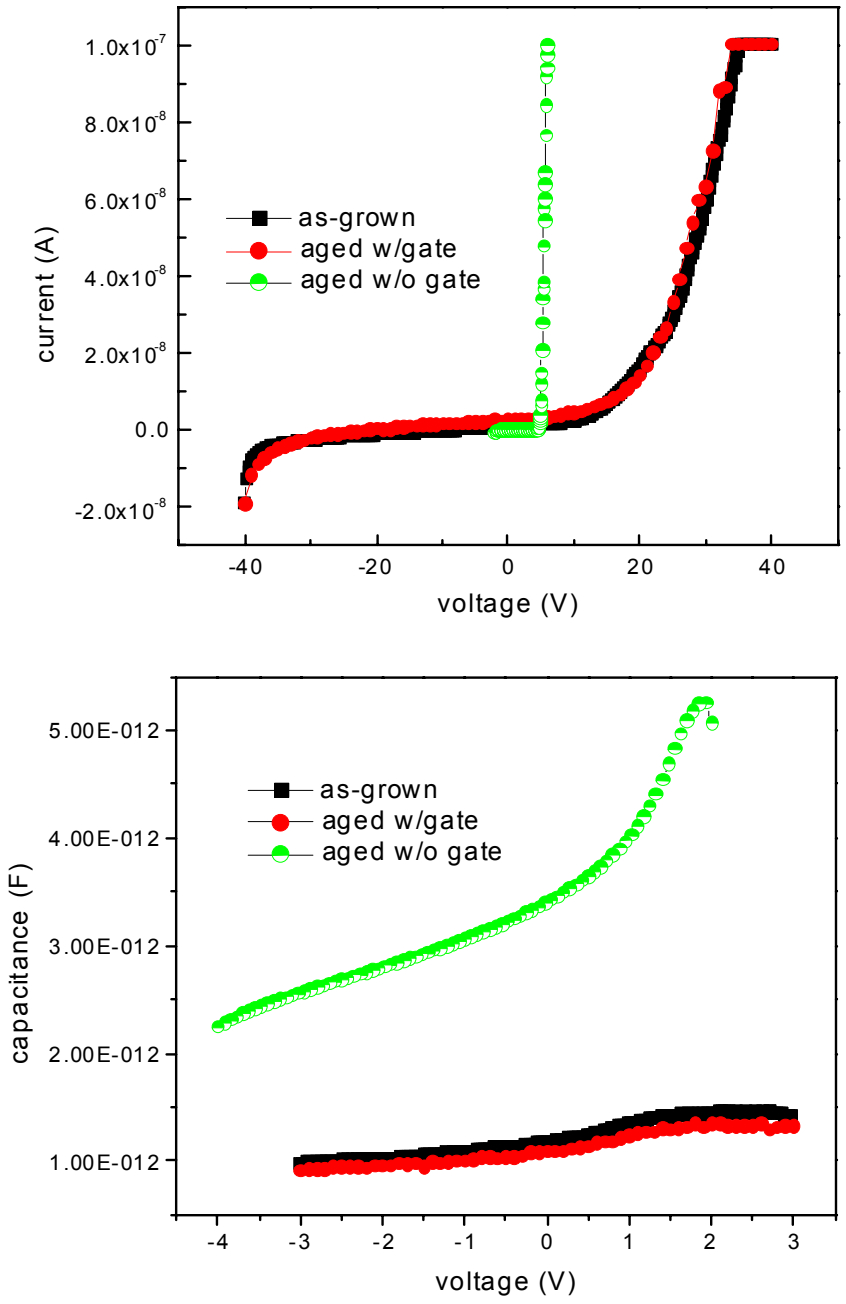

Figure 4-16. I-V and C-V of MgO/n-GaN diodes, aged15 weeks with and without processing

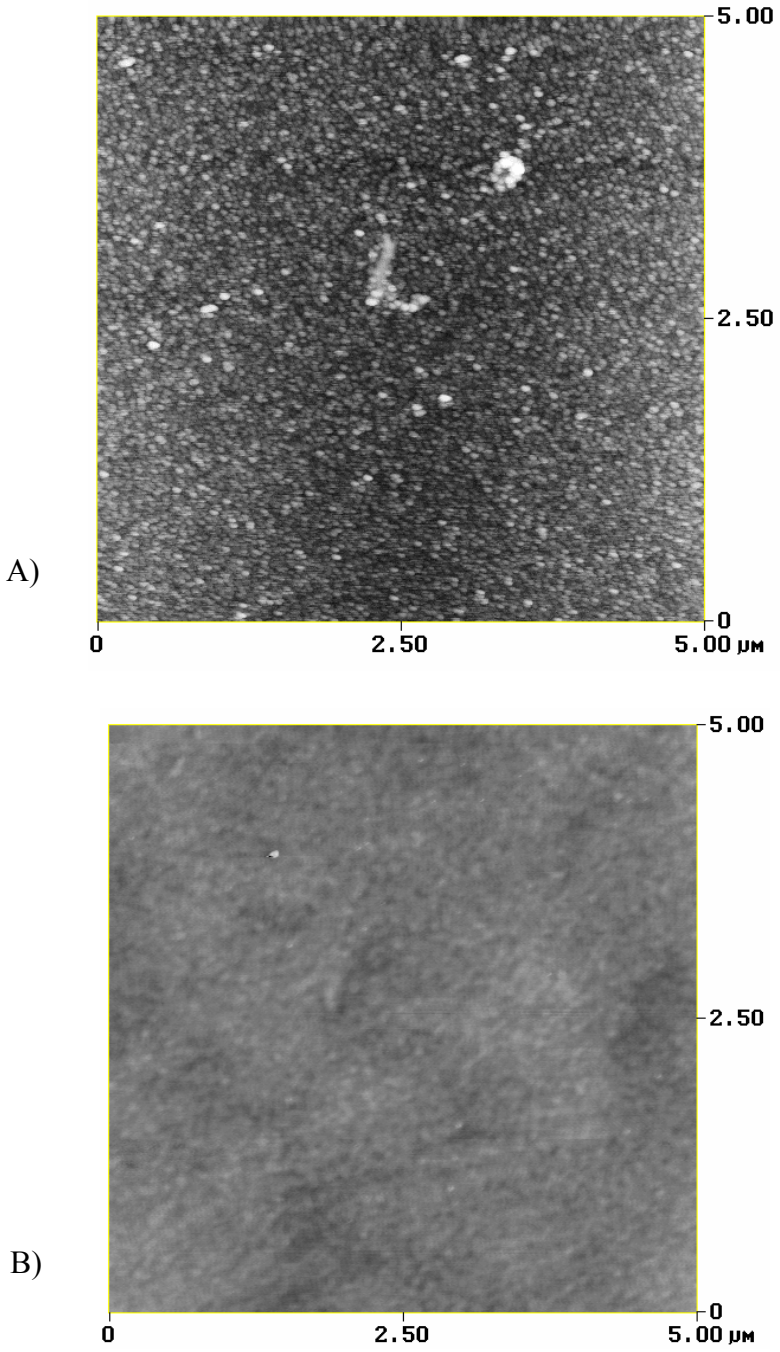

Figure 4-17. AFM of MgO with and without a capping layer. A) MgO without a cap, RMS = 1.921 nm, B) MgO with a 20 nm Sc_2O_3 cap, RMS = 0.337 nm. The MgO is grown at 300˚C. The Sc_2O_3 cap is grown at 100˚C.

CHAPTER 5
MAGNESIUM CALCIUM OXIDE: RESULTS AND DISCUSSION

It is expected that by lattice matching the oxide to the GaN, the interfacial trap density can be reduced. One method of accomplishing this is to alloy the MgO with an oxide of larger lattice constant. Calcium oxide was chosen for this purpose because CaO is also a rock salt dielectric, (Figure 5-1) like MgO, but has a larger lattice constant, 4.779 Å. The CaO dielectric constant (11.8) and bandgap (7.1eV) are similar to those of MgO. From Vegard's Law, the optimum ratio of Mg:Ca should be 1:1 in order to get material lattice matched to GaN. Though the phase diagram[78] shows poor miscibility between MgO and CaO, (Figure 5-2) single-phase thin films on GaAs whose compositions span the entire composition range have been reported using LT-MBE as the deposition method.[79]

5.1 Growth of CaO

First, to prove that CaO can be grown by MBE, starting with conditions similar to those used for the growth of MgO, CaO films were grown on GaN. The solid metal Ca source washeld at temperature of 405˚C to achieve a flux of $8x10^{-8}$ Torr. The same fluxwas used for the growth of MgO. The RF oxygen plasma was set at a pressure of $2x10^{-5}$ Torr. The substrate temperature was 100˚C or 300˚C. AES shows that the film was comprised of Ca and O, (Figure 5-3) but XRD showed no evidence of CaO or Ca diffraction peaks. TEM confirmed that the film was poly-crystalline at the interface but amorphous after 2 nm, (Figure 5-4). The amorphous nature of the bulk of the film explains the absence of peaks in XRD. The CaO film is very sensitive to the electron

beam in the TEM making it difficult to obtain good images. The growth rate of CaO at 100˚C was 25.8 A/min, while at 300˚C the growth rate was 2.2 nm/min. This is to be expected since an increase in temperature should decrease the sticking coefficient. AFM shows no change in RMS roughness of CaO grown at 100˚C versus 300˚C but stays constant at about 0.667 nm, Figure 5-5 and Figure 5-6. Unfortunately, CaO etches in deionized water, which makes processing difficult so no devices were made with CaO.

5.2 Growth of Ternary MgCaO

The standard MgO growth conditions that have produced oxide/GaN interfaces with low D_{it} consist of a Mg beam equivalent pressure, BEP, of $10x10^{-8}$ Torr. The addition of Ca to this beam at a comparable Ca BEP of $8x10^{-8}$ Torr, produced an increase of less than 50% in growth rate. This suggests that the sticking coefficient of the Ca is significantly lower than that of the Mg. This is further confirmed by AES analysis, which shows an Mg/Ca ratio less than that expected for a 50/50 composition film, (Table 5-1). In addition, AES depth profiling analysis shows that the Ca has severely segregated to the surface, (Figure 5-7). This would also indicate a low Ca sticking coefficient.

In spite of the apparent segregation of the Ca, XRD analysis of the MgCaO layer shows no evidence of phase separation, (Figure 5-8). MgO layers grown under similar conditions typically show primarily a (222) peak due to the texturing of the film. The MgCaO layer shows no evidence of either the MgO or the CaO (222) peaks suggesting that phase separation into the two binaries has not occurred. Instead there appears to be a shoulder on the GaN (004) peak that is not observed in spectra taken from either GaN substrates or MgO layers grown on GaN. This peak is most likely the (222) peak from the ternary MgCaO. The peak position is shifted to larger plane spacing relative to the MgO peak as would be expected from the addition of Ca, (Figure 5-9). The proximity of

this peak to the GaN (004) peak is encouraging and suggests that the addition of Ca may be useful in reducing the lattice mismatch between the dielectric and the GaN. Unfortunately due to the severe segregation, the peak is broadened indicative of a range of compositions present in the film, (Figure 5-10).

AFM analysis of the ternary grown at the highest flux rates shows a very rough surface morphology, (Figure 5-11). MgO layers grown under similar conditions show smooth morphology with an RMS of ~1 nm, suggesting that the Ca addition has dramatically altered the microstructure. It was thought that the higher growth rate used for the deposition of the ternary might have caused the rough morphology. To investigate a lower growth rate, the fluxes were reduced to BEP ~ 5.7×10^{-8} Torr. This did produce a substantial drop in the growth rate to ~1 nm/min and was successful in improving the surface morphology. Reducing the growth rate did not, however, suppress the Ca segregation. In fact there appears to be even greater disparity in the Ca surface and interface concentrations. This is not surprising since lower growth rates are usually found to enhance segregation.

Substrate temperature also affects the growth of MgCaO. At a substrate temperature of 340˚C, no film was grown even after 20 minutes of growth time as shown by AES, (Figure 5-12). A slightly lower substrate temperature of 300˚C did result in deposition of a film as determined by AES, (Figure 5-13). This film has a reasonable growth rate of 51.6 A/min, and enhanced crystallinity as shown by XRD, (Figure 5-14). Though for this substrate temperature, AFM does show a slightly rougher surface than that produced with a substrate temperature of 100˚C, (Figure 5-15). Due to

improvements in film quality with the increased substrate temperature of 300˚C, all further growths were done at a substrate temperature of 300˚C.

In order to reduce the segregation, a digital growth technique was used. This showed superior compositional and structural properties as compared to the continuous growth. To study the effects of growth technique on the characteristics of MgCaO deposited on GaN, several films were grown under different conditions. Initially conditions were set so that the Mg and Ca fluxes were equal. The timing sequence was 10 seconds Mg followed by 10 seconds Ca (10/10) with continuous operation of the oxygen plasma. The intended thickness of each layers was 3 Å and the substrate temperature was 300°C. The resulting films were Mg-rich, which showed that Ca has a lower sticking coefficient than Mg. Subsequent samples were grown using a progressively higher Ca flux in order to incorporate more Ca into the film and reduce the lattice mismatch. Digital samples were grown at the same fluxes and oxygen pressures as the continuous samples. AFM shows that the digital samples have a slightly smoother surface than the continuous samples. Also the growth rate of the continuous samples is about twice that of the digital samples, which was expected. Because of a combination of the growth rate and the growth sequence, the digital samples all showed a much more uniform depth profile in AES especially near the surface, (Figure 5-16). In the continuous samples there is a dip in the oxygen concentration near the surface as well as in the Ca profile. The ratio of oxygen to total metal shows a greater incorporation of oxygen in the digital samples than the continuous samples, (Table 5-2).

Powder XRD shows no oxide peaks other than those expected for the MgCaO. The oxide (222) peak is found to shift toward the GaN peak as the amount of Ca incorporated

into the film is increased for both the digital and the continuous growth sequences, (Figure 5-9). This peak position is the same for either growth method grown under the same fluxes, (Figure 5-17). At the highest Ca concentration, the lattice mismatch has been reduced from –6.5% for MgO to –2.05% for the ternary, (Table 5-3). High-resolution XRD shows a full-width-at-half-maximum (FWHM) of 3542 arcseconds, (Figure 5-17). Though this is substantially higher than the GaN FWHM of 507 arcseconds, it is a significant improvement over the value of 4327 arcseconds measured for MgO grown on GaN using similar growth conditions.

Similar to the XRD data, XTEM shows improved crystal quality in the ternary as compared to the binary, (Figure 5-18). In both cases, the oxide /GaN interface is epitaxial. For the binary, continued growth produces a change in microstructure indicative of a nanocrystalline film. For the ternary, this transition is not observed and the overall defect density appears to be significantly lower. This improvement in structural quality is most likely due to the reduction in mismatch for the ternary relative to the binary MgO.

In order to increase the amount of Ca incorporated into the films and reduce the lattice mismatch further, the fluxes of the Mg and Ca were held constant and the length of time the shutters were open was varied. The standard procedure was 10 seconds of Mg followed by 10 seconds of Ca(10/10) with continuous operation of the oxygen plasma. This shutter sequence was continued for the entire growth time. Keeping the cycle time constant at 20 seconds, shutter times of 8 seconds Mg followed by 12 seconds Ca (8/12), and 5 seconds Mg followed by 15 seconds of Ca (5/15) were tried. All samples began with an Mg layer as the first layer.

HRXRD shows the10/10 sample to have the expected peak position to the right of the GaN (004) peak at 73.9 degrees. This corresponds to a composition of 60% Mg and –1.5 lattice mismatch. For the 8/12 shutter sequence more Ca is incorporated and the film is slightly Ca rich. The Mg content goes down to 40.5% Mg and the mismatch is now +0.96%. The 8/12 sample peak shows up as a shoulder on the GaN (004) peak. The 5/15 shutter sequence incorporates even more Ca and has a peak position of 70.175 degrees. This results in a Mg content of 24% and a lattice mismatch of +3.04%. Figure 5-19 shows the XRD plots of these 3 samples.

AFM shows a slight difference in surface roughness for the different shutter sequences, (Figure 5-20). For 10/10 RMS is 0.790 nm, for 8/12 RMS is 1.081 nm, for 5/15 RMS is 0.979 nm. All of these samples have a 20 nm Sc_2O_3 cap. HRTEM shows the oxide to be crystalline and the capping layer to be polycrystalline for the 10/10 shutter sequence.

Table 5-1. Growth rate and AES data for MgCaO samples. AES data taken from an MgO single crystal is shown for comparison.

Mg Beam Equivalent Pressure (Torr)	Ca Beam Equivalent Pressure (Torr)	Growth Rate (nm/min)	Mg/Ca Ratio	(Mg+Ca)/O Ratio
5.7×10^{-8}	5.7×10^{-8}	1.0	0.81	0.92
10×10^{-8}	8×10^{-8}	5.3	1.27	0.83
10×10^{-8}	-	3.4	0.72	0.72
MgO Ref.	-	-	-	0.6

Table 5-2. Growth rate, AFM and AES data for MgCaO grown at 300˚C.

Growth Method	Mg Beam Equivalent Pressure (Torr)	Ca Beam Equivalent Pressure (Torr)	Growth Rate (nm/min)	RMS roughness (nm)	O/(Mg+Ca) from AES
Continuous	10x10-8	9.0x10-8	5.6	1.931	0.52
Digital	9.6x10-8	8.6x10-8	3	0.712	1.40
Continuous	8.0x10-8	9.0x10-8	5.3	0.774	1.29
Digital	8.0x10-8	9.0x10-8	1.8	0.554	1.81
MgO ref.	12x10-8	---	2.4	1.998	0.50

Table 5-3. Composition and mismatch from XRD

layer C- continuous D- digital	2-theta	% Mg	% mismatch to GaN
MgO	78.59	100	-6.45
MgCaO-C	75.43	72.8	-3.11
MgCaO-D	75.41	72.8	-3.09
MgCaO-C	74.79	74.79	-2.40
MgCaO-D	74.47	74.47	-2.05
50/50	~72.9	50	-0.23
CaO	67.375	0	6.86

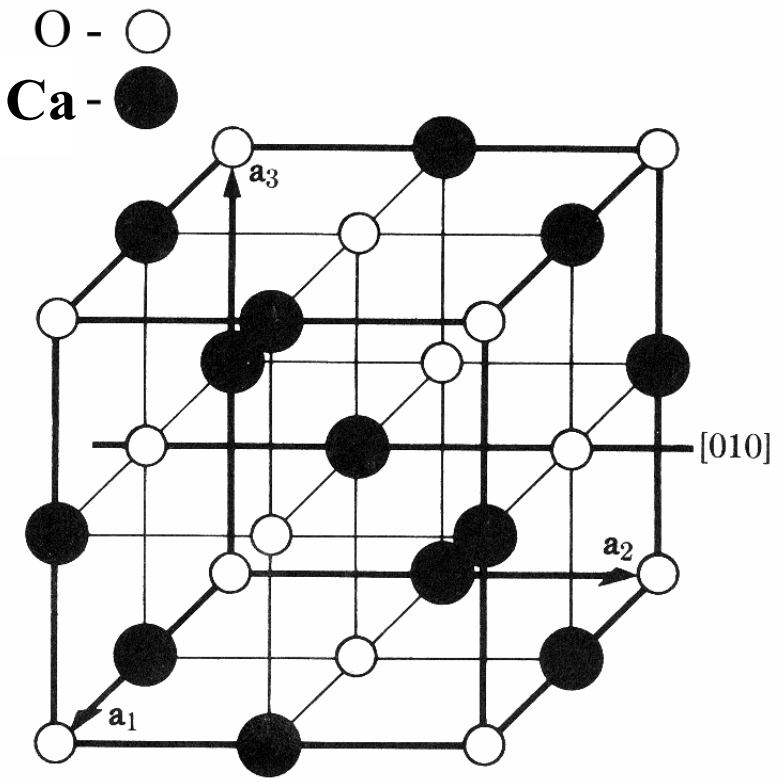

Figure 5-1. Illustration of the CaO structure (from Cullity 1978)

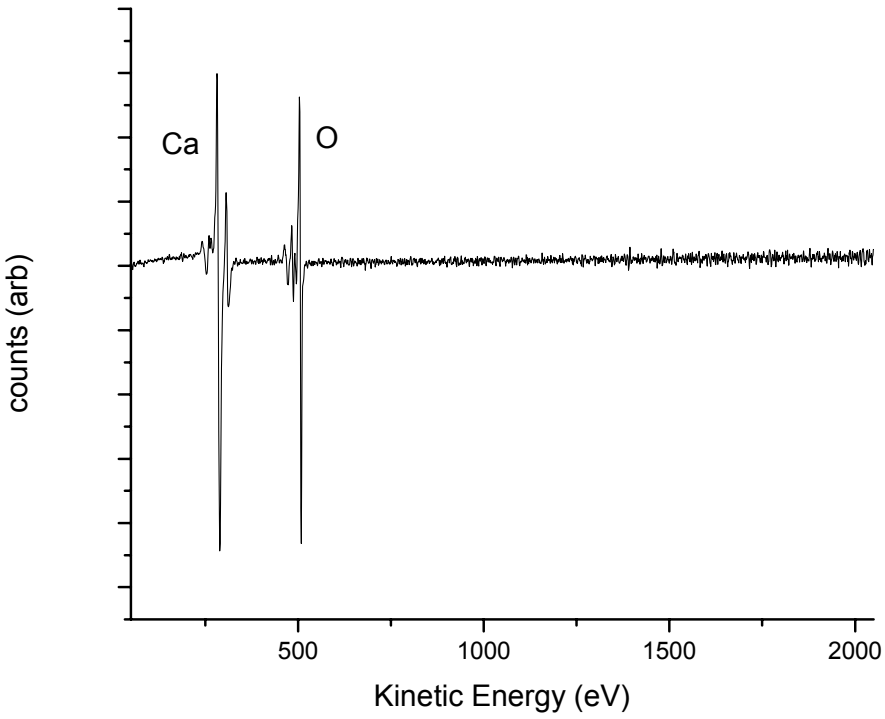

Figure 5-2. AES shows only Ca and O after growth of CaO at 300˚C

CaO–MgO

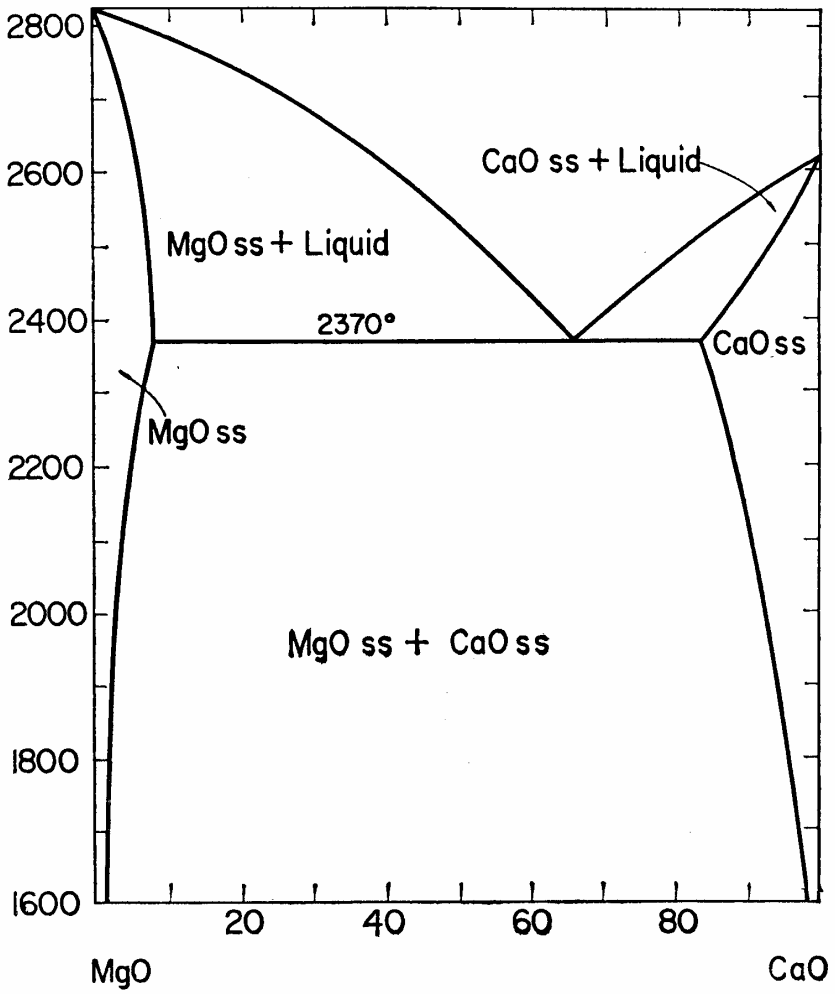

FIG. 229.—System CaO–MgO.

R. C. Doman, J. B. Barr, R. N. McNally, and A. M. Alper, *J. Am. Ceram. Soc.*, **46** [7] 314 (1963).

Figure 5-3. MgO-CaO phase diagram.[78]

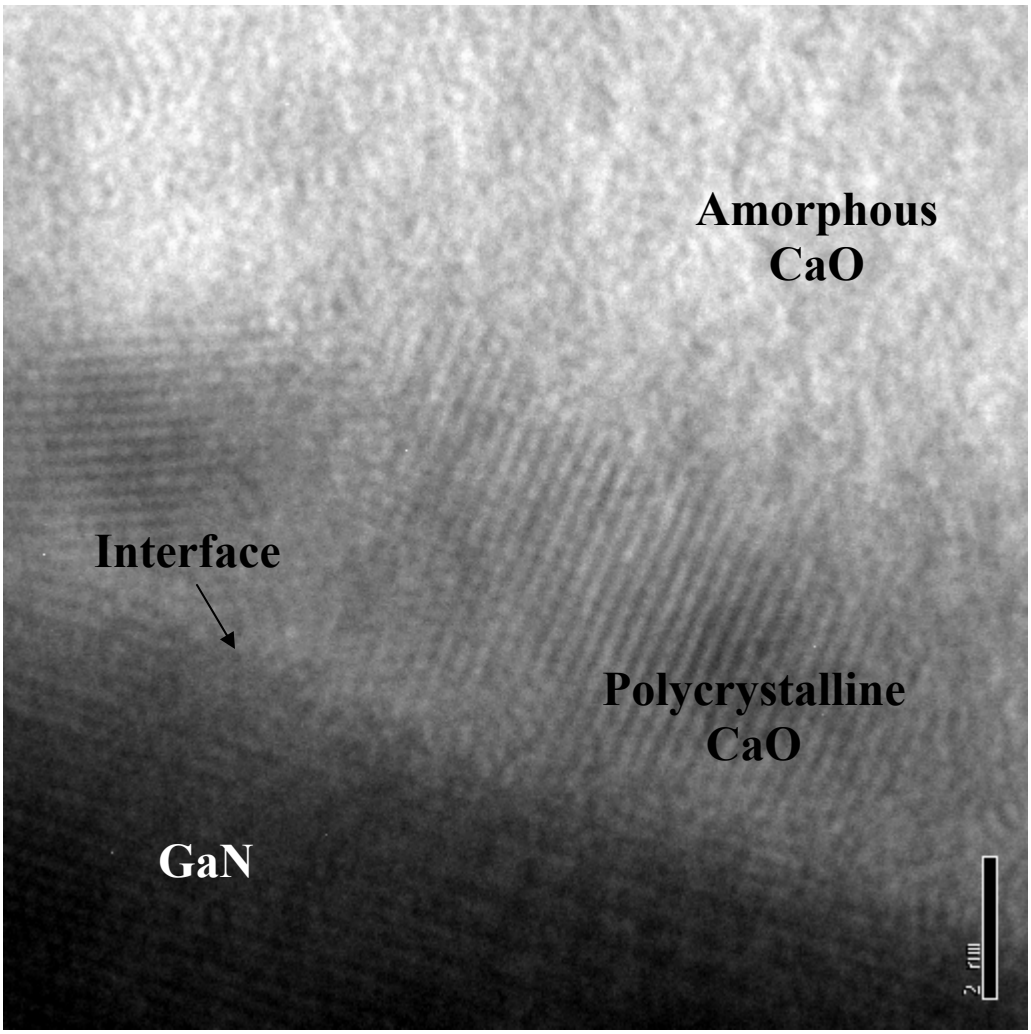

Figure 5-4. HR TEM of CaO.

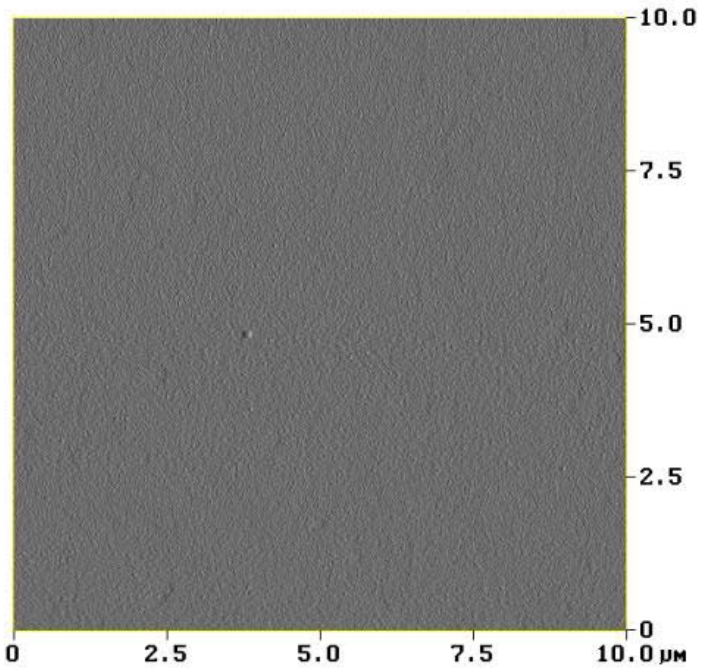

Figure 5-5. AFM of CaO grown at 100˚C, RMS = 0.667 nm.

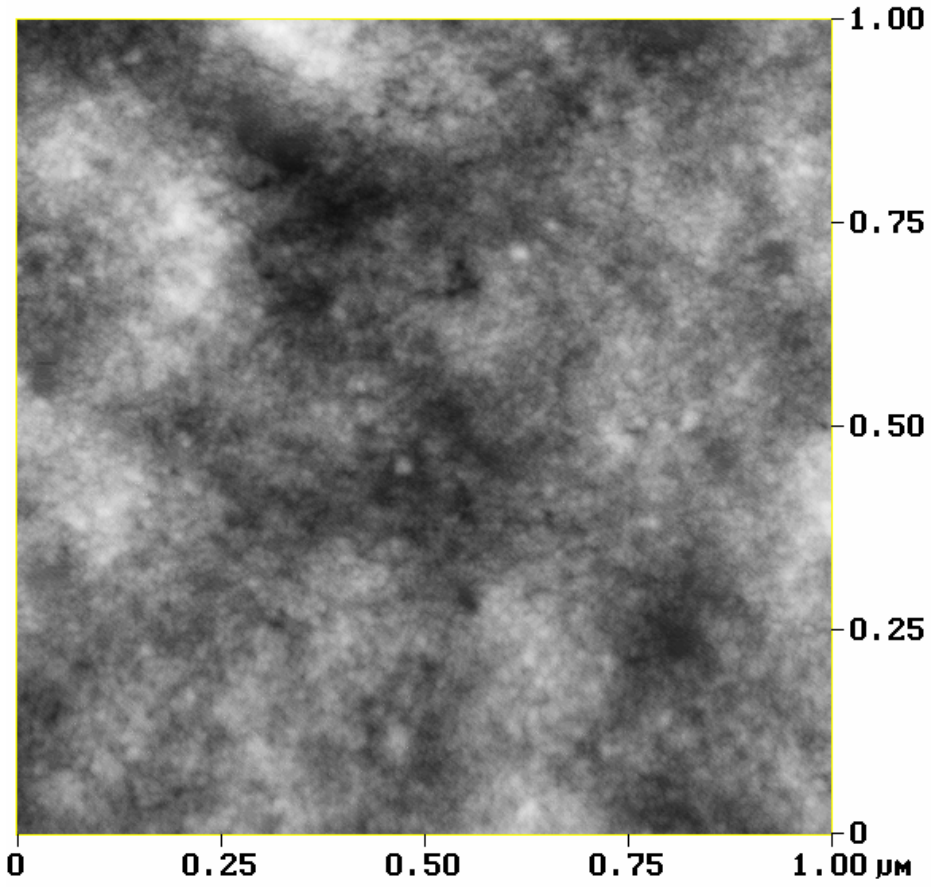

Figure 5-6. AFM of CaO grown at 300˚C, RMS roughness is 0.667 nm.

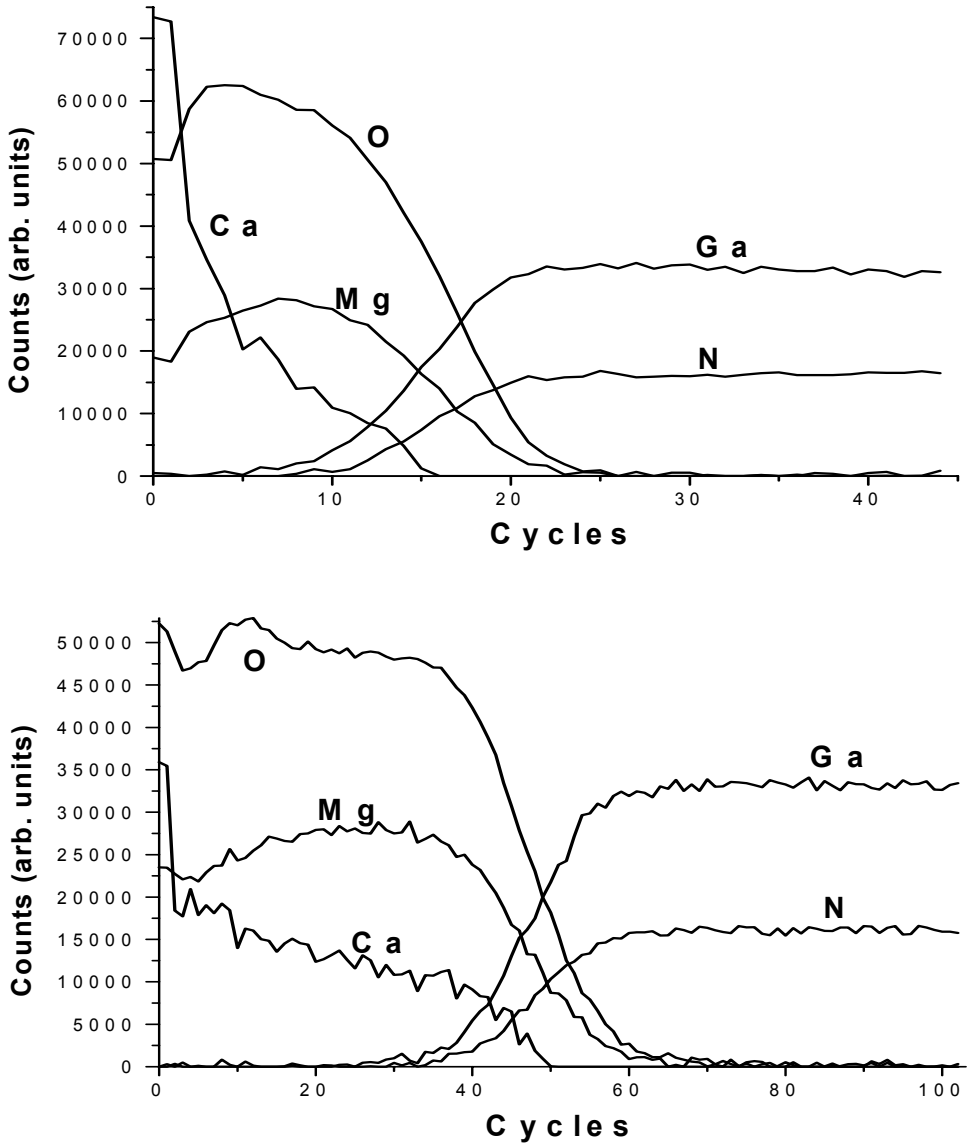

Figure 5-7. AES depth profiling of MgCaO grown using Ca and Mg BEP of 5.7×10^{-8} and 5.7×10^{-8} (top) and 8×10^{-8} and 10×10^{-8} (bottom).

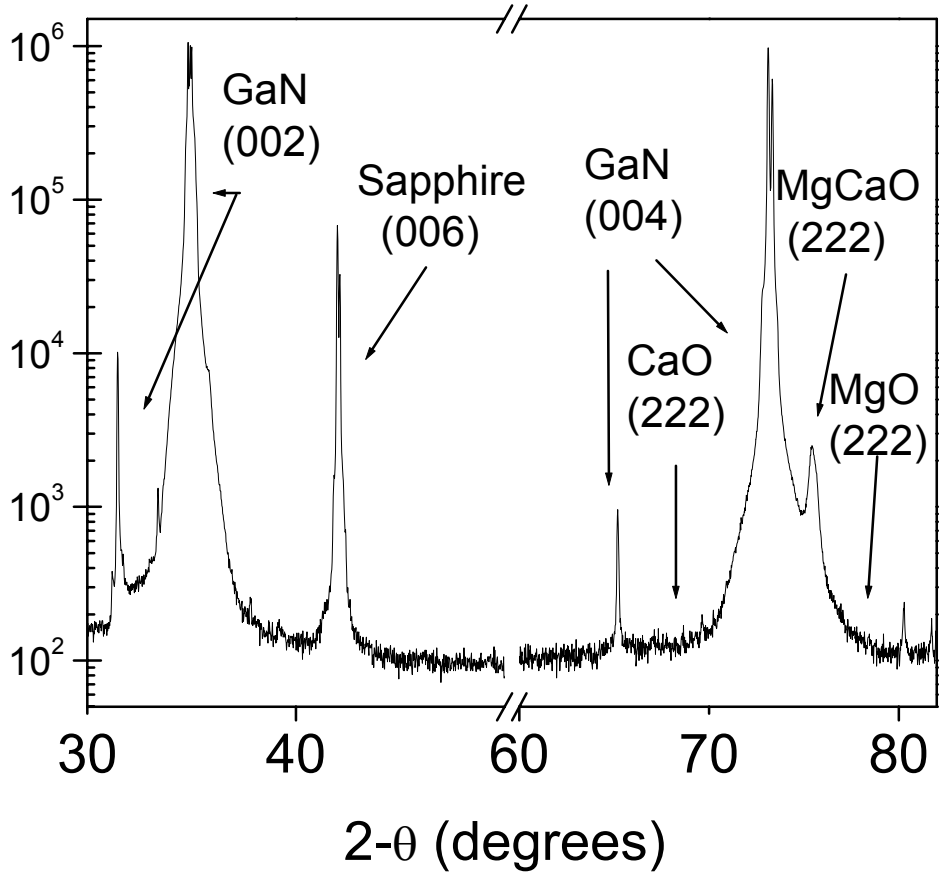

Figure 5-8. XRD of MgCaO shows no signs of phase separation or secondary phases.

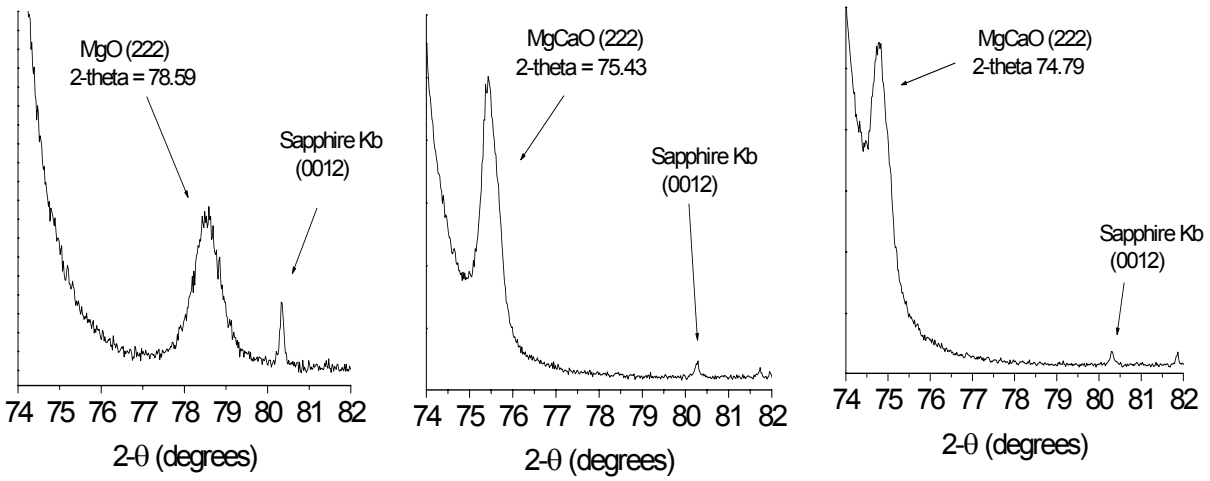

Figure 5-9. Powder XRD showing increase in lattice constant with the addition of Ca.

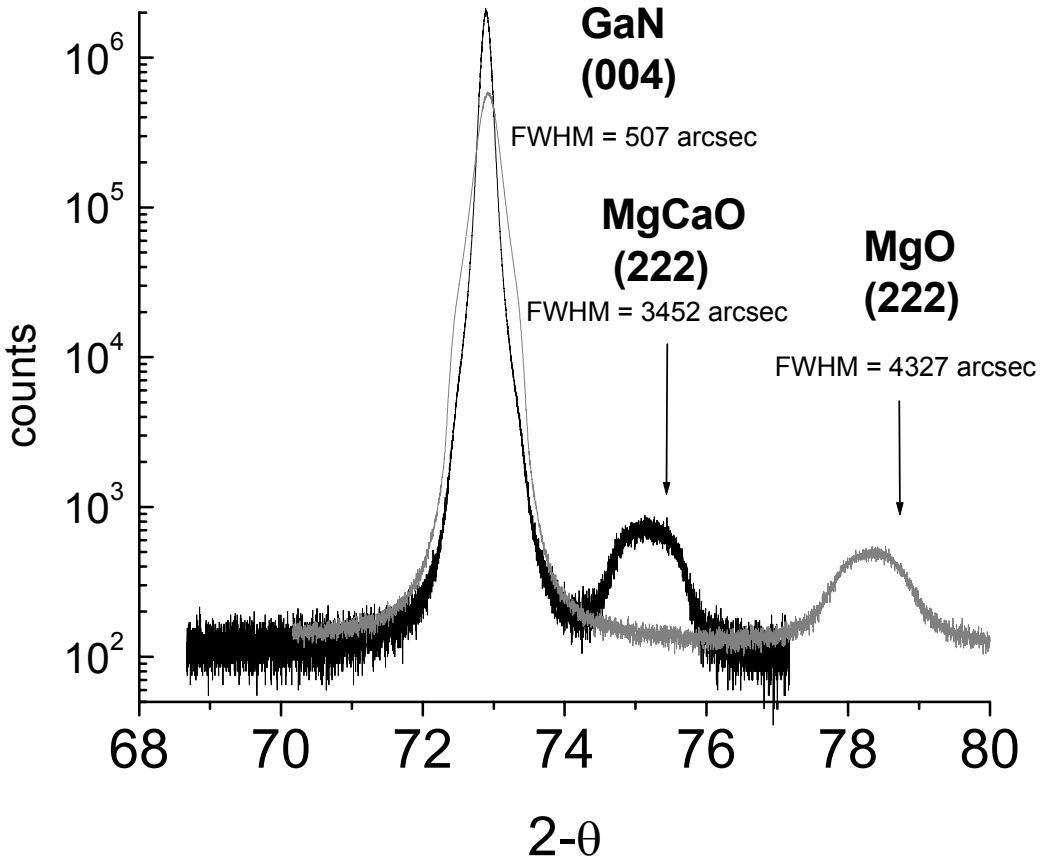

Figure 5-10. HR-XRD shows the relative positions of the MgO (222) and the MgCaO (222) peaks.

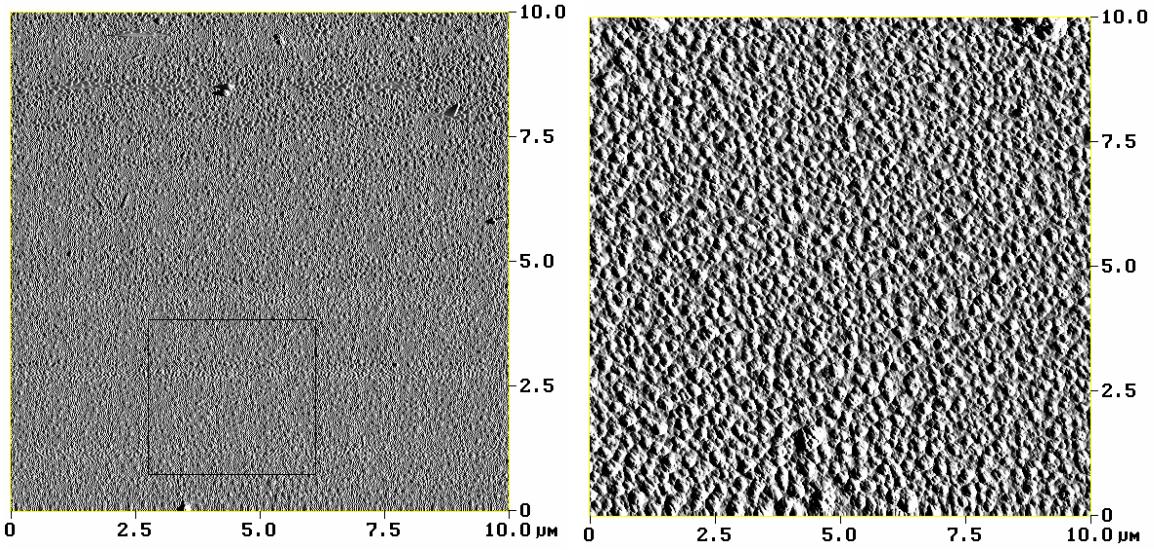

A) B)

Figure 5-11. AFM of MgCaO grown at 100ºC using Mg and Ca fluxes of A) 5.7×10^{-8} or B) 8×10^{-8}. RMS roughnesses for the two samples were 4 nm and 9 nm respectively. MgO grown under similar conditions shows an RMS roughness of ~1 nm

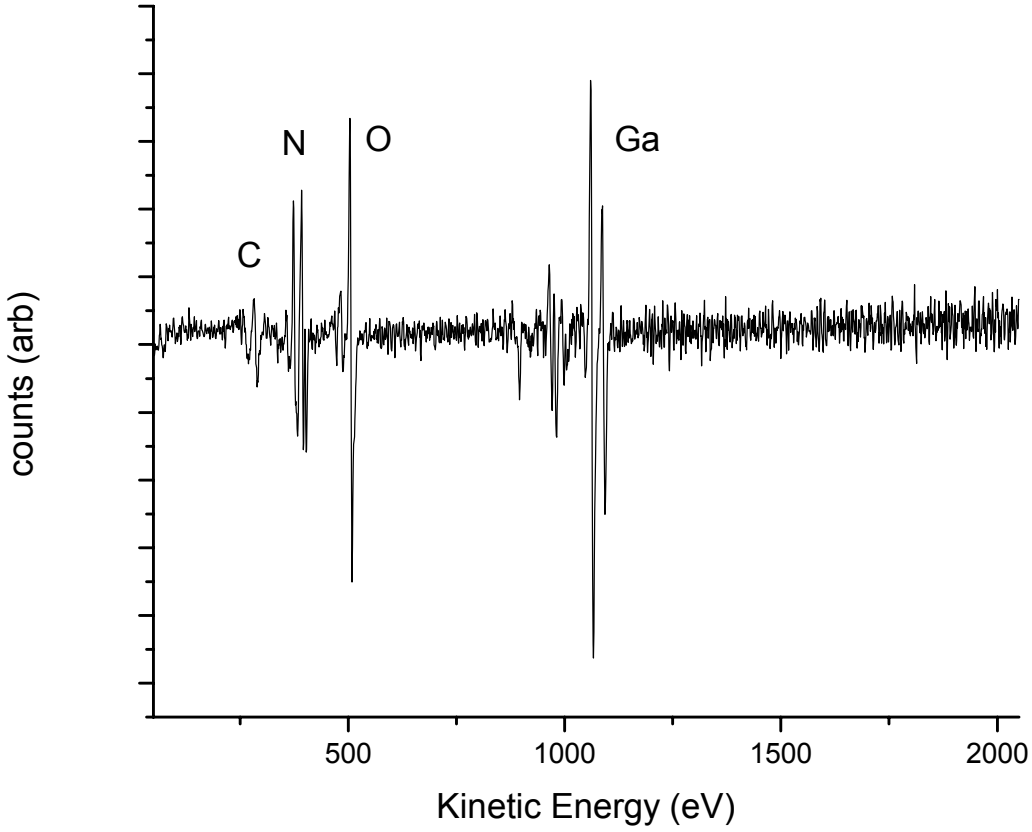

Figure 5-12. AES shows that no Mg (1175 eV) or Ca (294 eV) is present after growth time. Oxygen is due to exposure of surface to oxygen plasma for duration of growth time.

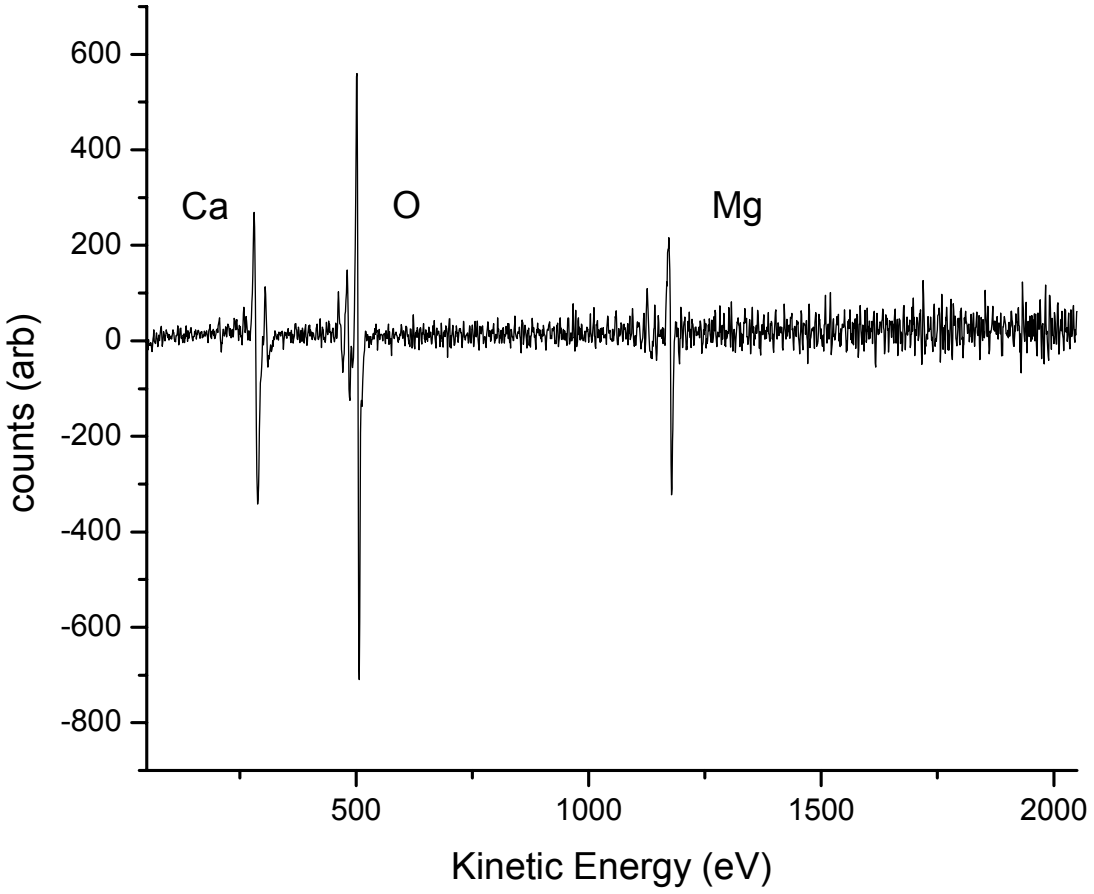

Figure 5-13. AES of MgCaO film grown at substrate temperature of 300˚C.

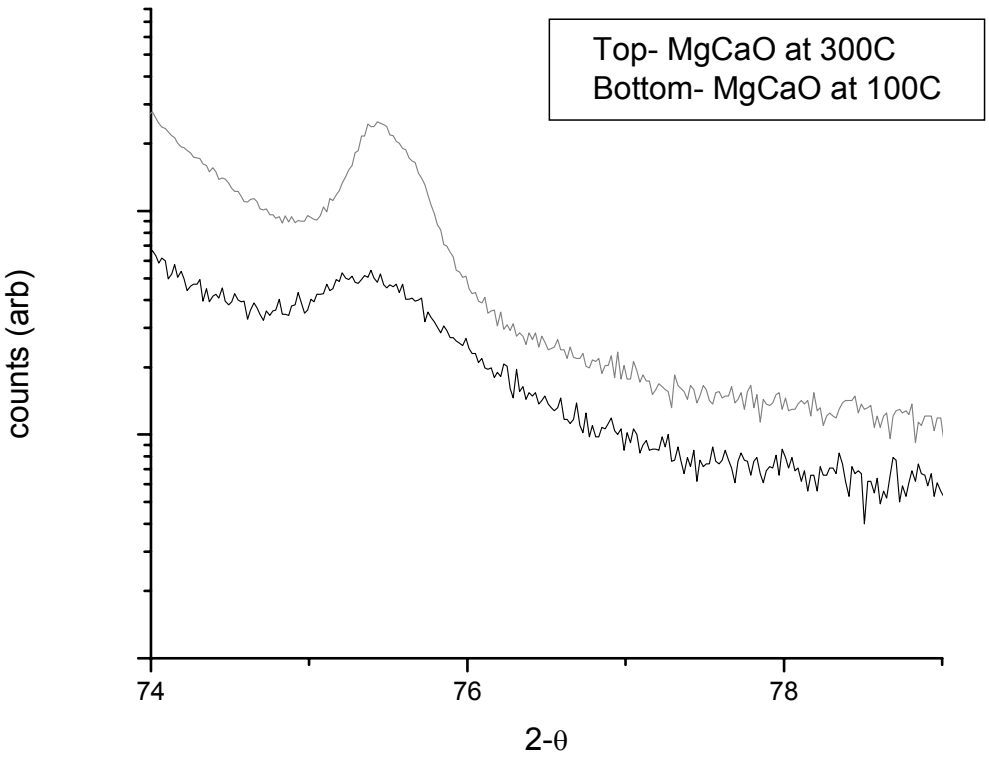

Figure 5-14. XRD shows that the peak from the MgCaO film grow at 300˚C is much sharper than the MgCaO film grown at 100˚C.

A)

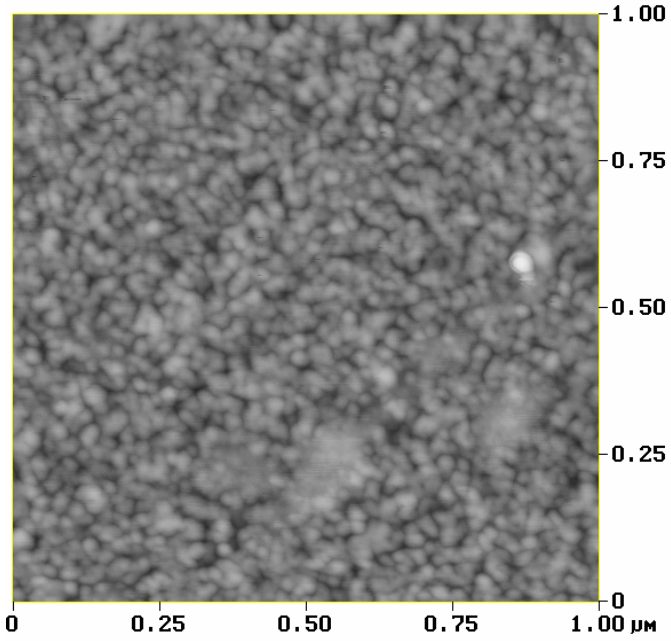

B)

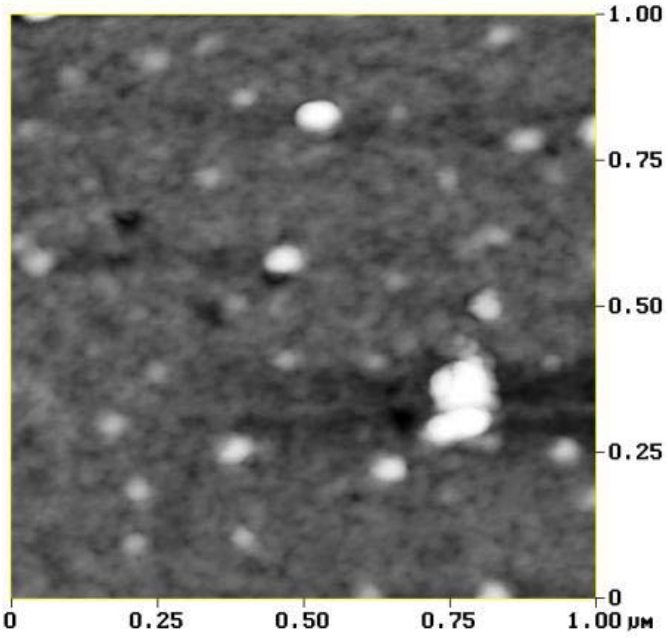

Figure 5-15. AFM of MgCaO grown at A)100˚C, RMS = 1.256 nm, B) 300˚C, RMS = 1.931 nm.

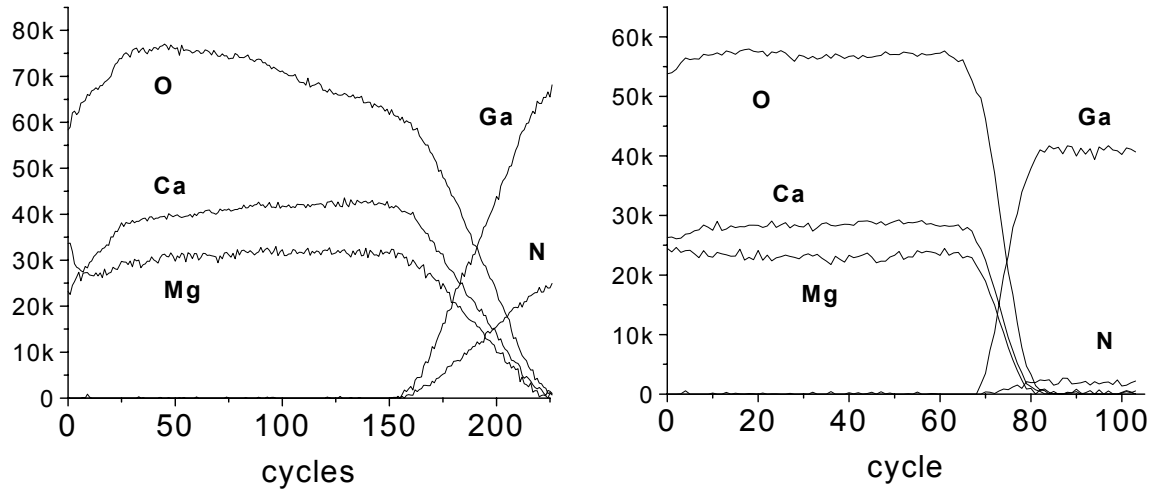

Figure 5-16. AES scans of continuously grown sample (at left), and digitally grown sample (at right). Both films were deposited at 300ºC under the same conditions.

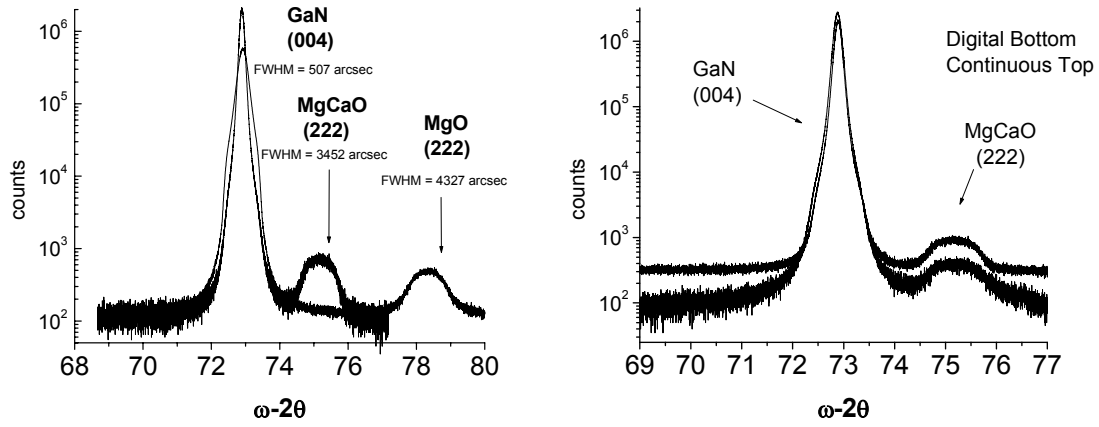

Figure 5-17. HR-XRD showing MgCaO and MgO texturing in the (111) direction. Peak positions were the same for the digital and continuous growth techniques under the same growth conditions. The ternary oxide showed a significantly lower FWHM than the binary MgO

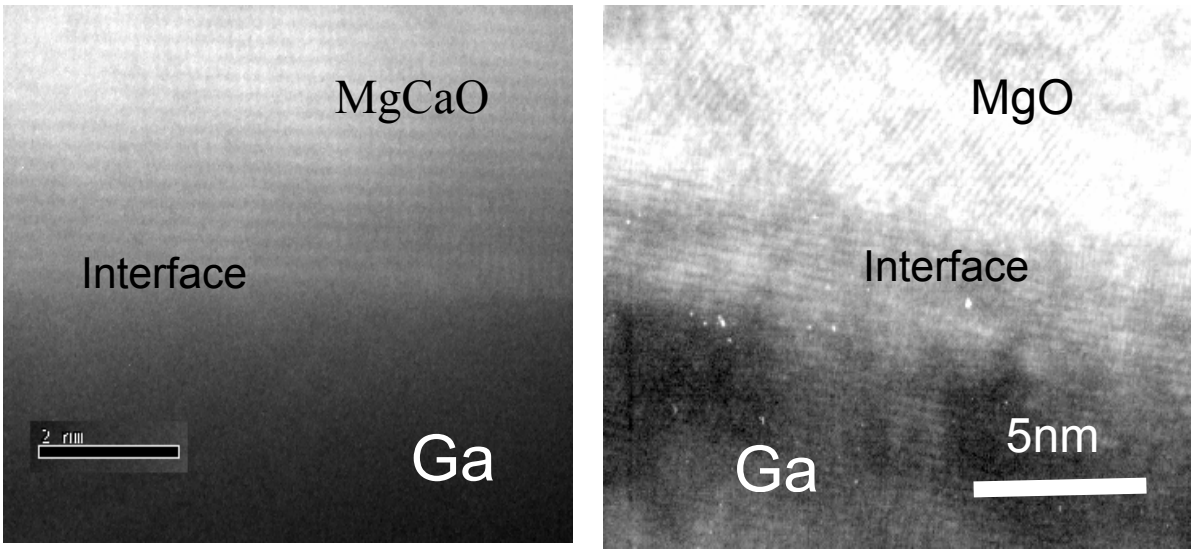

Figure 5-18. High resolution XTEM showing the epitaxial nature of the initial oxide layers grown on GaN. The ternary layer, shown at left, shows no evidence of crystallite formation while the MgO layer, shown at right, shows clear evidence of rotational relaxation.

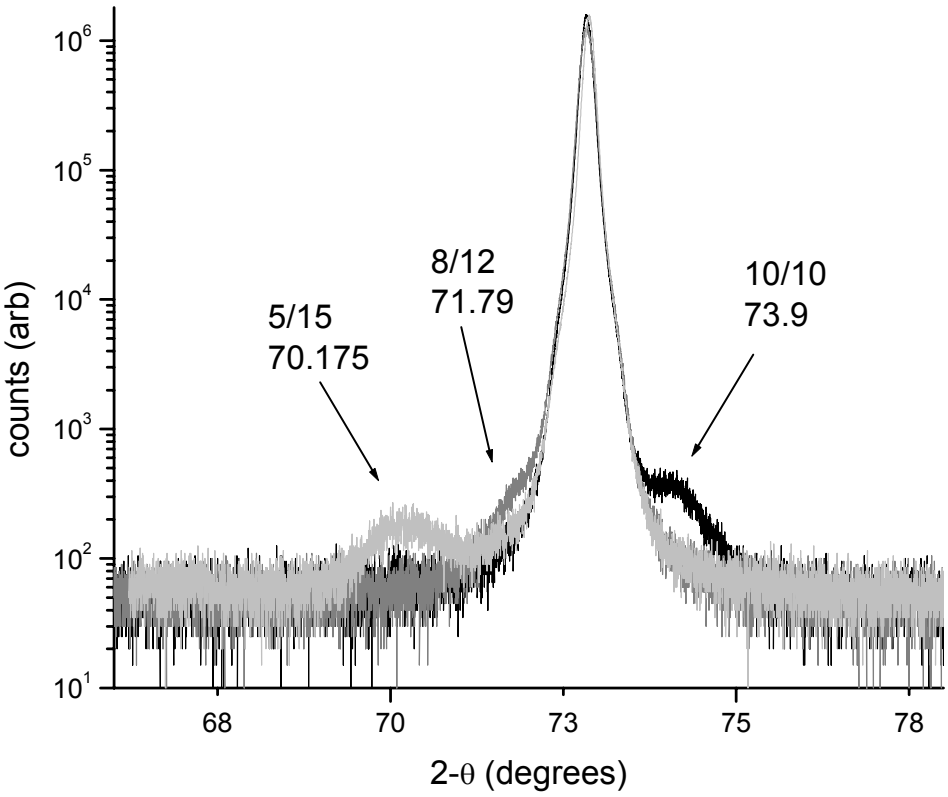

Figure 5-19. HR XRD showing change in peak position with change in shutter timing.

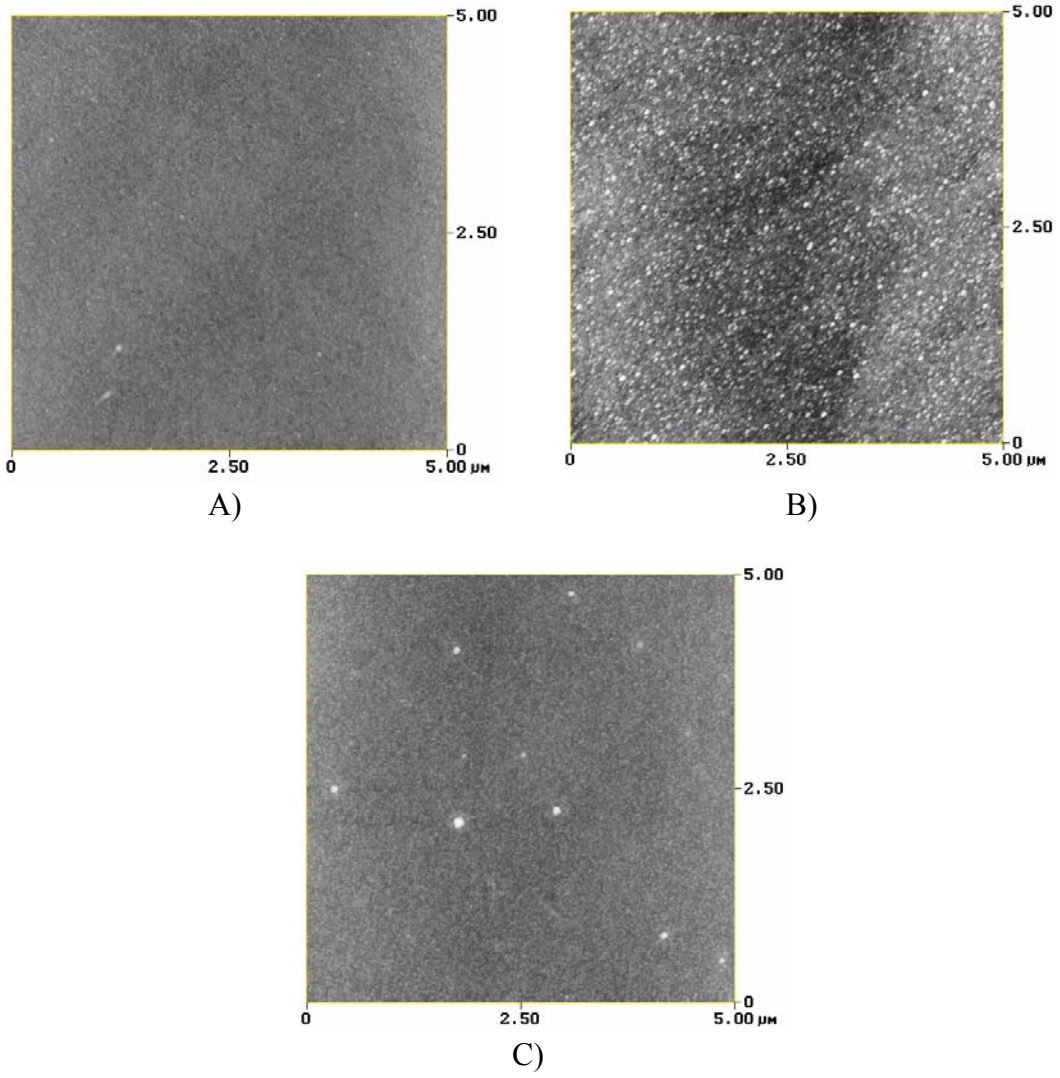

Figure 5-20. AFM of capped MgCaO at different shutter sequences. A) 10/10 with RMS roughness of 0.970 nm, B) 8/12 with RMS roughness of 1.081 nm, andC) 5/15 with RMS roughness of 0.979 nm.

CHAPTER 6
SCANDIUM MAGNESIUM OXIDE AND MAGNESIUM SCANDIUM OXIDE: RESULTS AND DISCUSSION

Scandium oxide, Sc_2O_3, has been explored for use as a dielectric for GaN and has many favorable properties. GaN gated diodes using Sc_2O_3 have shown inversion but the D_{it} of Sc_2O_3 is still higher than that seen for GaN diodes using MgO. Unlike MgO, Sc_2O_3 has the bixbyite structure. The bixbyite structure is a face-centered cubic, FCC, array of Sc atoms with 3/4 of tetrahedral sites filled with oxygen atoms, (Figure 6-1). The bond length mismatch between the GaN(0001) and the Sc_2O_3(111) is 9%. Scandium oxide is very environmentally stable. Even though Sc_2O_3 has a much different crystal structure and lattice constant, the ternary MgScO and ScMgO films have much potential.

The addition of Sc to MgO should increase the environmental stability of the film. It should also increase the lattice constant of the material which would improve the D_{it} and hence device performance. Films with a higher percentage of Mg than Sc are referred to as MgScO.

Adding Mg to Sc_2O_3 may also improve the D_{it} of Sc_2O_3 by decreasing the lattice constant. The addition of Mg to Sc_2O_3 should improve confinement on the valence band, which is necessary for CMOS technology, and improve the lattice match. As stated before the reduction in lattice mismatch reduced D_{it}, increases E_{BD} and will enable novel device structures such as GaN single crystal grown over dielectric and 3-D integration. Films with a higher percentage of Sc than Mg are referred to as ScMgO.

6.1 Scandium Magnesium Oxide

To study the effects of growth conditions and composition on the characteristics of ScMgO deposited on GaN, several films were grown under different scandium rich conditions. The composition of the films was varied by using a constant Sc cell temperature and varying the Mg cell temperature from 330°C to 350°C. As the Mg cell temperature was increased, the growth rate increased (Table 6-1) in agreement with previous work with MgO.[80] Although the growth rate increased, the RMS roughness remained about the same for a given substrate temperature. All of the samples grown at a substrate temperature of 100°C had an RMS roughness of about 0.6 nm independent of the Mg cell temperature. XRD showed a secondary phase peak at 76.7 degrees for samples with a Mg cell temperature over 330°C. No secondary phase peak was seen at a cell temperature of 330°C. AES shows an increase in the ratio of Mg to the total amount of metal in the samples with increasing cell temperature and growth rate, which shows that more Mg is being incorporated into the film. AES also shows that the ratio of oxygen incorporated into the film decreased with increasing growth rate. Depth profile AES showed an increasingly large dip in the amount of O at the surface with increasing Mg, (Figure 6-2).

The effect of the substrate temperature, T_{sub}, on the film was investigated by holding the fluxes constant at T_{Sc} = 1190°C and T_{Mg} = 350°C, and increasing the substrate temperature from 100°C to 500°C. As the substrate temperature was increased the growth rate remained unchanged, which has been seen in previous work with scandium oxide growth.[81] But unlike Sc_2O_3, as the substrate temperature increased the surface roughness also increased significantly from 0.6 nm at 100°C to 24.63 nm at

500°C, (Figure 6-3). AES showed a decrease in the amount of Mg incorporated into the film, which is consistent with a reduction of the Mg sticking coefficient with increased temperature. Depth profile AES (Figure 6-2) showed a reduction in surface effects, such as the dip in oxygen near the surface, with increased substrate temperature. XRD showed an increase in the peak height but no change in position. This suggests that little or no Mg is being incorporated at the higher substrate temperatures and thus no improvement in lattice mismatch between the oxide and the underlying GaN is being achieved.

All of the multi-phase films showed a magnesium rich secondary phase peak at 76.7 degrees, which corresponds to a composition of 98%Mg, (Figure 6-4). This peak occurs in the same position regardless of the growth conditions used for deposition, suggesting the solid solubility limit of MgO in Sc_2O_3 has been reached. The scandium oxide peak is masked by the GaN K_β peaks at the same position making an accurate determination of the lattice constant of the single phase ScMgO alloy difficult. If the lattice constant follows Vegard's law then based upon the composition as determined by AES, the lattice mismatch between the ScMgO and the GaN should be reduced from the 9.5% obtained with pure Sc_2O_3 to ~1.5%. Because of the formation of second phases this lattice matching is not possible but a slight reduction in lattice mismatch is achieved below the composition at which second phases appear.

6.2 Magnesium Scandium Oxide

To study the effects of growth conditions and composition on the characteristics of MgScO deposited on GaN, several films were grown under different magnesium rich conditions. The composition of the films was varied by using a constant Mg cell

temperature and varying the Sc cell temperature, T_{Sc}, from 1090°C to 1130°C. As the Sc cell temperature was increased, the growth rate increased only slightly

Initial work was done on Si to see the effect of annealing on the oxide and to determine the composition at various Sc cell temperatures. The Mg/Sc ratio decreased as the T_{Sc} increased, from 8.5 to 3.3. Etch rates also decreased as the Sc cell temperature increased, from 1.32 nm/sec at T_{Sc} = 1090˚C to 0.3 nm/sec at T_{Sc} = 1130˚C due to the increase in the amount of Sc in the film. The scandium cell temperature of 1090˚C produced a film composition most likely to produce single-phase material on GaN.

From this initial work on Si, MgScO was grown on GaN at a Sc cell temperature of 1090˚C. Powder XRD (Figure 6-5) showed a peak position of 78.09 degrees, which is closer to the GaN (004) peak than MgO showing that Sc has changed the lattice constant of the film. AES confirmed the composition of the capping layer and the oxide film (Figure 6-6). The MgScO film grown on GaN at 100˚C was much rougher than that grown on Si, RMS = 26.075 nm, (Figure 6-7). With a protective Sc_2O_3 cap grown at 100˚C, the RMS roughness was decreased to 0.728 nm, (Figure 6-8). For MgScO grown at 300˚C the RMS roughness increased to10.24 nm, (Figure 6.9). The amount of Mg incorporated in the film decreased with increasing substrate temperature. The sticking coefficient of Sc is not as temperature dependant as Mg. The Sc_2O_3 growth rate is relatively independent of growth temperature while almost no MgO film grows over a substrate temperature of 350˚C. HR-TEM (Figure 6-10) of MgScO grown at 100˚C with a Sc_2O_3 cap shows the oxide/GaN interface to be epitaxial and single crystalline. EDS shows this film to be the expected composition, (Figure 6-11). The Sc_2O_3 capping layer is polycrystalline, similar to that grown on GaN.

Table 6-1. Dependence of growth rate, RMS roughness, and AES ratio on magnesium cell temperature and substrate temperature.

T_{Mg} (°C)	T_{sub} (°C)	G rate (Å/min)	RMS (nm)	Mg/(Sc+Mg)	O/(Sc+Mg)
330	100	13.33	0.694	0.49	0.81
340	100	25.00	0.580	0.61	0.74
350	100	35.33	0.645	0.71	0.65
350	300	36.67	2.947	0.68	0.68
350	500	37.67	24.63	0.55	0.96

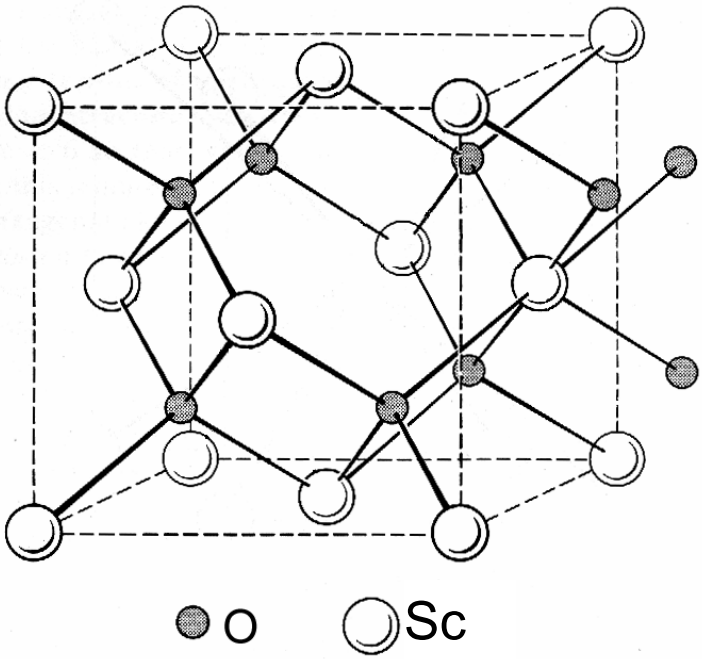

Figure 6-1. The Bixbyite crystal structure of scandium oxide. (B.P Gila 2000)

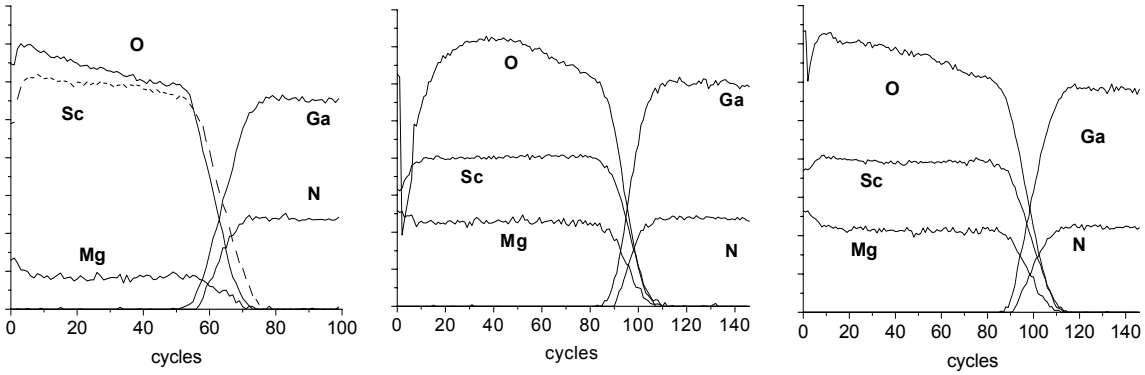

Figure 6-2. AES depth profiles taken from layers grown under different growth conditions: T_{Mg} = 330°C, T_{sub} = 100°C (at left); T_{Mg} = 350°C, T_{sub} = 100°C (middle); and T_{Mg} = 350°C, T_{sub} = 300°C (at right).

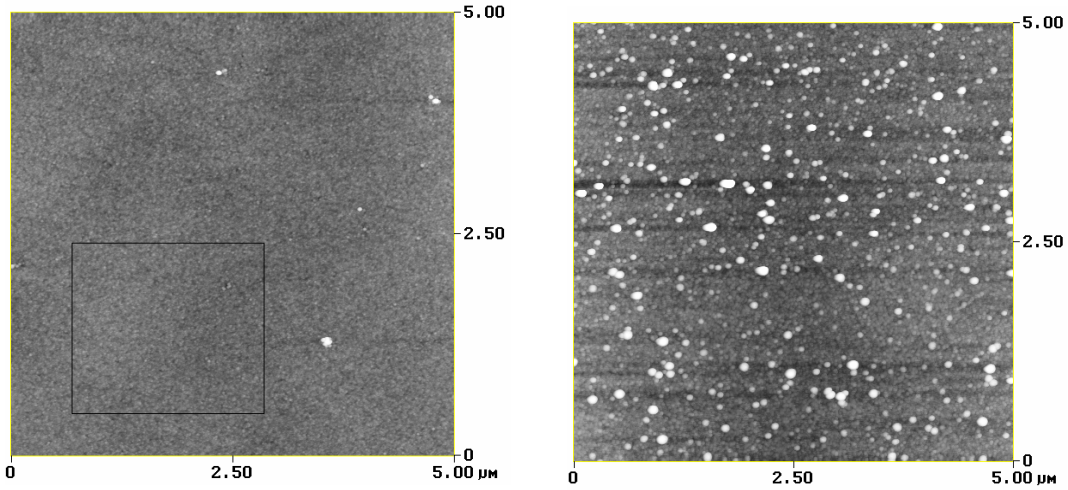

A) B)

Figure 6-3. AFM surface scans for films grown at A) T_{Mg} = 350°C, T_{sub} = 100°C showing an RMS roughness of 0.645 nm and B) T_{Mg} =350°C, T_{sub} = 300°C showing an RMS of 2.947 nm.

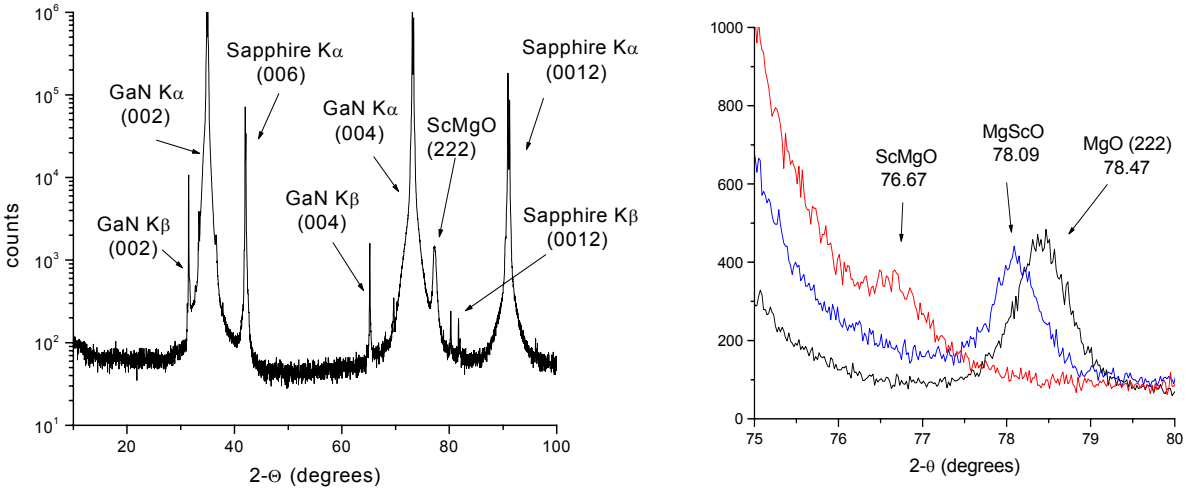

Figure 6-4. XRD of ScMgO grown at T_{Mg} =350°C and T_{sub} = 300°C (at left) and comparison of the secondary peak position of scandium rich ScMgO with magnesium rich MgScO and MgO (at right). All peak positions are normalized with respect to the GaN (004) peak.

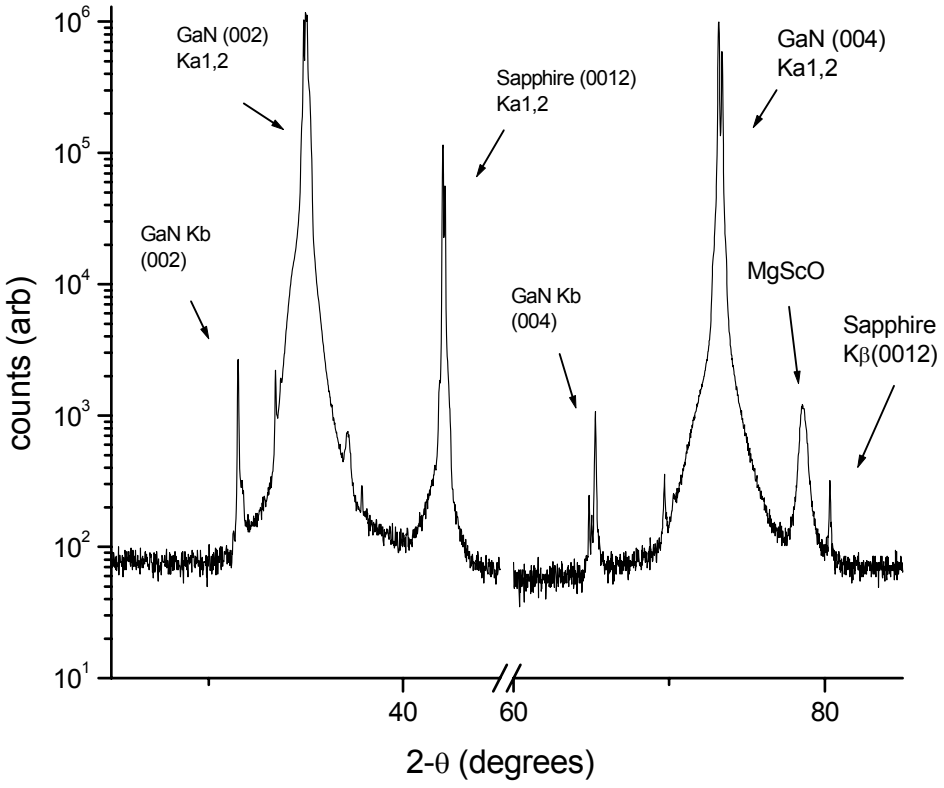

Figure 6-5. Powder XRD showing the peak position of MgScO peak.

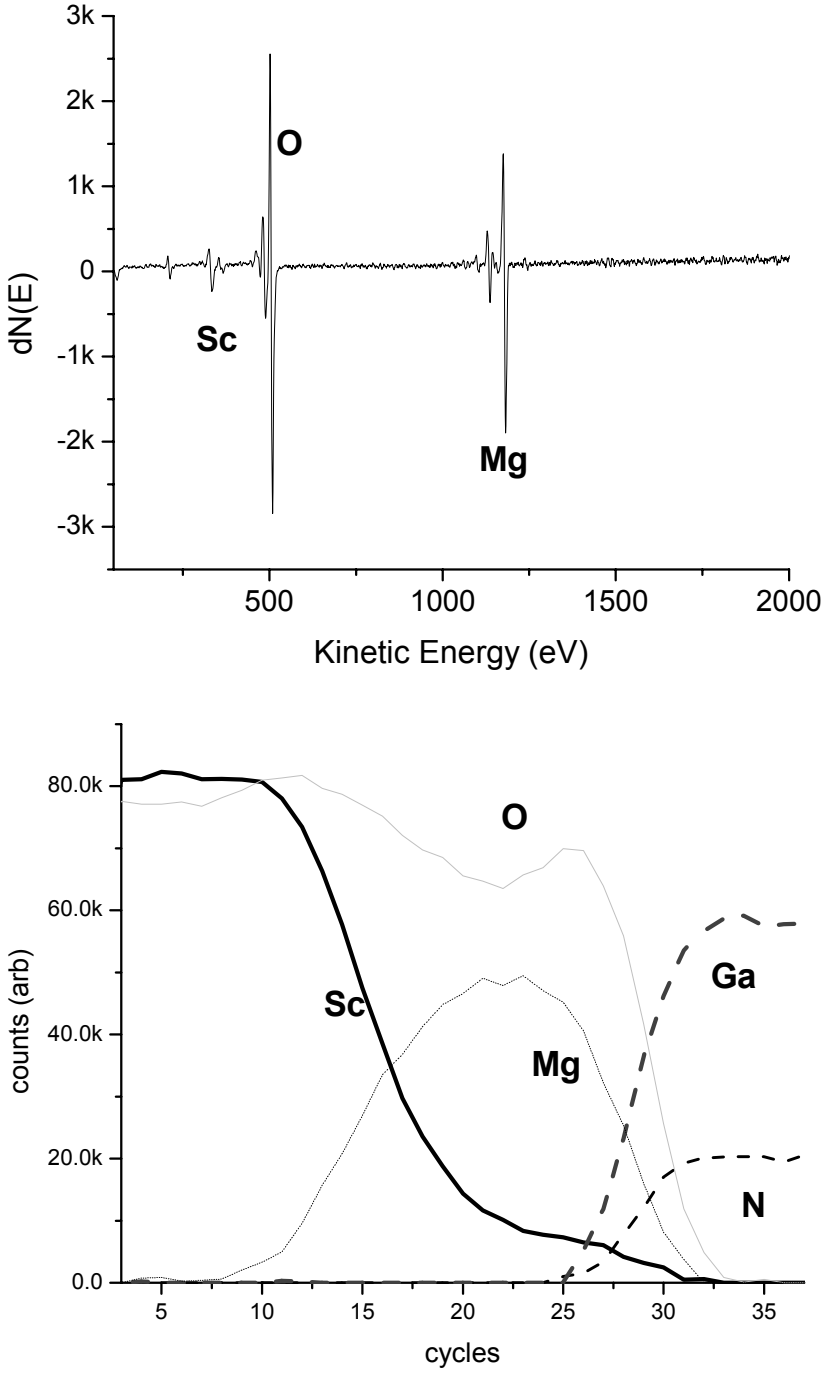

Figure 6-6. AES of MgScO with Sc_2O_3 capping layer.

A)

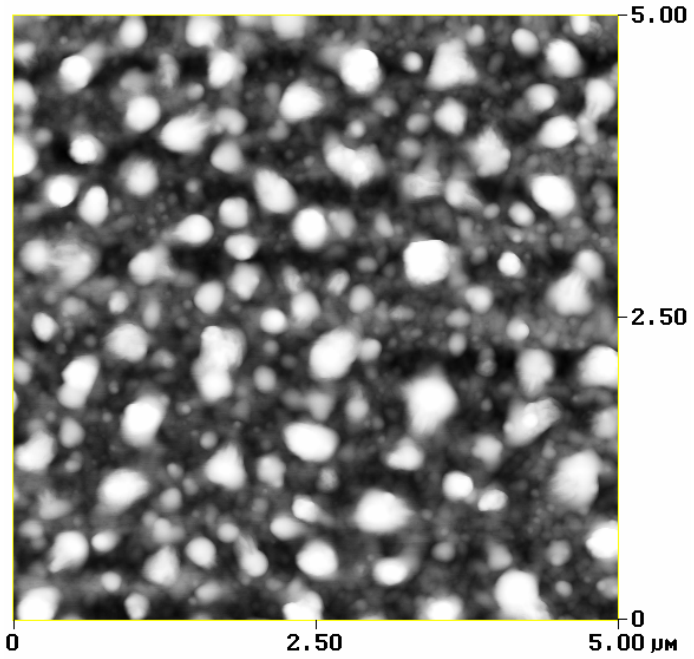

B)

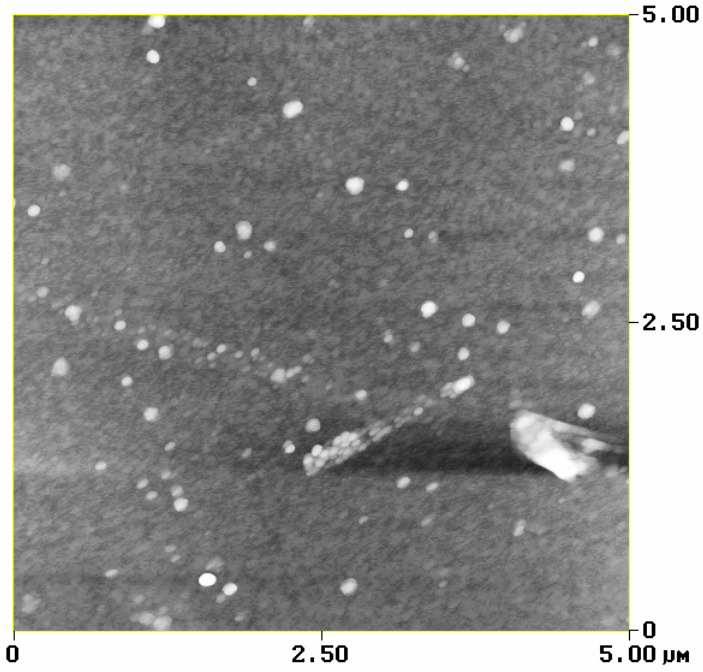

Figure 6-7. AFM of MgScO grown at 100˚C, A) uncapped, RMS = 34.868 nm and B) with a Sc_2O_3 cap, RMS = 1.69 nm.

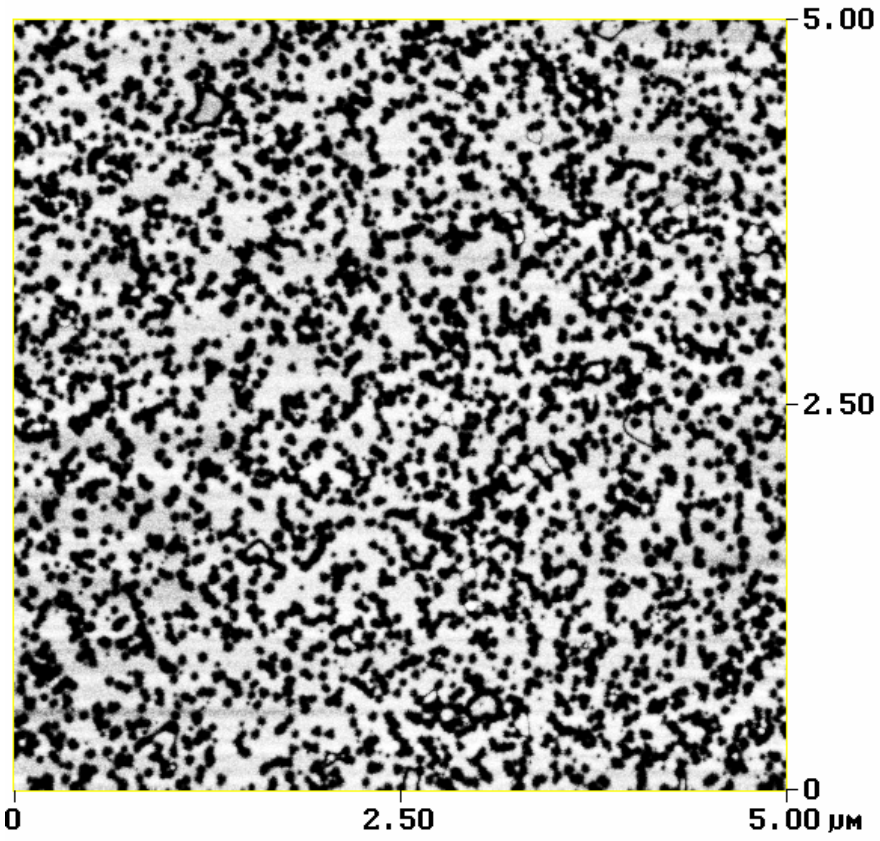

Figure 6-8. AFM of MgScO grown at 300˚C without capping layer, RMS = 10.345 nm.

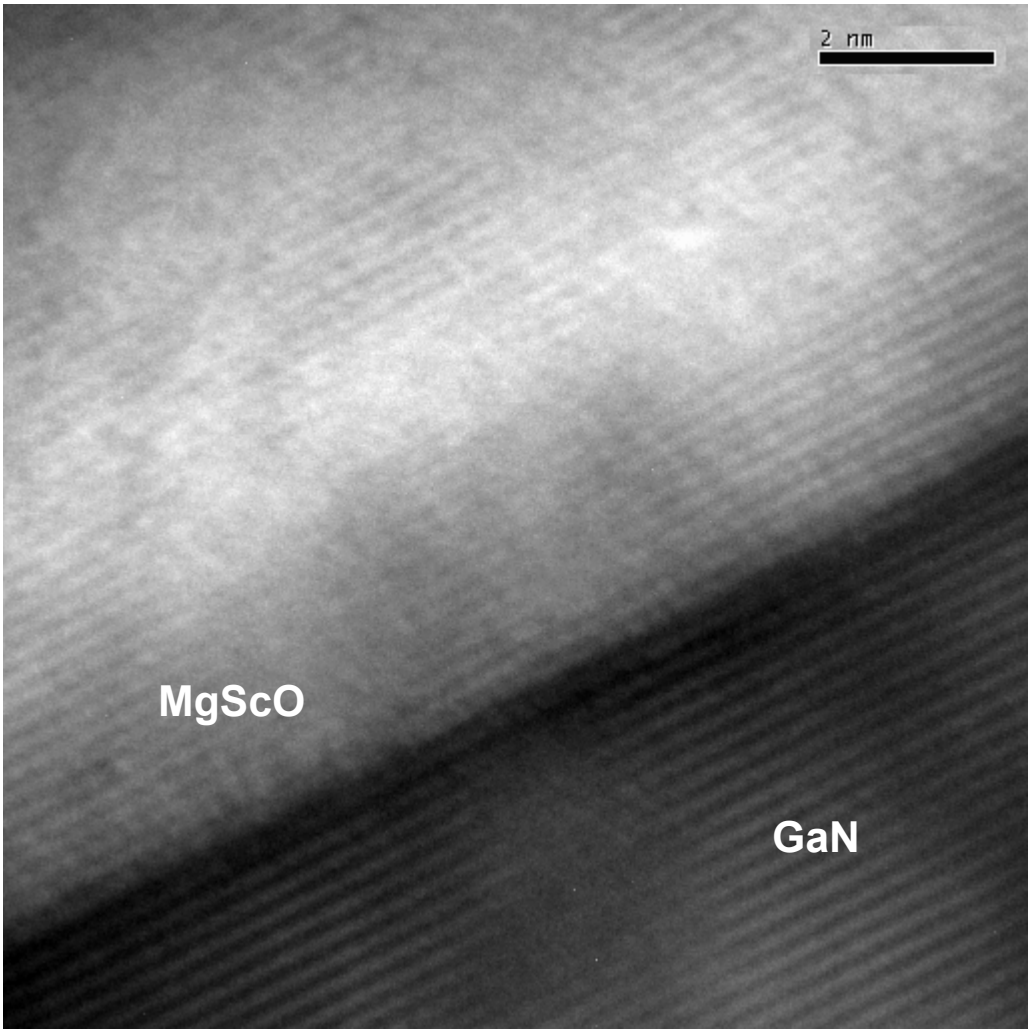

Figure 6-9. TEM of MgScO shows epitaxial growth of MgScO on GaN.

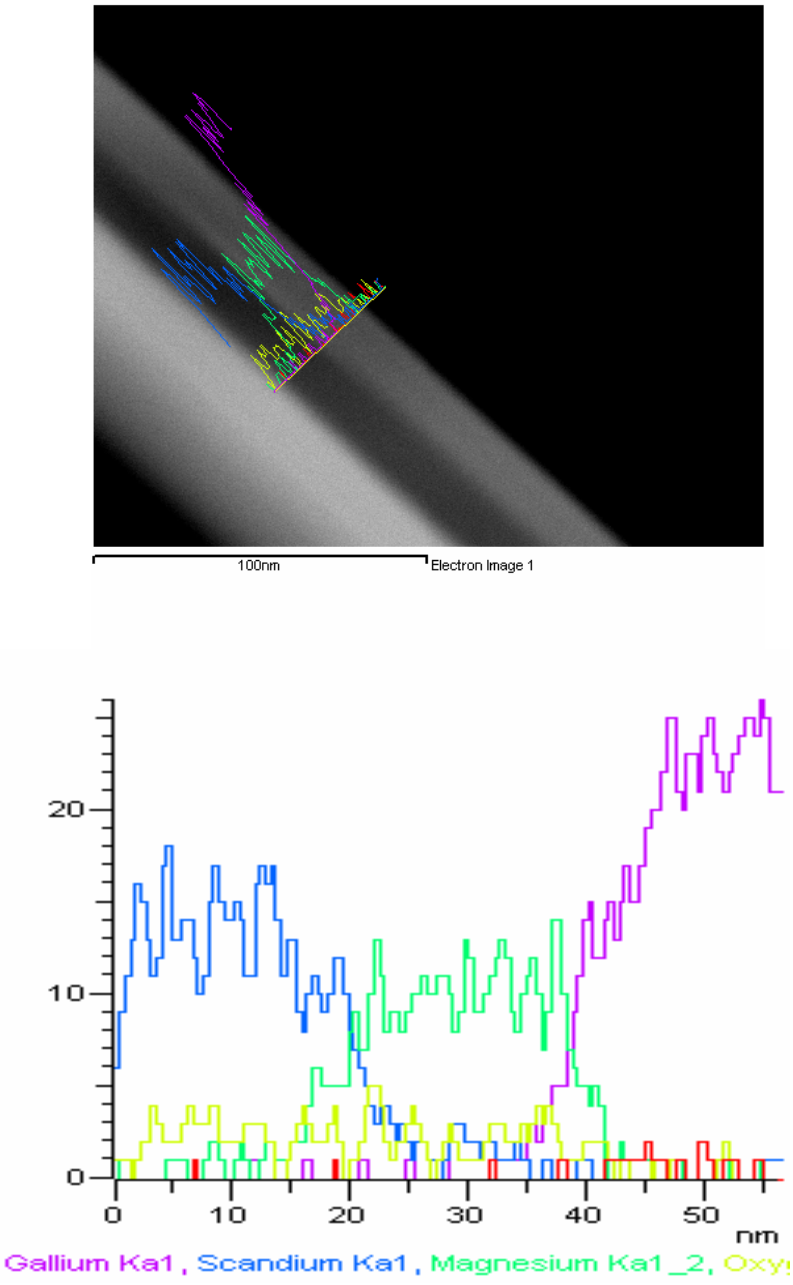

Figure 6-10. EDS of ScMgO showing that the composition of the film is MgScO and the cap layer is Sc_2O_3.

CHAPTER 7
ENVIRONMENTAL AND THERMAL STABILIY

7.1 Environmental Stability

Environmental stability is important for the viability of a gate oxide in production and long-term use. If the oxide reacts rapidly upon exposure to light, moisture, or atmospheric gases and its properties change, then it is not viable. The environmental stability of the oxides under study was tested under the accelerated aging conditions of 100% humidity and elevated temperature. A diagram of the accelerated aging experiment is shown in Figure 7-1. The stability of the films was measured as the change of the index of refraction, n, over time. The index of refraction was measured using a J.A. Woollam Spectroscopic Ellipsometer as described in Section 3.2.7 and Appendix A.

7.1.1 Magnesium Oxide

Despite all the good qualities of MgO, it has been found to be environmentally unstable as shown by SEM, (Figure 4-17). The MgO films degrade over time in atmosphere due to the presence of water vapor. It is believed that the water vapor reacts with the MgO to form magnesium hydroxide, $Mg(OH)_2$.[76,77] From device characteristics, it does not appear that the MgO under the metal contacts degrades, only the areas exposed to atmosphere. Capping layers of scandium oxide of various thicknesses were tried in order to prevent this degradation. Samples with scandium oxide caps of 5 nm, 10 nm, and 20 nm were compared to bare MgO under accelerated aging conditions, (Figure 7-1). For the bare, uncapped MgO sample, the index of refraction starts at 1.71 and after 20 days is 1.54, (Table 7-1). A capping layer of 5 nm greatly improves the

environmental stability of the MgO. The 10 nm and 20 nm capped MgO shows no apparent degradation over the entire duration of the aging study. The index of refraction for the 5 nm, 10nm and 20 nm caps remains about 1.64, 1.41, and 1.15, respectively.

7.1.2 Magnesium Calcium Oxide

Environmental stability of bare, uncapped MgCaO (60%Mg) was compared to MgCaO with a 20 nm scandium oxide cap. Uncapped MgCaO degraded more rapidly than the uncapped MgO, (Figure 7-3). The uncapped MgO showed rapid decrease in n over time, (Figure 7-2). For the bare, uncapped sample, the index of refraction starts at 1.62 and after 20 days is 0.89, (Table 7-1). The index of refraction for the 20 nm capped sample remained about 1.07. Thus the capping layer of scandium oxide improved the stability of MgCaO.

7.1.3 Magnesium Scandium Oxide and Scandium Magnesium Oxide

Environmental stability of bare, uncapped MgScO (2%Mg) was compared to MgScO with a 20 nm scandium oxide cap, (Figure 7-4). The uncapped MgScO did show some degradation but at a slower rate than the MgO. For the bare, uncapped sample, the index of refraction starts at 1.77 and after 20 days is 1.59, (Table 7-1). The index of refraction for the 20 nm capped sample remained about 1.31. The addition of scandium to the MgO did improveslightly the environmental stability of the oxide. The capped MgScO showed no apparent degradation over the duration of the study.

Due to the two-phase nature of the ScMgO films, no aging study was preformed on these oxides.

7.2 Thermal Stability

The thermal stability of the gate oxide is important for both operation and processing. If the oxide degrades upon exposure to moderate temperatures over an

extended time then the oxide is not suitable due to degradation at operational temperatures. More importantly if the oxide degrades upon annealing at elevated temperatures of up to 1000˚C then processing limitations become an issue as anneals for Ohmic contact formation and implant activation are typically done at elevated temperatures. The oxide films were annealed in an RTA at 1000˚C for 2 minutes to test their thermal stability. X-ray reflectivity (XRR), Section 3.2.6, was used to measure the interface roughness before and after annealing to determine the thermal stability of the film. Philips Electronics WinGixa software, Version V1.102, was used to model and interpret the results.

7.2.1 Magnesium Oxide

Uncapped MgO showed severe degradation or change in film properties after annealing, (Figure 7-5). The surface and interface roughness increased and the density of the oxide layer changed, (Table 7-2). The roughness of the GaN/MgO interface increased from 7.65 Å to 16.84 Å. The roughness of the MgO/Air interface increased from 35.4 Å to 56.33 Å. The density of the MgO film changed from 2.69 g/cm^3 to 3.33 g/cm^3. This is likely due to recrystallinzation of the polycrystalline MgO. The capping layer seems to reduce these effects (Figure 7-6), but it is still not stable under these conditions, (Table 7-2). The MgO/GaN interfacial roughness increases about the same amount for the capped sample as the uncapped sample.

7.2.2 Magnesium Calcium Oxide

Uncapped MgCaO (60% Mg) also showed degradation after annealing (Figure 7-7), but less severely than the MgO. The capped MgCaO showed only slight differences after annealing, (Figure 7-8). The majority of this difference comes from a change in the capping layer possibly due to recrystallization of the polycrystalline scandium oxide

capping layer. The MgCaO/GaN interface increases in roughness from 3.24 Å to 96.0 Å for the uncapped sample and from 25.58 Å to 51.76 Å for the capped sample after annealing, (Table 7-2). There was only a small change in the roughness of the capping layer after annealing.

7.2.3 Magnesium Scandium Oxide and Scandium Magnesium Oxide

Uncapped MgScO (2%Mg) showed degradation after annealing, (Figure 7-9). The GaN/MgScO interfacial roughness increased from 6.84 Å to 149 Å after annealing, (Table 7-2). The capped MgScO showed much less degradation after annealing (Figure 7-10), than the capped MgO and slightly less than the capped MgCaO. The addition of the scandium oxide capping layer greatly improved the thermal stability of the MgScO. The roughness of the GaN/MgScO interface went from 35.53 Å to 50.93 Å after annealing.

Due to the two-phase nature of the ScMgO films no thermal annealing was done on any of these samples.

Table 7-1. Ellipsometry data. Change in index of refraction, at t = 0 days, and t =20days.

	cap	n, t = 0 days	n, t= 20 days	change in n
MgO	no cap	1.71	1.5	0.21
	5 nm	1.64	1.66	0.02
	10 nm	1.41	1.42	0.01
	20 nm	1.17	1.14	0.03
MgCaO	no cap	1.62	0.89	0.73
	20 nm	1.07	1.01	0.06
MgScO	no cap	1.77	1.59	0.18
	20 nm	1.31	1.37	0.06

Table 7-2. XRR data of as-grown and annealed samples. Data modeled using Winixa software.

		Anneal	GaN/Oxide	Oxide/Cap or Air		Cap/Air	
			RMS (A)	RMS (A)	Density (g/cm3)	RMS (A)	Density (g/cm3)
MgO	no cap	Before	7.65	35.40	2.69	--	--
		After	16.84	56.33	3.33	--	--
MgO	capped	Before	6.69	37.05	3.35	15.06	1.14
		After	4.66	54.46	3.25	34.20	1.97
MgCaO	no cap	Before	7.52	3.24	3.24	--	--
		After	14.53	96.00	2.82	--	--
MgCaO	capped	Before	2.70	25.78	2.62	11.60	2.97
		After	3.00	151.76	1.75	22.70	2.97
MgScO	no cap	Before	6.84	4.20	3.97	--	--
		After	149.20	57.63	3.47	--	--
MgScO	capped	Before	4.24	35.53	3.38	14.32	2.05
		After	4.16	50.93	3.73	35.24	1.27

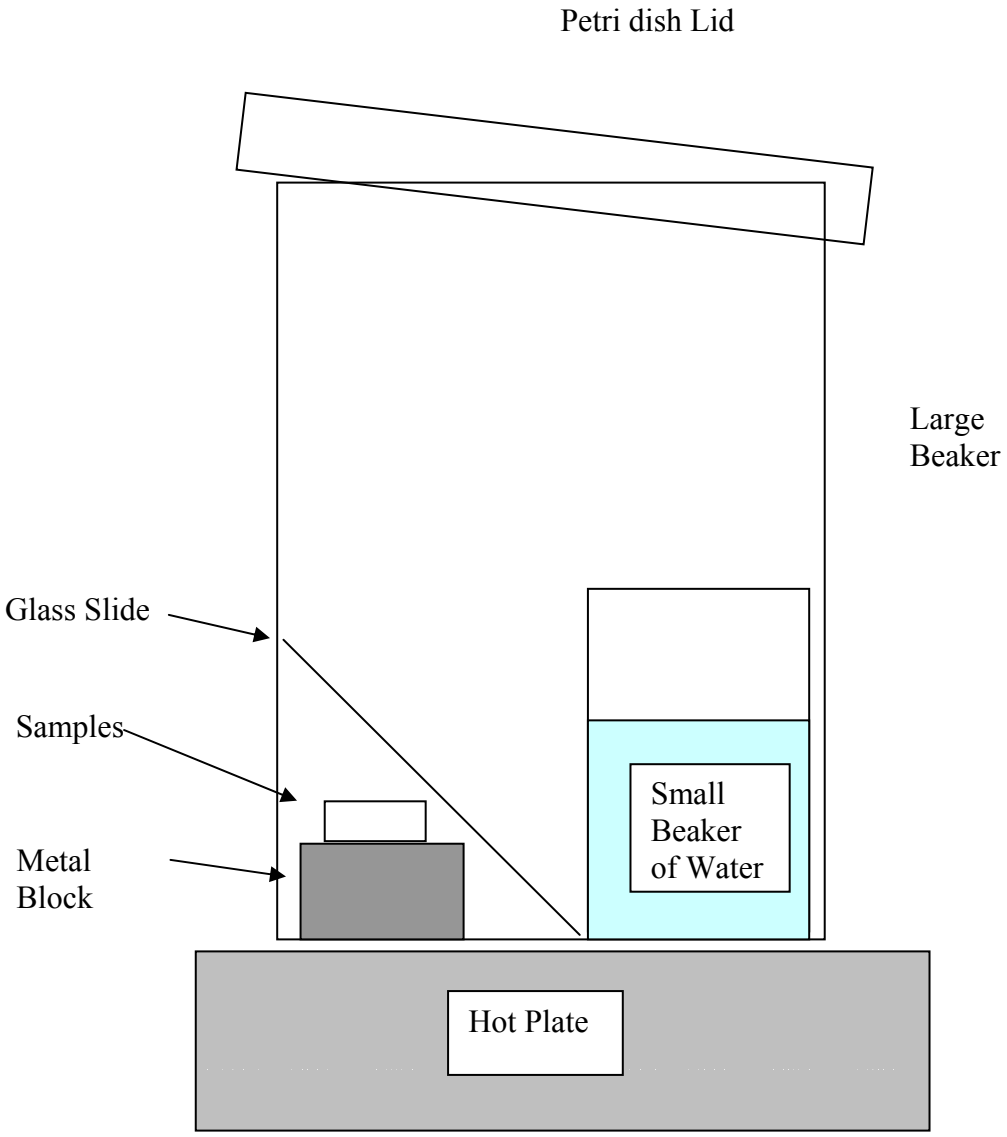

Figure 7-1. Accelerated aging experimental set up. The smaller beaker of water inside the larger beaker provides elevated humidity and the hot plate provides elevated temperature. The lid is angled such that condensation will drip down the side opposite of the samples. The glass slide provides protection from random drops of water. The metal block provides heat transfer to the samples while keeping them out of the water that collets on the bottom of the beaker.

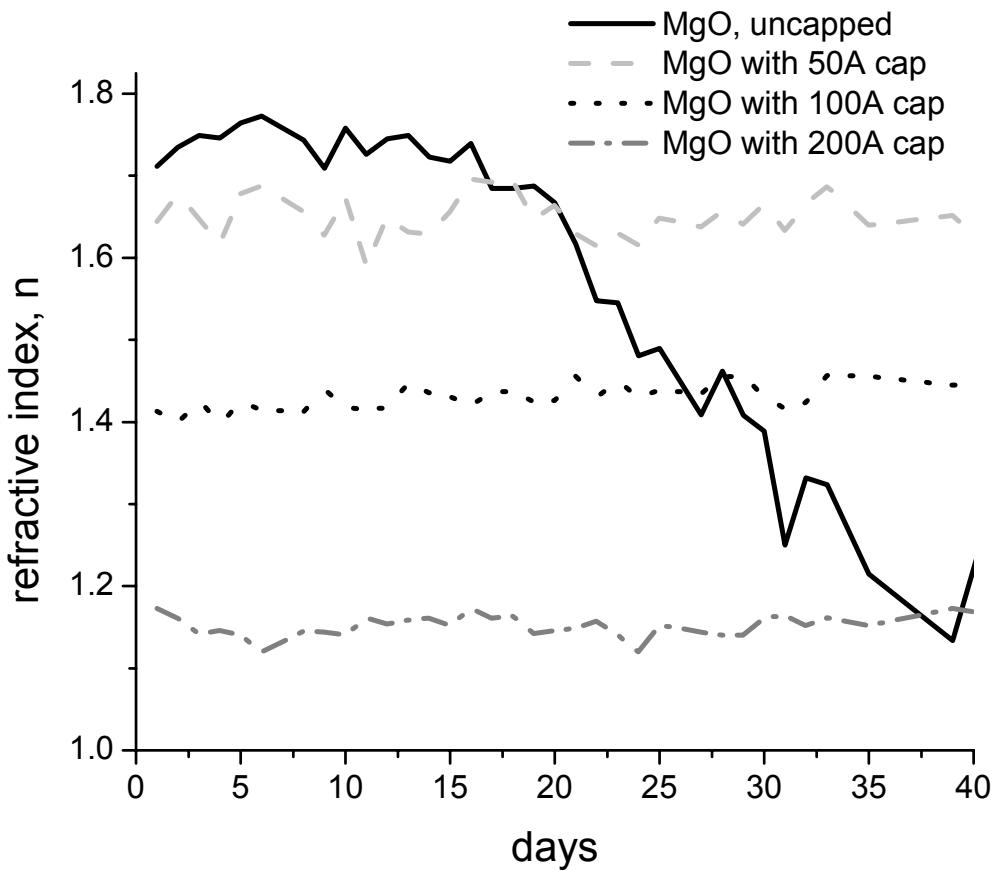

Figure 7-2. Ellipsometry of the degradation of MgO with and without a capping layer.

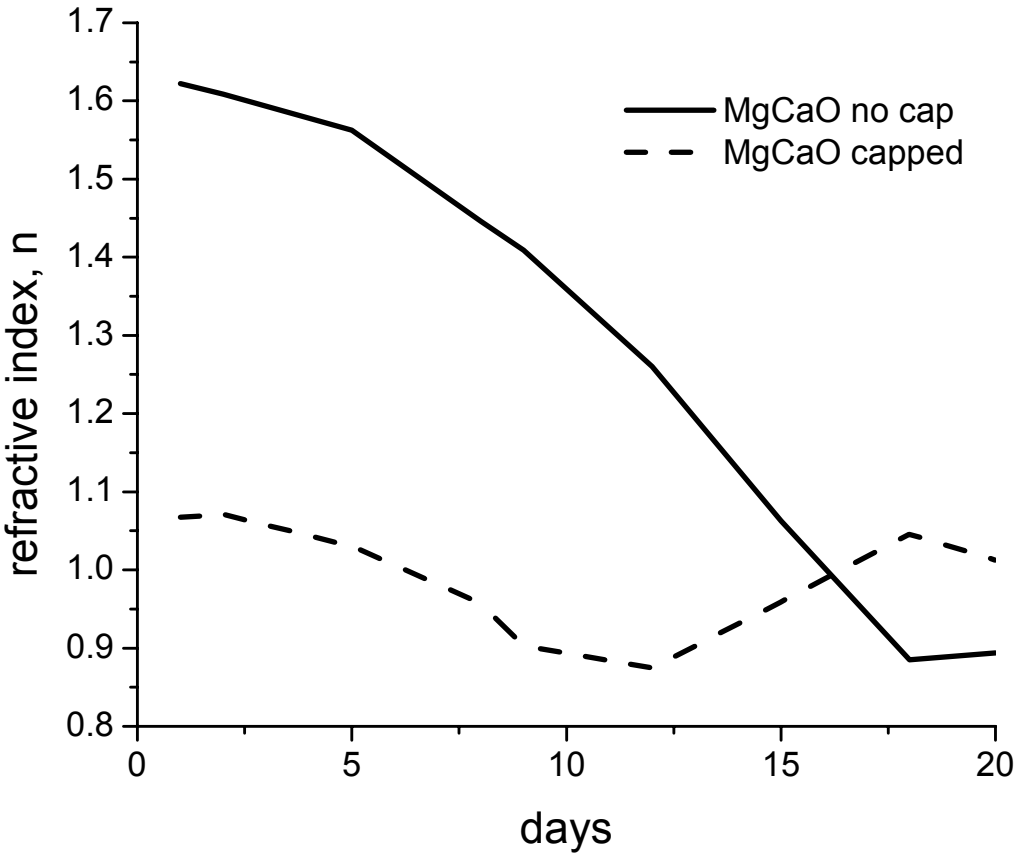

Figure 7-3. Ellipsometry of the degradation of MgCaO with and without capping layer.

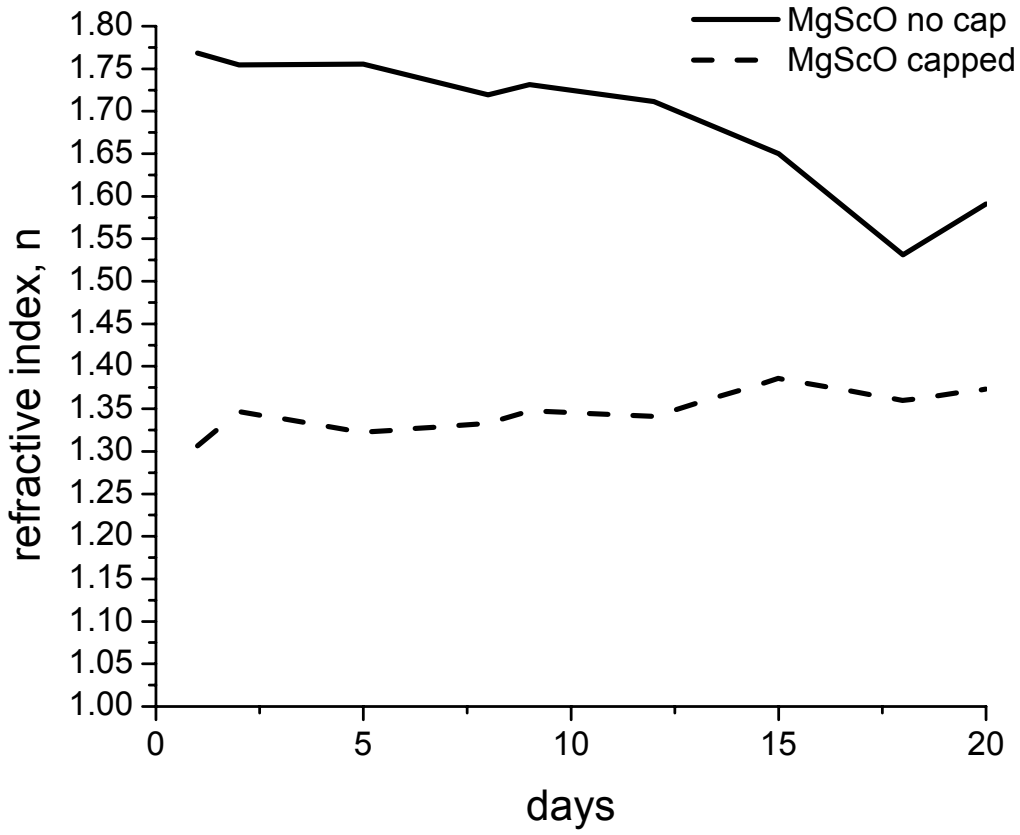

Figure 7-4. Ellipsometry of the degradation of MgScO with and without capping layer.

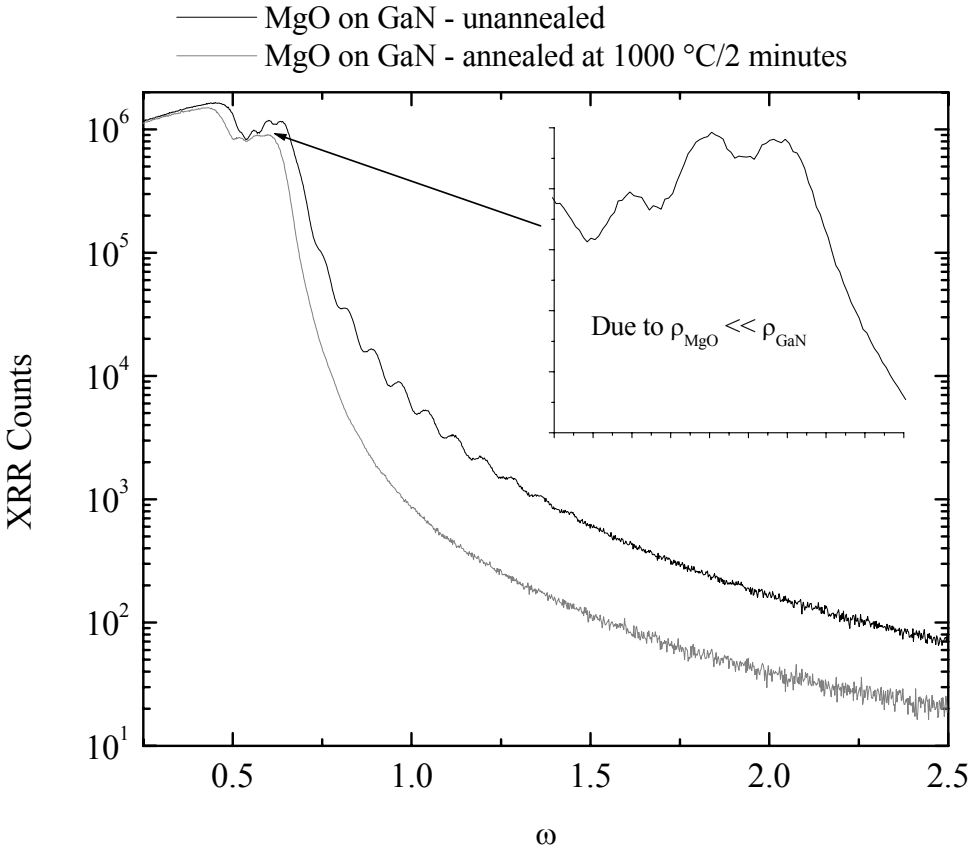

Figure 7-5. XRR of MgO uncapped, before and after annealing at 1000˚C for 2 minutes.

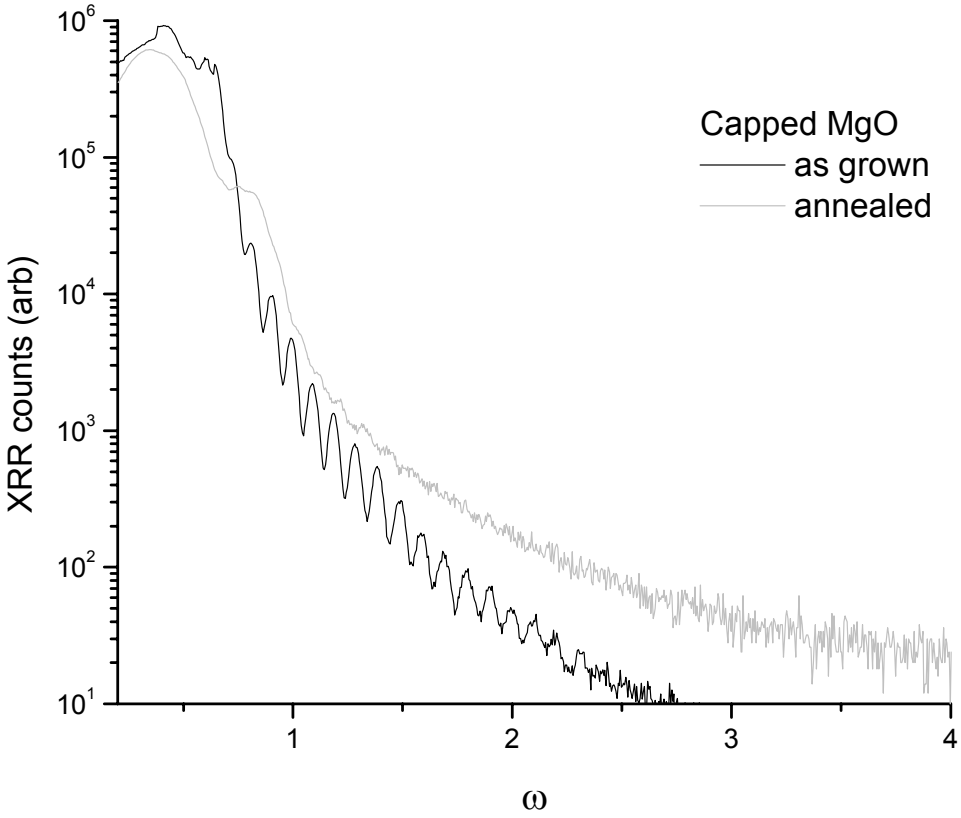

Figure 7-6. XRR of capped MgO before and after annealing at 1000˚C for 2 minutes.

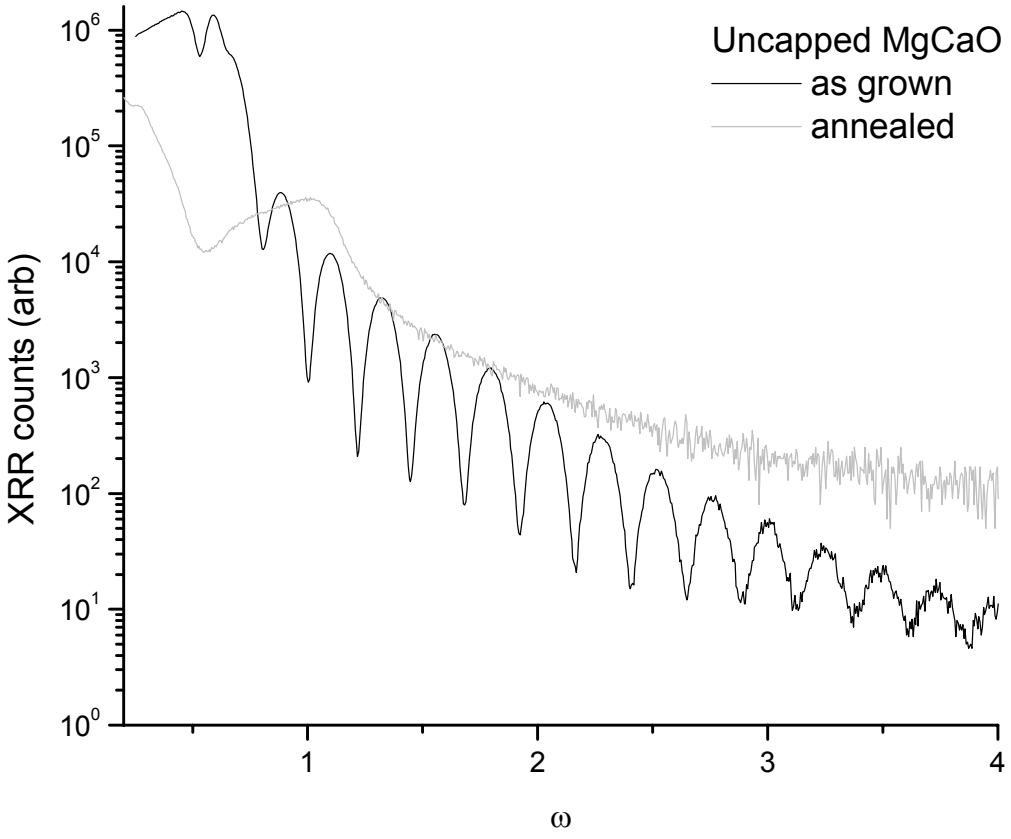

Figure 7-7. XRR of MgCaO uncapped before and after annealing at 1000˚C at 2 minutes.

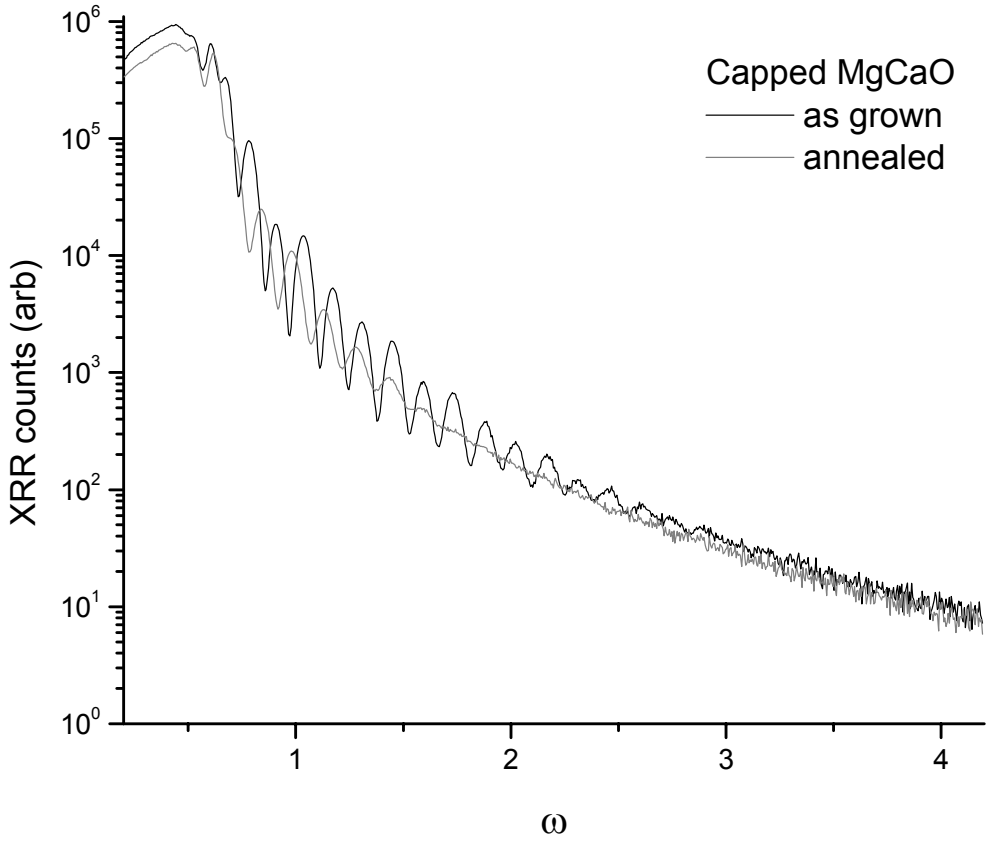

Figure 7-8. XRR of MgCaO capped before and after annealing at 1000˚C for 2 minutes.

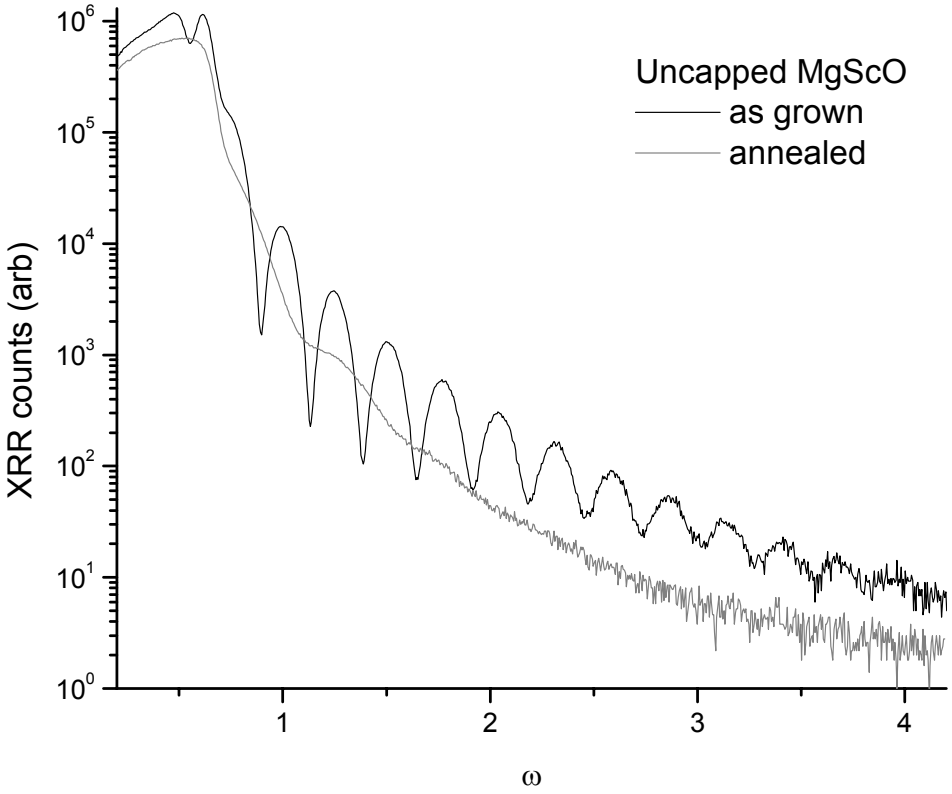

Figure 7-9. XRR of MgScO uncapped, before and after annealing at 1000˚C for 2 minutes.

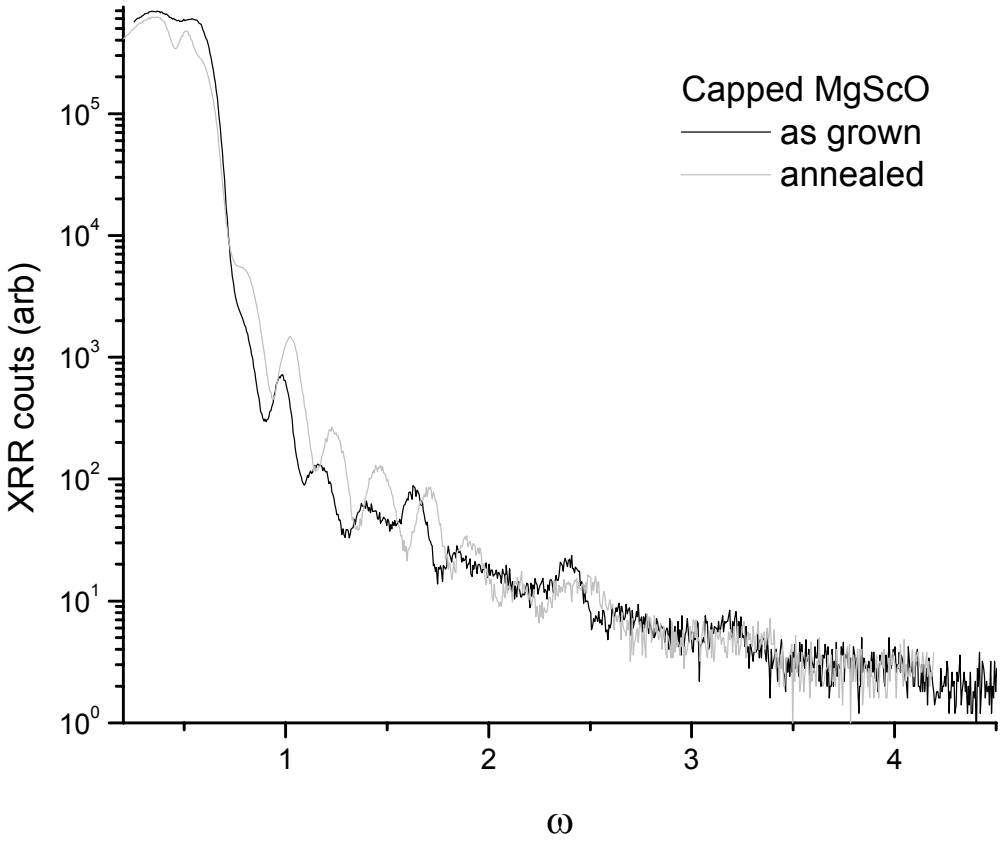

Figure 7-10. XRR of MgScO capped, before and after annealing at 1000˚C for 2 minutes.

CHAPTER 8
SUMMARY AND FUTURE WORK

8.1 Magnesium Oxide

Magnesium oxide was grown by gas source MBE on (0001) GaN using elemental Mg and atomic oxygen supplied from an ECR plasma source and an RF plasma source. The morphology of the ECR grown MgO was needle-like, while the RF grown magnesium oxide had a much smoother morphology. In both cases, the magnesium oxide was polycrystalline and highly textured toward the (111) direction. Breakdown fields of 1.0MV/cm for ECR grown MgO and 2.3 MV/cm for RF grown were obtained. Interface state densities of $4x10^{11}$ MV/cm were measured for the polycrystalline MgO/GaN heterostructure of either plasma source. RF grown MgO was found to be superior to ECR grown oxides and thus all further growths used the RF plasma for the oxygen source.

Increasing the oxygen pressure during growth was found to improve the morphology and produced an Mg/O ratio closer to that obtained for single crystal MgO. By contrast, electrical characterization of MgO/GaN diodes showed the best breakdown field and interface state density at the lower oxygen pressures. It is believed that the superior electrical behavior at lower oxygen pressures is due to the higher ion energy obtained at the lower pressures. This is in agreement with the poorer electrical characteristics obtained using ECR oxygen plasmas, which produce significantly lower ion energies than RF plasmas. Unfortunately, the MgO films are environmentally and thermally unstable.

8.2 Magnesium Calcium Oxide

Magnesium calcium oxide was grown on (0001) GaN by gas-source molecular beam epitaxy. Depth profiling Auger electron spectroscopy (AES) showed a steep increase in the Ca concentration at the surface relative to the oxide/GaN interface indicative of severe Ca segregation which was enhanced at lower growth rate. In spite of this segregation, XRD of films deposited at 100°C showed no evidence of phase separation, and the addition of Ca did increase the lattice constant of the material thus reducing the bond mismatch to GaN.

A digital growth technique was used to suppress the segregation of the Ca in the film. AES showed an improvement in the uniformity of the depth profile of the ternary film, especially near the surface, and enhanced oxygen incorporation in the digitally grown samples as compared to the continuously grown samples. HRXRD shows the same (222) peak position for both growth sequences using the same metal fluxes during growth. AFM shows that the surface of the digital sample is smoother than that of the continuous samples. Thus all evidence suggests that the digital growth sequence produces higher quality material than a continuous sequence. The reduction in lattice match enables the growth of an epitaxial single crystalline oxide on GaN, which does not relax into nanocrystallites as film thickness increases.

Changing the shutter sequence allows for more exposure of Ca during growth and resulted in increased incorporation of Ca. The standard 10 sec Mg/10 sec Ca shutter sequence produced a bond mismatch of –1.5%. The bond mismatch for the 8 sec Mg/12 sec Ca shutter sequence was +0.96 percent. The 5 sec Mg/15 sec Ca shutter sequence produced a bond mismatch of +3.04%. Thus it appears a lattice matched film would be

produced for a shutter sequence of 9 sec Mg/11 sec Ca. Bond mismatch can be varied from tensile to compressive strain. Future experiments should include trying the 9/11 shutter sequence.

8.3 Scandium Magnesium Oxide and Magnesium Scandium Oxide

Scandium magnesium oxide was grown on (0001) GaN by gas-source molecular beam epitaxy. Increasing the magnesium cell temperature during growth of ScMgO was found to increase the growth rate, have little effect on surface roughness, and create a second phase which was magnesium rich at Mg cell temperatures over 330°C. Increasing the substrate temperature was found to have little effect on the growth rate and dramatically increased surface roughness. The maximum Mg concentration that could be obtained in single-phase material was found to be 28% Mg as determined by AES.

Magnesium scandium oxide was grown on (0001) GaN by gas-source molecular beam epitaxy. The maximum amount of Sc that could be incorporated into MgO was ~9%. TEM showed this film to be epitaxial and single crystalline. The incorporation of scandium reduced the amount of strain in the MgO and produced a film that was single crystal. AFM showed that the MgScO grown at a substrate temperature of 100°C was much smoother with the scandium oxide cap.

8.4 Environmental and Thermal Stability

MgO has been found to be unstable due to reactions with moisture in the atmosphere. A scandium oxide cap of 5 nm was shown to improve the environmental stability during an experimental accelerated aging experiment. After annealing the MgO film at 1000˚C for 2 minutes the film degraded and the interface roughness was

drastically increased, probably due to recrystallization of the MgO. The scandium oxide cap reduced the degradation of the film.

MgCaO was shown to degrade faster than MgO in atmosphere. As with MgO, a scandium oxide cap improved the environmental degradation of the oxide. The MgCaO was annealed at 1000˚C for 2 minutes. The uncapped MgCaO also degraded upon annealing. The capping layer significantly increased the thermal stability of the film. The best structural quality and stability were obtained using the MgCaO with the Sc_2O_3 cap.

Both uncapped and capped MgScO were aged as well at an accelerated rate. The addition of Sc was shown to have no significant effect on rate of the aging process. The capping layer prevented environmental aging as seen with the other two oxides. The thermal stability of the MgScO was better than that of the MgO. The capping layer improved this further.

Further experiments are needed to determine the temperatures at which each of these oxide films degrade to determine a maximum processing temperature. Processing issues related to the differences in etch rates between the Sc_2O_3 cap and the MgCaO must be addressed so that the electrical effects of the change in bond mismatch can be determined.

APPENDIX A
ELLIPSOMETRY

Ellipsometry is a very sensitive surface and thin film measurement technique that uses polarized light. It derives its sensitivity, which is greater than a simple reflection measurement, from the determination of the relative phase change in a beam of reflected polarized light. Also, ellipsometry is more accurate than intensity reflectance because the absolute intensity of the reflected light does not have to be measured. For rotating analyzer ellipsometers, the detectors used only have to have a linear intensity response and do not need to be calibrated in an absolute sense, such that no special reference samples need to be maintained.

Many simple samples may be characterized by ellipsometric measurements at a single wavelength. The use of spectroscopic measurements using multiple wavelengths provides much more information about the sample and also provides the ability to acquire data in spectral regions where the measured data are most sensitive to the model parameters which are to be determined. In many cases the dispersion of the optical constants of a given materials is known, or the optical constants may be parameterized in such a way as to enforce some type of dispersion on the optical constants (Cauchy, Lorentz, and parametric semiconductor models for example). In this case the acquisition of spectroscopic data allows the user to take advantage of this knowledge to obtain more information from the analysis of the ellipsometric data than would be possible when analyzing data from a single wave length.

Ellipsometry measures the change in the polarization state of light reflected from the surface of a sample. Fundamentally, ellipsometry refers to the measurement of the polarization state of a light beam. However, ellipsometric measurements are usually performed in order to describe an "optical" system that modifies the polarization state of a beam of light. For thin film sample analysis, the "optical system" is simply the reflection of light from the sample.

The measured values are expressed as psi (Ω) and delta (Δ). These values are related to the ratio of Fresnel reflection coefficients R_p and R_s for p- and s-polarized light, respectively, Equation A-1.

$$\rho = \frac{R_p}{R_s} = \tan(\Psi)e^{i\Delta} \qquad \text{(A-1)}$$

Because ellipsometry measures the ratio of two values it can be highly accurate and very reproducible. Because the ratio is a complex number, it is also contains "phase" information (Δ), which makes the measurements very sensitive.

Ellipsometry can be used to determine thin film thicknesses, thin film optical constants, and in many case both for the same film. For many samples, ellipsometry is sensitive to film thickness on a submonolyer level. Ellipsometry has also proven to be the premier technique for determining optical constants in the near-UV, visible, and near-IR wavelength ranges.

Ellipsometry uses polarized light for measurements. The first step in understanding polarized light is understanding an electromagnetic (EM) plane wave, which is a solution of Maxwell's equations for electromagnetic fields. In this section we review the properties of the plane wave, the Jones matrix calculus for describing polarization state and the various types of light polarization encountered in ellipsometric experiments.

A.1 Maxwell's Equations and the EM Plan Wave

Maxwell's equations from a non-conducting, non-dispersive medium appear as follows:

$$\vec{\nabla} \bullet \vec{E} = 0 \tag{A-2}$$

$$\vec{\nabla} \bullet \vec{B} = 0 \tag{A-3}$$

$$\vec{\nabla} \times \vec{E} + \frac{1}{c}\frac{\partial \vec{B}}{\partial t} = 0 \tag{A-4}$$

$$\vec{\nabla} \times \vec{B} - \frac{\mu\varepsilon}{c}\frac{\partial \vec{E}}{\partial t} = 0 \tag{A-5}$$

Where E and B are the electric field and magnetic fields, c is the speed of light, and μ and ε are the permeability and the dielectric function, respectively. Any propagating light beam must obey these equations.

These equations can be combined to yield the wave equations for the electric field:

$$\vec{\nabla}^2 \vec{E} - \frac{1}{\nu^2}\frac{\partial^2 \vec{E}}{\partial t^2} = 0 \tag{A-6}$$

where the optical impedance υ is defined as

$$\nu = \frac{c}{\sqrt{\varepsilon\mu}}. \tag{A-7}$$

A solution of the electric field wave equation is the electromagnetic plane wave:

$$E(\vec{r},t) = \vec{E}_o \exp\left(\frac{i2\pi\tilde{n}}{\lambda}\vec{q} \bullet \vec{r}\right)\exp(-i\varpi t), \tag{A-8}$$

Where $\vec{q}$ is a unit vector along the direction of wave propagation, $\vec{n}$ is the complex index of refraction n + ik, λ is the wavelength of the light in vacuum, ω is the angular frequency of the wave, and E_o is a complex vector constant specifying the amplitude and

polarization state of the wave. Such a wave propagating in a medium with no absorption (k=0), (Figure A-1).

The E-field, B-field, and the direction of propagation are all orthogonal with respect to each other. Because of the relationship between the fields, only the E-field and the direction of propagation are required to completely define a plane wave. Polarization states are usually in terms of the direction and phase of the E-field vector, only.

If the imaginary part of the complex index of refraction, the extinction coefficient, is non-zero, the amplitude of the wave will decay exponentially as it propagates according to the following expression

$$E \propto \exp(-2\pi kz/\lambda) \tag{A-8}$$

Where k is the extinction coefficient, z is the distance of propagation in length units, and lambda is the wavelength, in the same length units as z. The wave will then decay to 1/e of its original amplitude after propagating a distance, D_p, known as the penetration depth, given by

$$D_p = \lambda/2\pi k \tag{A-9}$$

This is an important concept, as many materials exhibit large values of the extinction coefficient such that the light beam may penetrate a few tens of nm or less into the material. We cannot expect to gain any information from a film or interface unless the light beam used in the ellipsometric experiment penetrates to the film on interface that we are studying, and is also able to propagate back out of the sample after reflection from the interface. For this reason it is usually not possible to measure the thickness of metal films of more than 50nm in thickness, as very little of the incident light beam reaches the bottom of the metal films and gets back out of the top to reach the detector.

A.2 Jones Vectors and Matrices

One of Maxwell's equation states that the divergence of the displacement field must equal 4π times the local charge density

$$\Lambda \text{ X } D = 4\pi \rho \qquad \text{(A-10)}$$

Where D is the displacement field and ρ is the charge density. In the absence of space charges, ρ is zero and if we assume the material to be isotropic the above equation reduces to

$$\Lambda \text{ X } E = 0 \qquad \text{(A-11)}$$

Where E is the electric field. This requires that he components of the polarization vector E_o must lie in the plane perpendicular to the direction of beam propagation, again assuming the material in which the beam is propagating is isotropic. In this case, we can describe the polarization states of any beam by specifying its components along any two orthogonal axes in the plane perpendicular to the direction of the beam propagation.

In ellipsometric experiments it is common to use the p- and s- directions as the two orthogonal basis vectors use to express beam polarization states, (Figure A2-2). The p-direction is defined as lying in the plane of the incidence, defined as the plane containing the incident and reflected beams and the vector normal tot eh sample surface. The s-direction (from Senkrecht, German for perpendicular) lies perpendicular to the p-direction such that the p-direction, s-direction, and the direction of the propagation (in that order) define a right hand Cartesian coordinate system.

We can now express any totally polarized beam by specifying the components of the electric field of the beam along the p- and s-directions. The components are complex

numbers, which may be conveniently written as two-component vector, known as the Jones vector

$$E = \begin{bmatrix} E_p \\ E_s \end{bmatrix} \tag{A-12}$$

We may now express the action of any component or sample upon the polarization state of the propagating beam very simply by means of a 2x3 transfer matrix, known as the Jones matrix. The diagonal elements of the Jones matrix represent the change of amplitude and phase of the p- and s- components of the beam, while the off-diagonal elements describe the transfer of energy from the p-component to the s-component, and vice versa.

The Jones matrix calculus provides a very convenient and powerful means of describing optical systems, such as ellipsometers, and will be used throughout the remainder of this section.

A.3 Light Polarization States

If one looks at the E-filed vector of linearly polarized light in a plane perpendicular to the direction of propagation (x-y plane), one sees that the E-field lies in one line at all time. The tip of the E-fled vector traces out a line segment as a function of time. This linear polarization can be described as two component waves propagating in phase, in the same direction, but with orthogonal E-fields in the x and y directions. The polarization state is defined with respect to some physical frame of reference. The orientation of the total E-filed with respect to the coordinate system is defined by the relative amplitudes of the E_x and E_y fields. The Jones vector representation of linearly polarized light is

$$\begin{bmatrix} E_p e^{i\phi} \\ E_s e^{i\phi} \end{bmatrix}, \tag{A-13}$$

where Φ is a phase angle, which must be identified for both components. For special cases of p- and s-polarized light, the normalized Jones vectors have the particularly simple forms (up to and arbitrary multiplicative complex constant)

$$\begin{bmatrix} 1 \\ 0 \end{bmatrix} \text{p-polarized and } \begin{bmatrix} 0 \\ 1 \end{bmatrix} \text{s-polarized.} \tag{A-14}$$

If the E_x and E_y fields are equal in magnitude but 90˚ out of phase, then the filed vector traces out a circle as a function of time. There are two types of circular polarization. If, looking into the propagating beam, the electrical field vector is precessing counterclockwise around the circle the beam is left-circularly polarized, and normally the Jones vector for the beam is

$$\frac{1}{\sqrt{2}}\begin{bmatrix} 1 \\ i \end{bmatrix}. \tag{A-15}$$

If the electric field vector is precessing clockwise around the circle, the beam is right-circularly polarized, and the corresponding Jones vector for the beam is

$$\frac{1}{\sqrt{2}}\begin{bmatrix} 1 \\ -i \end{bmatrix}. \tag{A-16}$$

A line segment and a circle are special types of ellipses; therefore, linearly and circularly polarized lights are just special cases of elliptically polarized light. Ellipsometry measures Ψ and Δ by determining the polarization of ellipse of the probe beam, hence its name.

A.4 Single Films on Thick Substrates

The case of polarized light reflection from a single film on an optically thick substrate may be solved in a number of ways. The most instructive is an analytical solution based on the summation of all reflected beam component such as the multiple

reflections of the incident light beam which occur in the film for the case of a single film on an optically thick substrate, (Figure A-3).

There are in principle an infinite number of reflected and transmitted beams, however, the splitting of the beam, into reflected and transmitted component at each reflection quickly reduce the amplitude if the subsequent reflections such that eventually the reflected and transmitted beams die out. Also, any absorption in the film will attenuate the beams as they propagate.

We now take advantage of the fact that our previous derivation for the Fresnel reflection and transmission coefficients of a bulk system is locally valid for the reflection and transmission of a beam from any interface. Thus, we calculate Fresnel coefficients, which are functions for the ambient and film indices of refraction and the angle of incidence, which are valid for any beam incident on the air/film interface or the film/substrate interface.

The terminology for this calculation will be as follows. First the incident beam is denoted E^{inc}, which will represent ether a p- or s-polarized wave of unit amplitude. The reflected beams will be labeled E_n^{refl}, where n denotes the nth reflection and refl denotes reflected beams. Transmitted beams will be labeled E_n^{trans}, where n denotes the nth transmitted beam and trans denotes transmitted beams.

Quantities relating to the ambient medium will have the subscript 0, quantities relating to the films will have the subscript 1, and quantities relating to the substrate will have the subscript 2. This notation is used because it is easily extended to any number of layers. Fresnel reflection and transmission coefficients for both interfaces will be given two numbers for a subscript, where the first number denotes the region from which the

beam is incident on the interface, and the second number denotes the region on the other side of the interface.

Our calculation will be performed independently for the p- and s-polarized incident beams, as any incident beams of arbitrary polarization can be described as a linear combination of s- and p-polarization states. As a result, we do not need to label the Fresnel coefficients with p or s. For example, r_{01} denotes the complex Fresnel reflection coefficient for a beam incident upon the film, region 1, and from the ambient medium (region 0), while t_{12} denotes the Fresnel transmission coefficient for a beam incident on the film/substrate interface from the film side.

In order to complete the model we must also be able to connect the propagating waves between the top and bottom interfaces of the film. A propagating wave will have the form given in Equation A-8, and it is a simple matter to show that propagation of a wave across the film, in either direction, yields a wave of the following form.

$$E_{after} = E_{before} \cdot \exp(-i2\beta) \tag{A-17}$$

where β is the phase thickness or optical thickness of the film for the given wavelength and angle of incidence, given by

$$\beta = 2\pi n_1 \frac{d}{\lambda} \cos\Phi_1 = 2\pi \frac{d}{\lambda} \sqrt{n_1^2 - n_0^2 \sin^2 \Phi_0} \ , \tag{A-18}$$

in which d is the film thickness and λ is the wavelength, in the same units as the film thickness. It is now a simple matter to writ down the expressions for the successive reflected beams:

$$E_1^{refl} = r_{01} E_{incident} \tag{A-19}$$

$$E_2^{r} = t_{10} t_{01} r_{12} e^{-j2\beta} E_{incident} \tag{A-20}$$

$$E_3^r = t_{10}t_{01}r_{10}\left(r_{12}\right)^2 e^{-j4\beta}E_{incident} \tag{A-21}$$

$$E_4^r = t_{10}t_{01}\left(r_{10}\right)^2\left(r_{12}\right)^3 e^{-j6\beta}E_{incident} \tag{A-22}$$

and so on. We can now identify the following general form for the nth reflected beams:

$$E_n^r = t_{10}t_{01}\left(r_{10}\right)^{n-2}\left(r_{12}\right)^{n-2} e^{-j(2n-2)\beta} \tag{A-23}$$

Now we sum the reflected beams using this functional form, as shown below.

$$E_{total}^r = \left[r_{01} + t_{10}t_{01}e^{j2\beta}\sum_{n=2}^{\infty}\left(r_{10}\right)^{n-2}\left(r_{12}\right)^{n-2} e^{-j2n\beta} \right]\cdot E_{incident}, \tag{A-24}$$

We next take advantage of the following identities,

$$r_{01} = -r_{10}, \tag{A-25}$$

$$t_{10}t_{01} = 1 - r_{01}^2 \tag{A-26}$$

Inserting A-25 and A-26 into A-24 and evaluating the resulting convergent series, we find the following expression for the total reflected beam.

$$E_{total}^r = \left(\frac{r_{01} + r_{12}e^{-j2\beta}}{1 + r_{01}r_{12}e^{-j2\beta}} \right)\cdot E_{incdnet} \tag{A-27}$$

This equation is valid for p- and s-polarized input beams, provided the corresponding p- or s-polarized Fresnel reflection coefficient for the interfaces are employed. We now define the pseudo-Fresnel reflection coefficients for any arbitrary sample in terms of the incident, reflected, and transmitted beams. If we use p-polarized Fresnel coefficients for the evaluation of A-27, we can find the p-polarized pseudo-Fresnel reflection coefficient R_p as follows

$$R_p \equiv \frac{E_{total}^r}{E_{incident}} = \frac{r_{01} + r_{12}e^{-j2\beta}}{1 + r_{01}r_{12}e^{-j2\beta}} \tag{A-28}$$

with a similar equation holding for the s-polarized case. These coefficients are easily identified from A-27. We may now calculate Ψ and Δ from a broader definition of the ellipsometric parameters, valid for any sample exhibiting pseudo-Fresnel p- and s-polarized reflection coefficients R_p and R_s respectively:

$$\rho = \tan\Psi e^{i\Delta} \equiv \frac{R_p}{R_s} \tag{A-29}$$

The summation of multiple transmitted beams may also be performed in a similar manner to obtain the polarization state of the transmitted beam.

There are many mathematical formalisms that may be used to calculate the pseudo-reflection coefficient and/or Ψ and Δ for multi-layered structures but that is too complex to go into at this time.

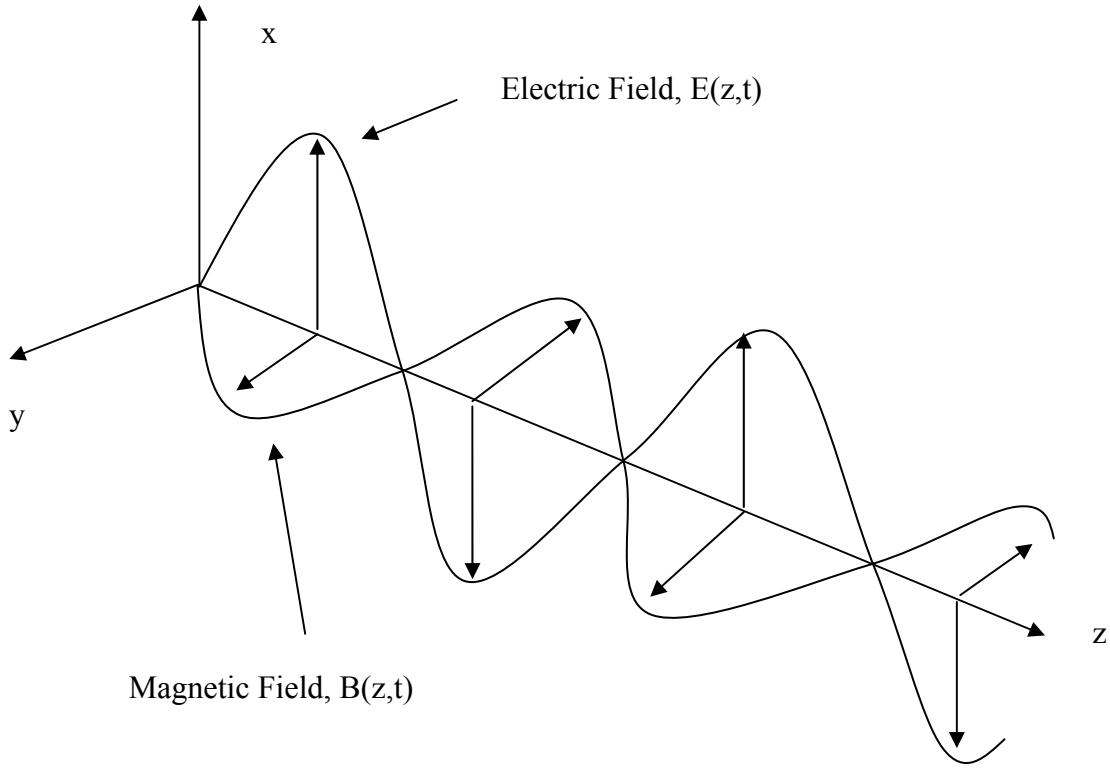

Figure A-1. An electromagnetic plane wave.

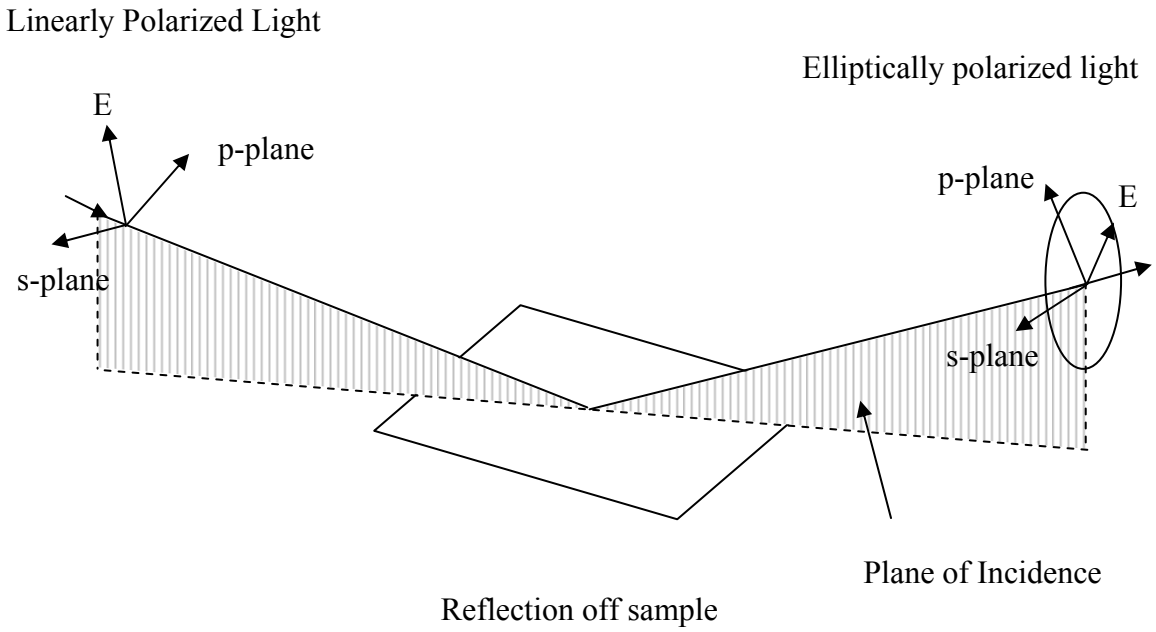

Figure A-2. Geometry of an ellipsometric experiment, showing p- and s-directions.

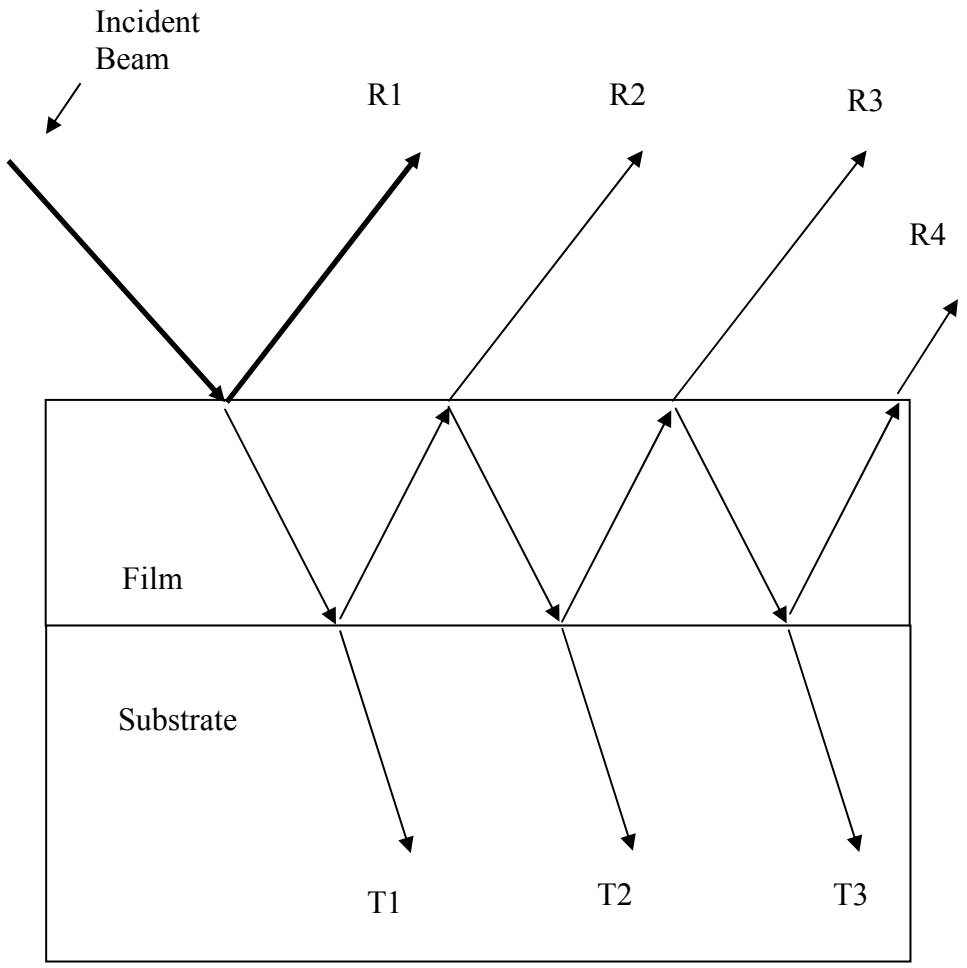

Figure A-3. Multiple reflected and transmitted beams for a single film on an optically thick substrate.

APPENDIX B
TEM SAMPLE PREPARATION

There are many ways to make TEM cross-sectional samples. For materials as brittle as GaN on sapphire the main technique has been the old fashioned method of hand grinding and polishing to electron transparency. A newer method that is being used to make cross-sectional TEM samples for many materials is focused ion beam, FIB, milling followed by lift-out. These two sample preparation methods are described below.

B.1 Old-fashioned Hand Grinding-

Sample preparation begins by cleaving thin strips of the material, about 1 cm long. These strips are glued together, using G-1 epoxy from Gatan, film side to film side. Other strips of sapphire are glued to add support, (Figure B-1). Tweezers are used to hold the strips together during the curing process to ensure thin glue lines. This stack of strips are polished using 320 grit SiC paper to create two parallel sides, perpendicular to the glue line. This is further polished using 600 grit SiC paper and a final polish with 3-5 micron diamond slurry on 800 grit SiC paper. The final thickness of the polished piece is 20 to 30 microns, (Figure B-2). This piece is glued to a nickel support grid, approximately 100mm thick, using the Gatan G-1 glue, (Figure B-3).

The sample is thinned further by using a Gatan Duo ion mill. The ion mill uses an argon ion beam accelerated toward the sample to remove material by collision. The settings of the ion mill are 5 kV and 0.7 mA per beam. The milling angle is adjusted from a starting range of 18° to a final range of 13°. The ion mill uses two ion guns, 180°

apart, for milling of both sides of the sample. The sample is also rotated to allow for a more uniform milling process. The final sample thickness is about 100 nm.

B.2 Focused Ion Beam Milling

Focused Ion Beam (FIB) milling uses Ga ions to mill out a sample from a bulk piece of material. The bulk material must be coated with carbon or another conductive material to prevent charging of the surface so that it can be imaged with the ions or electrons. My samples were affixed to a FIB sample stub with carbon paint. and then carbon coated with to a thickness of about 500Å. Once the sample is mounted and coated, the sample is ready to be loaded into the FIB.

First ensure all of the beams are off and the nitrogen tank is not empty before venting the chamber. Place sample on the stage and use “dog ear” tool to make a rough adjustment for the z-height of the sample. Remove “dog ear” tool and pump down the chamber. Then, turn on the high tension, electron and ion beams, and the GIS heating (Pt source). Before depositing platinum, the eucentric position needs to be aligned and the electron beam and the ion beam need to be linked. The eucentric is the height at which there is minimal shift in position with a large change in tilt. This ensures that the sample will not hit the needle or detectors in the chamber. To link the beams, focus and locate a piece of debris near the desired sample area and select zero beam-shift. This ensures that the ion beam and the electron beam are always focused on the same location. The electron beam and the ion beam are 52 degrees different in tilt and will not show the same image with out this step. Focus on the piece of debris using one beam, switch to the other beam, and locate the same point with the x and y knobs. The Auto FIB program can be used at this point.

The protective platinum layer (1x1x20 μm) is then deposited to protect the surface of the sample during milling. The sample is now ready to be milled.

The initial trenches are milled at a high current (7000 pA). A series of trenches are milled to either side of the desired sample area and the sample gets progressively thinner, (Figure B-4). The beam current used for milling is reduced (2000 pA-300 pA) as well as the sample gets thinner to reduce damage and redeposition on the sample. At about a sample thickness of 0.5 microns, the sample is under cut which frees the bottom of the sample from the bulk of the material, (Figure B-5). The thinning process is continued until sample is at its desired thickness. Then the ends of the sample are cut free from bulk material, (Figure B-6). Once the sample is completely free from the bulk, it is removed from FIB chamber.

Now the sample is lifted out from trench with glass rods and place on copper grid that has a thin layer of carbon to hold the sample. Sample sticks to the glass rods and the grid by static electricity. This procedure is called lift-out or micromanipulation.

Sample is now ready to be looked at in the TEM.

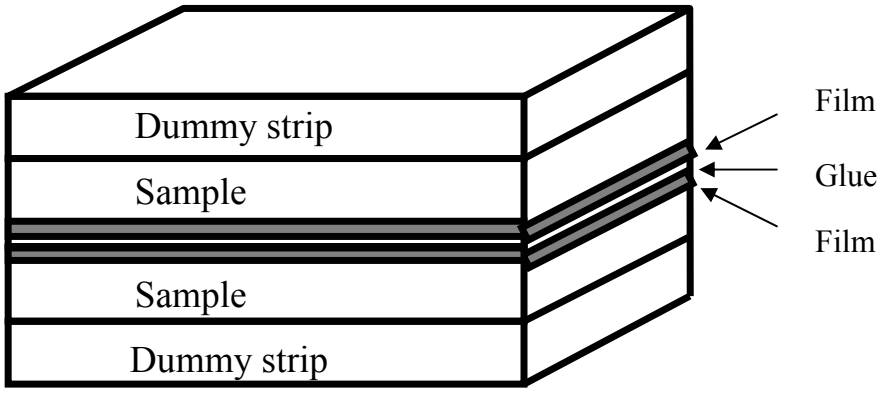

Figure B-1. Strips of sample and support sapphire glued together into a sample stack.

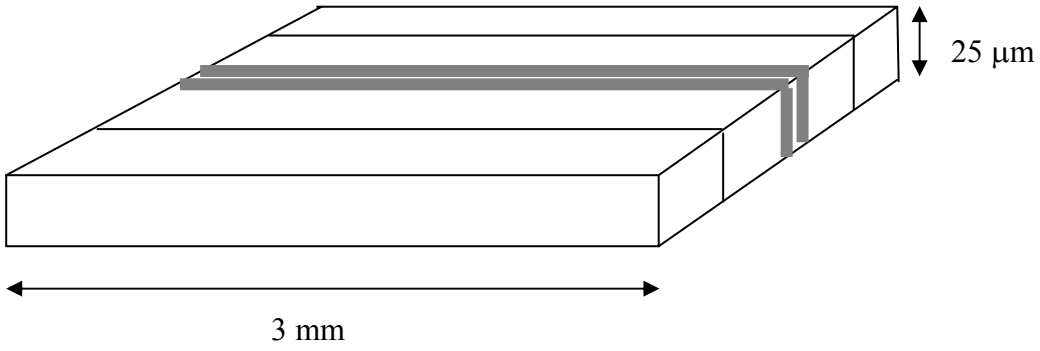

Figure B-2. TEM sample polished to 25 μm thick.

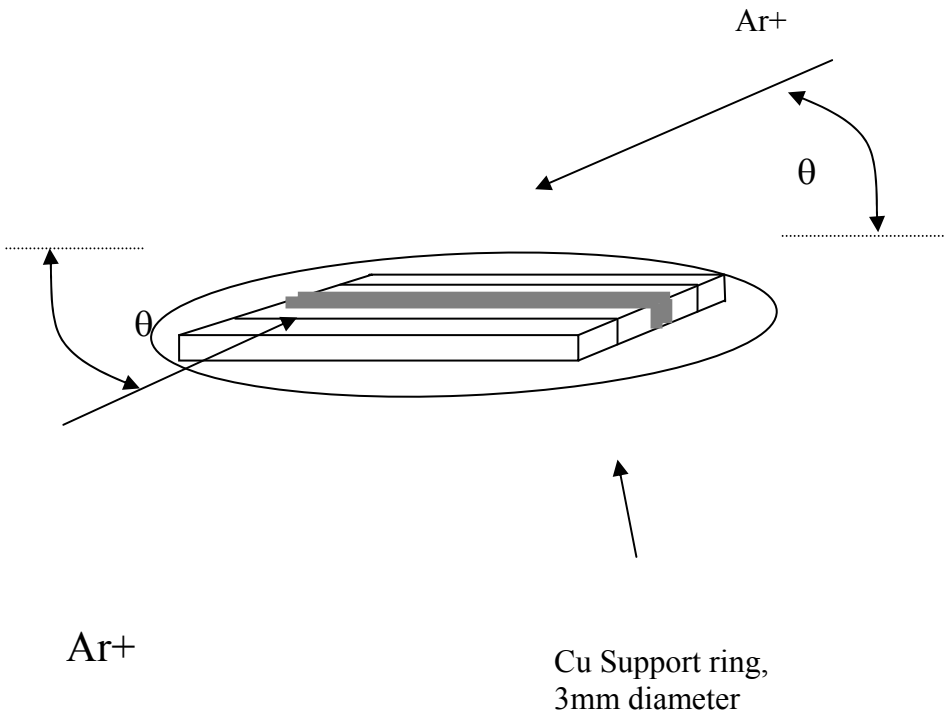

Figure B-3. The sample glued to a 3mm Cu support ring and orientation of ion milling. Angle θ is the ion beam angle with respect to the plane of the sample. (B.P. Gila 2000)

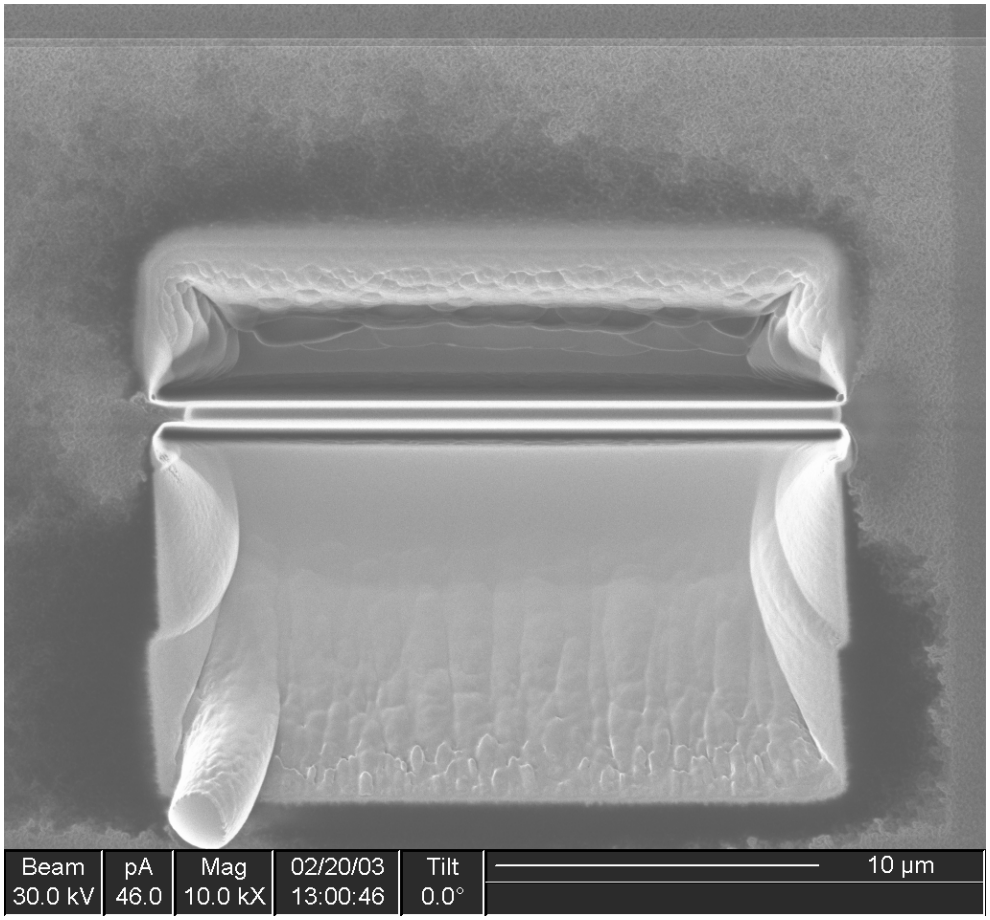

Figure B-4. Top view of FIB thinned sample.

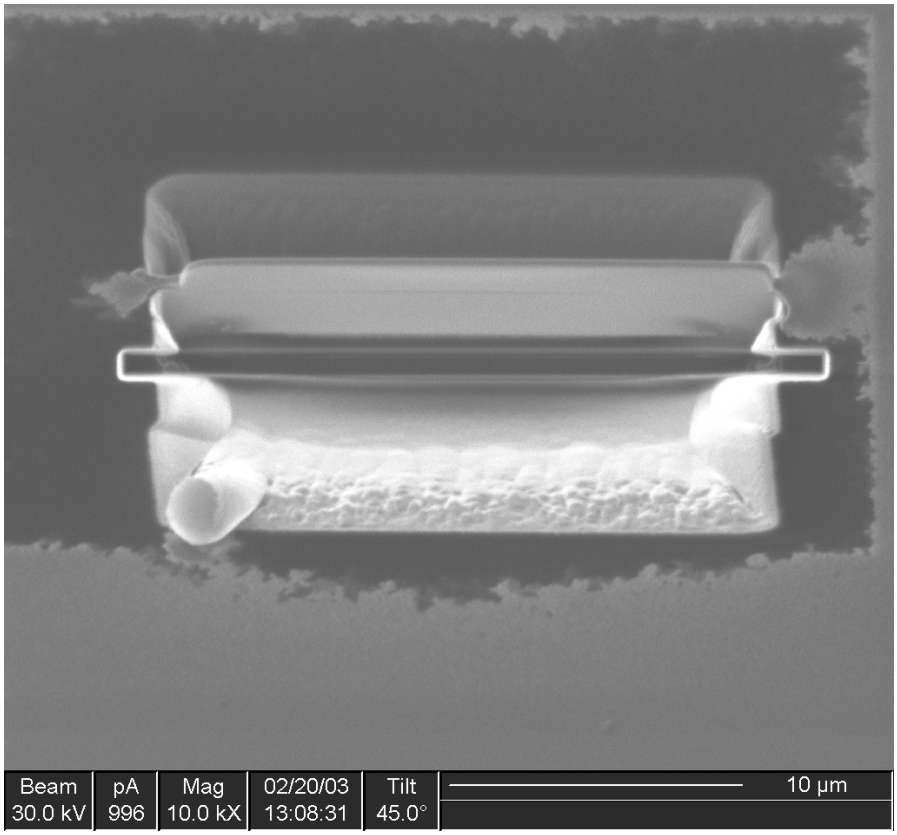

Figure B-5. Tilted picture of undercut step of FIB sample preparation.

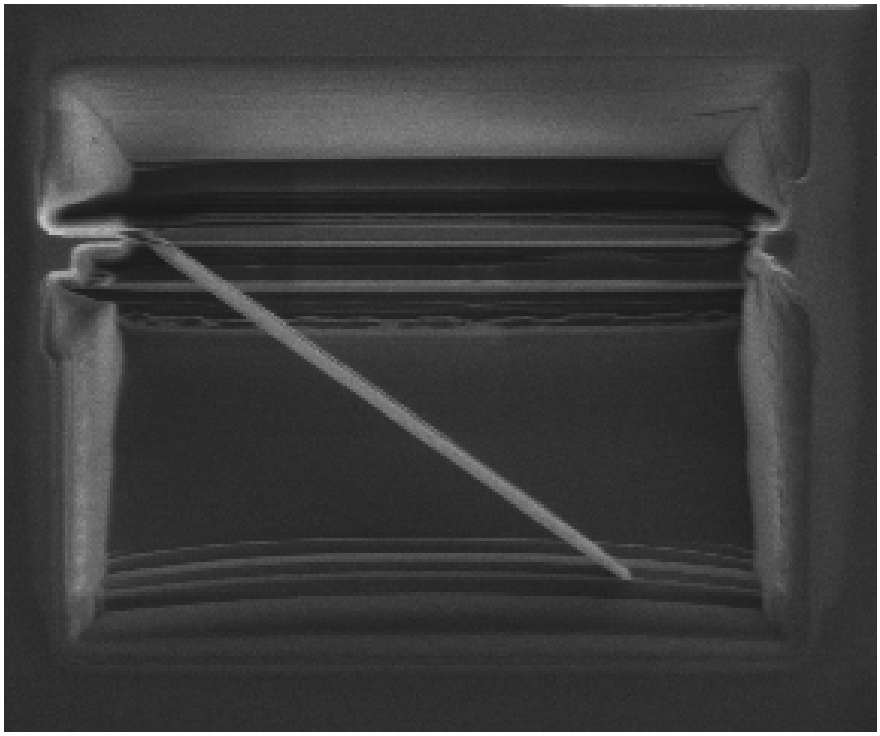

Figure B-6. Sample is now cut free and ready for lift-out.

LIST OF REFERENCES

1. M. Hong, M Passlack, J.P. Mannaerts, J. Kwo, S.N.G. Chu, N. Moriya, S.Y. Hou, V.J. Fratello, *Journal of Vacuum Science and Technology B*, **14**(3), 2297 (1996)

2. F.Ren, M. Hong, W.S. Hobson, J.M. Kuo, J.R. Lothian, J.P. Mannaerts, J. Kwo, Y.K. Chen, A.Y. Cho, *Tech. Dig. Int. Electron Devices Meeting*, 943 (1996)

3. J. Kwo, D.W. Murphy, M. Hong, J.P. Mannaerts, R.L. Opila, R.L. Masaitis, A.M. Sergent, *Journal of Vacuum Science and Technology B*, **17**(3), 1294 (1999)

4. J. Kwo, D.W. Murphy, M. Hong, R.L. Opila, J.P. Mannaerts, A.M. Sergent, R.L. Masaitis, *Applied Physics Letters*, **75**(8), 1116 (1999)

5. L.W. Tu, Y.C. Lee, K.H. Lee, C.M. Lai, I. Lo, K.Y. Hsieh, M.Hong, *Applied Physics Letters*, **75**(14), 2038 (1999)

6. A.R. Korton, M. Hong, J. Kwo, J.P. Mannaerts, N. Kopylov, *Physical Review B*, **60**(15), 10913 (1999)

7. M. Hong, Z.H. Lu, J. Kwo, A.R. Korton, J.P. Mannaerts, J.J. Krajewski, K.C. Hsieh, L.J. Chou, K.Y. Cheng, *Applied Physics Letters*, **76**(3), 312 (2000)

8. S.J. Pearton, F. Ren, A.P. Zhang, G. Dang, X.A. Cao, K.P. Lee, H. Cho, B.P Gila, J.W. Johnson, C. Mnier, C.R. Abernathy, J. Han, A.G. Baca, J.I. Chyi, C.M Lee, T.E. Nee, C.C. Chuo, S.N.G. Chu, *Materials Science and Engineering B*, **82**, 227-231 (2001)

9. D.R. Askeland, *The Sciemce and Engineering of Materials, 3rd ed*., PWS, Boston MA, 1994

10. R. Wolfson and J.M. Pasachoff, *Physics*, Little, Brown and Company, Boston, 1987

11. J. W. Mayer, S. S. Lau, *Electronic Materials Science*, Macmillan, New York, 1990

12. C. T. Sah, *Fundamentals of Solid-State Electronics*, World Scientific, New Jersey, 1991

13. H.C. Casey Jr, G.G. Fountain, R.G. Alley, B.P Keller, S.P. Denbaars, *Applied Physics Letters* **68**, 1850 (1996)

14. M. Sawada, T. Sawada, Y. Yamagata, K. Imai, H. Kumura, M. Yoshino, K. Iizuka, H. Tomozawa, *Proceedings of the Second International Conference on Nitride Semiconductors*, Tokushima, **482** (1997)

15. S. Aurlkumaran, T. Egawa, H. Ishikawa, T. Jimbo, M. Umeno, *Applied Physics Letters*, **73**(6) 809-811 (1998)

16. S.L. Rumyanysev, N. Pala, M.S. Shur, R. Gaska, M.E. Levinshtein, M. Asif Khan, G. Simin, X. Hu, J. Yang, *Journal of Applied Physics*, **90** (1), 310-314 (2001)

17. T.E. Cook, Jr. C.C. Fulton, W.J. Mecouch, K.M. Tracey, R.F. Davis, E.H. Hurt, G. Lucovsky, R.J. Nemanich, *Journal of Applied Physics* **93** (7), 3995-4004(2003)

18. K.M. Chang, C.C. Cheng, C.C. Lang, Electrical properties of SiN/GaN MIS diodes formed by ECR-CVD, *Solid-State Electronics* **46,** 1399-1403(2002)

19. T. Hashizumu, S. Ootomo, T. Inagaki, H. Hasegawa, *Journal of Vacuum Science and Technology B***, 21**(4), 1828-1830 (2003)

20. L.J. Guido, P. Mitev, M. Gherasimova, B. Gaffey, *Applied Physics Letters*, **72**, 2005 (1998)

21. T.P. Ma, *Microelectronics Journal* **34,**363-370 (2003)

22. B. Gaffey, G. Chong, L. Guido, X.W. Wang, T.P. Ma, *Applied Physics Letters*, **42**, 2145 (1998)

23. F. Ren, C.R. Abernathy, J.D. MacKenzie, B.P. Gila, S.J. Pearton, M. Hong, M.A. Marcus, M.J. Schuman, A.G. Baca, R.J. Shul, *Solid State Electronics* **42**, 2177 (1998)

24. H. Kawai, M. Hara, F. Nakamura, T. Asatsuma, T. Kobayashi, S. Imanaga, *Journal of Crystal Growth* **189/190**, 738 (1998)

25. S.D. Wolter, B.P. Luther, D.L. Waltermyer, C. Onneby, S.E. Mohney, R.J. Molnar, *Applied Physics Letters* **70**, 2156 (1997)

26. S.D. Wolter, S.E. Mohney, H. Venugopalan, A.E. Wickenden, D.D. Koleske, *Journal of the Electrochemical Society* **145**, 629 (1998)

27. Y. Nakano, T. Kachi, T. Jimbo, *Journal of Vacuum Science and Technology B* **21**(5), 2220-2222 (2003)

28. M. Hong, J. Kwo, S.N.G. Chu, J.P. Mannaerts, A.R. Kortan, H.M. Ng, A.Y. Cho, K.A. Anselm, C.M. Lee, J.I. Chyi, *Journal of Vacuum Science and Technology B* **20** (3), 1274-1277 (May/June 2002)

29. D.J. Fu, Y.H. Kwon, C.J. Park, K.H. Baek, H.Y. Cho, D.H. Shin, C.H. Lee, K.S. Chung, *Applied Physics Letters* **80** (3), 446-448 (2002)

30. L.H. Peng, C.H. Liao, Y.C. Hsu, C.S. Jong, C.N. Huang, J.K. Ho, C.C. Chiu, C.Y. Chen, *Applied Physics Letters* **76**, 511 (2000)

31. D.J. Fu, T.W. Kang, Sh.U. Yuldashev, N.H. Kim, S.H. Park, J.S. Yun, K.S. Chung, *Applied Physics Letters* **78**, 1309 (2001)

32. D. Fu, S.U. Yuldashev, N.H. Kim, Y.S. Ryu, J.S. Yun, S.H. Park, T.W. Kang, K.S. Chung, *Japanese Journal of Applied Physics- Part 2* **40**, L10 (2001)

33. C. T. Lee, H.W. Chen, H.Y. Lee, Metal-oxide-semiconductor devices using Ga_2O_3 dielectrics on n-type GaN, *Applied Physics Letters* **82**(24), 4304-4306 (2003)

34. T. Rotter, R. Ferretti, D. Mistele, F. Fedler, H. Klausing, J. Stemmer, O.K. Semschinova, J. Aderhold, J. Graul, *Journal of Crystal Growth* **230**, 202-206 (2001)

35. C. Bae, G.B. Rayner, G. Lucovsky, *Applied Surface Science* **216**, 119-123 (2003)

36. R. Therriem. G. Lucovsky, R. Davis, *Applied Surface Science* **166**, 513-519 (2000)

37. C. Bae, G. Lucovsky, *Surface Science* **532-535**, 759-763 (2003)

38. C. Bae, G. Lucovsky, *Applied Surface Science* **212-213**, 644-648 (2003)

39. Y. Nakano, T. Kachi, T. Jimbo, *Applied Physics Letter*, **83**(21), 4336-4338 (2003)

40. S.J. Chang, Y.K. Su, Y.Z. Chiou, J.R. Ciuo, B.R. Huang, C.S. Chang, J.F. Chen, *Journal of the Electrochemical Society*, **150**(2), C77-C80 (2003)

41. E.D. Readinger, S.D. Wlter, D.L. Waltermyer, J.M. Delucca, S.E. Mohney, B.I. Prenitzer, L.A. Gainnuzzi, R.J. Molnar, *Journal of Electronic Materials* **28**, 257 (1999)

42. M. Hong, J.P. Mannaerts, J.E. Bower, J. Kwo, M. Passlack, W-Y. Hwang, L.W. Tu, *Journal of Crystal Growth* **175/176**, 422 (1997)

43. F. Ren, M. Hong, W.S Hobson, J.M. Kuo, J.R. Lothian, J.P. Mannaerts, J. Kwo, S.N.G. Chu, Y.K. Chen, A.Y. Cho, *Solid State Electronics* **41**, 1751 (1997)

44. Y.C. Wang, M. Hong, J.M. Kuo, J.P Mannaerts, J. Kwo, H.S. Tsai, J.J. Krajewski, J.S. Weiner, Y.K. Chen, A.Y. Cho, *Materials Research Society Symposium Proceedings* **573**, 219 (1999)

45. J. Kwo, M. Hong, A.R Kortan, D.W. Murphy, J.P Mannaerts, A.M. Sergent, Y.C. Wang, K.C Hsieh, *Materials Research Society Symposium Proceedings* **573**, 57 (1999)

46. T.S. Lay, M. Hong, J. Kwo, J.P Mannaerts, W.H. Hung, D.J. Huang, *Materials Research Society Symposium Proceedings* **573**, 131 (1999)

47. A.R. Mortan, M. Hong, J. Kwo, J.P Mannaerts, N. Kopylov, *Materials Research Society Symposium Proceedings* **573**, 21 (1999)

48. F. Ren, M. Hong, S.N.G. Chu,, M.A. Marcus, A. Baca, S.J. Pearton, C.R. Abernathy, *Applied Physics Letters*, **73**(26), 3893-3895 (1998)

49. J. Kim, R. Mehandru, B. Lou, F. Ren, B.P. Gila, A.H. Onstine, C.R. Abernathy, S.J. Pearton, Y. Irokawa, *Applied Physics Letters* **81**(2), 373-375

50. B. Lou, J.W Johnson, B.P. Gila, A.H. Onstine, C.R. Abernathy, F. Ren, S.J. Pearton, A.G. Baca, A.M. Dabiran, A.M. Wowchack, P.P. Chow, *Solid State Electronics* **46**, 467-476 (2002)

51. R. Mehandru, B.P. Gila, J. Kim, J.W Johnson, K.P. Lee, B. Lou, A.H. Onstine, C.R. Abernathy, S.J. Pearton, F. Ren, *Electrochemical and Solid State Letters* **5**(7) G51-G53 (2002)

52. B. Lou, J.W Johnson, J. Kim, R. Mehandru, F. Ren, B.P. Gila, A.H. Onstine, C.R. Abernathy, S.J. Pearton, A.G. Baca, R.D. Briggs, R.J. Shul, C. Monier, J. Han, *Applied Physics Letters* **80**(9) 1661-1663 (2002)

53. J. Kim, B.P. Gila, R. Mehandru, J.W Johnson, J.H. Shin, K.P. Lee, B. Lou, A.H. Onstine, C.R. Abernathy, S.J. Pearton, F. Ren, *Journal of the Electrochemical Society* **149** (8) G482-G484 (2002)

54. W.M. Yim, E.J. Stofko, P.J. Zanzucchi, J.I. Pankove, M. Ettenburg, S.L. Gilbert, *Journal of Applied Physics*, **44**, 292 (1973)

55. V.W.L. Chin, T.L. Tansley, T. Osotchan, *Journal of Applied Physics*, **75**, 7365 (1994)

56. M.S. Shur, M.A. Khan, *Mat. Res. Bull.*, **22**(2), 44 (1997)

57. A.I. Manakov, O.A. Esin, B.M. Lepinskikh, *Russian Journal of Physic and Chemistry*, **36**, 1481, (1965)

58. *Refractory Production, Handbook* [in Russian], Izd. Metallurgiya , 1965

59. G.W. Kaye, T.H. Laby, *Tables of Physical and Chemical Constants and some Mathematical Functions, 11th ed*, Longmans, New York, 1956

60. S.J. Pearton, *International. Journal of. Modern. Physics. B*, **7**, 4687 (1993)

61. M. Passlack, M. Hong, J.P. Mannaerts, *Applied Physics Letters*, **68**, 1099 (1996)

62. O. Kubaschewski and B. Hopkins, *Oxidation of Metals and Alloys* [Russian translated], Izd. Metallurgiya, 1965

63. S.S. Derbeneva, S.S. Batsano, *Dokl. Chem.*, **175**, 710 (1967)

64. S.S. Batsono, E.V. Dulepov, *Soviet Physics – Solid State*, **7**(4), 995 (1965)

65. K.A. Gschneider, *Rare Earth Alloys* [Russian translation], Izd. Mir., 1965

66. Q. Xiao and J.J. Derby, *Journal of Crysal Growth*, **139**, 147 (1994)

67. S.M. Sze, *Physics of Semiconductor Devices, 2nd edition*, Wiley, New York, 1981

68. D.R. Lide, *Handbook of Chemistry and Physics, 71st edition*, CRC Press, Boca Raton, 1990

69. R.L. Melik-Davtyan, N.F. Shvartsenau, A.I. Shelykh, *Inorganic Materials*, **2**(1), 21 (1966)

70. J.L. Pentecost, *Ceramic Age*, **71**, 26 (1958)

71. A.A. Vorob'ev, *Physical properties of Crystalline Ionic Dielectrics* [in Russian], Izd. Tomsk. Univ. 1961

72. G.V. Samsonov, *The Oxide Handbook*, Plenum, New York, 1973, and references therein

73. Radical Beam Source Model MDP21S Operating and Service Manual, Oxford Applied research, Witney (1989)

74. D.K. Schroder, *Semiconductor Material and Device Chartacterization 2nd ed.*, Wiley, New York, 1998

75. B.D. Cullity, *Elements of X-ray Diffraction, 2nd ed*, Addison-Wesley, London, 1978

76. Y. Kuroda, E. Yasugi, H. Aoi, K. Miura, T. Morimoto, *Journal of Chemical Society, Farady Tansactions*, **84**(7), 2421-2430 (1988)

77. Refson, Wogelius, Fraser, Payne, Lee, Milman; *Physical Review B* **52**(15) (1995)

78. E.M. Levin, C.R. Robins, H.F. McMurdie, Phase *Diagrams for Ceramists*, The American Ceramic Society, Columbus, 1964

79. E.S. Hellman, E.H. Hartford, Jr., *Applied Physical Letters* **64** (11) 1341-1343 (1994)A. H. Onstine, B. P. Gila, J. Kim, D. Stodilka, K. Allums, C. R. Abernathy, F. Ren, S. J. Pearton submitted for publication in *Sol. Stat. Elect.* 2003.

81. B.P. Gila, J.W. Johnson, R. Mehandru, B. Luo, A.H. Onstine, K.K. Allums, V. Krishnamoorthy, S. Bates, C. R. Abernathy, F. Ren, S.J. Pearton, *Phys. Stat. Sol. (a)* **188** (1), 239-242 (2001).

BIOGRAPHICAL SKETCH

I was born in Minneapolis, Minnesota in 1975. I received my Bachelors in Chemical Engineering from the University of Florida in May 1999. I then continued on in graduate school in Materials Science and Engineering and received my Masters of Science in Materials Science and Engineering from the University of Florida in December 2002 and Doctor of Philosophy in Materials Science and Engineering from the University of Florida in December 2004. While in school at UF I started the Florida Swing Dancing Club. I also lived on a horse farm, in an apartment in the barn, while in graduate school, which was wonderful.